A modular, comprehensive microscopy platform for modern live cell imaging

Dissertation
der Mathematisch-Naturwissenschaftlichen Fakultät
der Eberhard Karls Universität Tübingen
zur Erlangung des Grades eines
Doktors der Naturwissenschaften
(Dr. rer. nat.)

vorgelegt von
Dipl.-Chem. Sven zur Oven-Krockhaus
aus Bochum

Tübingen
2021

Gedruckt mit Genehmigung der Mathematisch-Naturwissenschaftlichen Fakultät der Eberhard Karls Universität Tübingen.

Tag der mündlichen Qualifikation:	21.10.2021
Dekan:	Prof. Dr. Thilo Stehle
1. Berichterstatter/-in:	Prof. Dr. Alfred J. Meixner
2. Berichterstatter/-in:	Prof. Dr. Erik Schäffer

Acknowledgement

Without the support of numerous people, this thesis could not have been realized in this form. I would like to take this opportunity to thank them for the help they have given me.

First of all, I would like to express my special thanks to my doctoral supervisor Professor Dr. Alfred J. Meixner for giving me the opportunity to carry out my work in his laboratory, for his support and encouragement. His broad-based scientific curiosity initiated many interesting and satisfying interdisciplinary projects for which I am very grateful.

I sincerely thank Prof. Dr. Erik Schäffer, who kindly agreed to be a referee of this thesis.

Prof. Dr. Klaus Harter deserves great credit for his inspiring enthusiasm for this work. His interest in spectromicroscopy techniques for biological problems was the key to finding my place in this field of research, accompanied by his vast knowledge and constant support.

PD Dr. Frank Schleifenbaum originally sparked my interest for this kind of work. His scientific and personal guidance, as well as his continuous input to my output, have contributed greatly to the success of this thesis.

The Nano-Optics Group Tübingen is appreciated for their good teamwork, providing a pleasant work environment and helpful discussions. Special thanks go out to my colleagues Dr. Sébastien Peter and Tim Rammler who shared my fascination for interdisciplinary projects. Helping each other overcome the occasional stumbling block in our research has also brought us closer together personally.

I also thank the Department of Plant Physiology in Tübingen for engaging in our many fruitful collaborations and for welcoming a non-biologist into their midst, in research and in retreats. Special thanks go out to Dr. Friederike Wanke for proofreading the biological parts of this thesis.

The Deutsche Forschungsgemeinschaft (DFG) is acknowledged for their financial support.

My heartfelt thanks go to my partner Dr. Anke Horneber, not only for proofreading and her scientific support, but especially for her emotional encouragement and for always being there for me.

Contents

i. List of Figures

ii. List of Tables

1 Introduction and Outline

For classical microscopy, the detected light intensity is the main source of information. Advanced techniques such as polarization microscopy (1830) or interference contrast microscopy (1932) showed early on that utilizing the physical properties of light is indispensable for further developments. Spectroscopy, the analysis of light-matter interactions, is thus an ideal complement to microscopy, providing additional layers of information that enable a much more comprehensive characterization of samples. Especially in life sciences, the combination of imaging with spatially resolved spectroscopy ("spectromicroscopy") is key for modern microscopy and serves as an important tool to gain ever deeper insights into the complexity of biological processes. Numerous techniques, based on photophysical or physiochemical processes, are employed to resolve increasingly fine spatial or temporal properties of the intricate structure and regulation processes of living cells. In this respect, the relatively recently established superresolution microscopy can image nanoscopic structures that have never been directly observed in vivo. Generally, the number of optical analytical methods to elucidate processes in a biological system is nowadays very diverse and numerous. Consequently, most studies in the field of life sciences are based not only on classical biochemical and molecular biological methodology, but increasingly on imaging techniques in vivo. The inherent advantage is, of course, the direct observation of largely undisturbed biological processes in intact cells. It is precisely through the combination of different, complementary methods (in particular also by different spectromicroscopy techniques) that scientific knowledge can be gained with a significantly higher reliability than it would be possible by the individual techniques. Accordingly, the requirements for a modern research microscope have constantly increased. Through the study of interdisciplinary research subjects within the framework of this thesis, it was first determined which microscopic techniques are most valuable for a modern research microscope in the life sciences. The corresponding spectromicroscopy methods were applied and adapted in line with the respective scientific questions. This allowed for an overview of requirements that are especially important to provide a robust analysis infrastructure, particularly in the case of interdisciplinary projects. Commercial microscopes usually specialize in some of these requirements and are therefore very

precise and fast for their unique purpose, such as high-throughput routine measurements with high throughput rates. In the course of the joint research projects and collaborations, it became clear, however, that the highest obstacle to generate significant data is the establishment of a tailor-made spectromicroscopy methodology to test a theory experimentally. For this purpose, access to different measuring methods with a flexible basic platform is essential to meet the requirements of a given experiment regarding both microscopy and spectroscopy. This was the motivation to build up a corresponding microscope and to conceive it precisely for interdisciplinary research approaches. The implementation into one platform also has the advantage that different methods can be directly compared with one another. Furthermore, the desired experiment can already be explored for possible combinations of spectromicroscopy techniques.
The applicability of various spectromicroscopy methods has been demonstrated in several publications. On one hand, the peer-review process provides an independent validation of the chosen method and expertise, on the other hand it underlines the importance and usefulness of those analysis tools in current research. Therefore, a short description of the respective experiments will focus on the methodical parts provided in chapter 3, referencing the complete publications to illustrate the analysis techniques as tools in the wider context of the research field. The collected experiences from the research projects served as a starting point to develop the flexible, interdisciplinary research microscope described in chapter 4. This design approach already suggests that it is subject to constant development. Emerging new spectroscopic methods, instrumentation or mathematical analysis algorithms continually change the scope of what is possible or attainable in live cell imaging. For that reason, the flexible custom-built microscope and its high adaptability to newly arising research topics provides an excellent basis and motivation for the development of new techniques and the evaluation of viable combinations.

2 Theory of Utilized Spectroscopy Techniques

2.1 General Concepts of Fluorescence Microscopy

Exploring our reality beyond the capability of our physical senses has always been a driving force in scientific research. The development of microscopes led to a far better understanding of how biological life is organized on a size scale hidden from the naked eye. For a literally clearer image, many technical advances in this field concentrated on the improvement of the signal-to-noise ratio. Fluorescence microscopy offered a way to exclusively visualize objects of interest against an otherwise dark background and was achieved by addressing these objects by spectroscopic means, usually requiring labeling of these objects with fluorophores. Since fluorescence techniques, their resolution and image contrast are prominently featured in this work, a short introduction into the basics of light-matter interactions, optical spectroscopy and microscopy will be given in the following.

2.1.1 Absorption and Fluorescence

When molecules interact with electromagnetic radiation, the most important processes can be visualized with Jabłoński diagrams [1] (Figure 2.1a), where the energy structure of molecules is characterized by quantized levels. Most molecules exist in the electronic singlet ground state S_0 at room temperature. When a photon is absorbed, the molecule undergoes a transition to an excited state, for example to a vibrational level of the first excited singlet state S_1, if this energy difference corresponds to the photon's energy

$$E = h\nu \tag{2.1}$$

with Planck's constant h and photon frequency ν. The excited vibrational modes relax rapidly to lower states due to their intramolecular arrangement or intermolecular interactions with the nano-environment, thus called vibrational relaxation (VR). Internal conversion (IC) describes an isoenergetic process that involves overlapping vibrational states of different excited electronic states, usually followed by VR. Fluorescence can be regarded as the reverse of absorption and returns the molecule to the electronic singlet ground state S_0 under simultaneous emission of a photon. As fluorescence occurs within a relatively large time frame (typically several nanoseconds), the non-radiative and noncoherent VR and IC processes are generally already complete. Therefore, spontaneous fluorescence emission almost exclusively occurs from the lowest vibrational level of S_1, irrespective of the initial excited energy state. This means that emission spectra are commonly independent of their excitation wavelength, which is also known as Kasha's rule [2]. The energy loss caused by VR after excitation is the reason for the energy difference of their respective spectra for the same electronic transition, denoted as the Stokes shift [3]. Fluorescence spectroscopy takes advantage of this principle by separating excitation from emission light with the use of color filters.

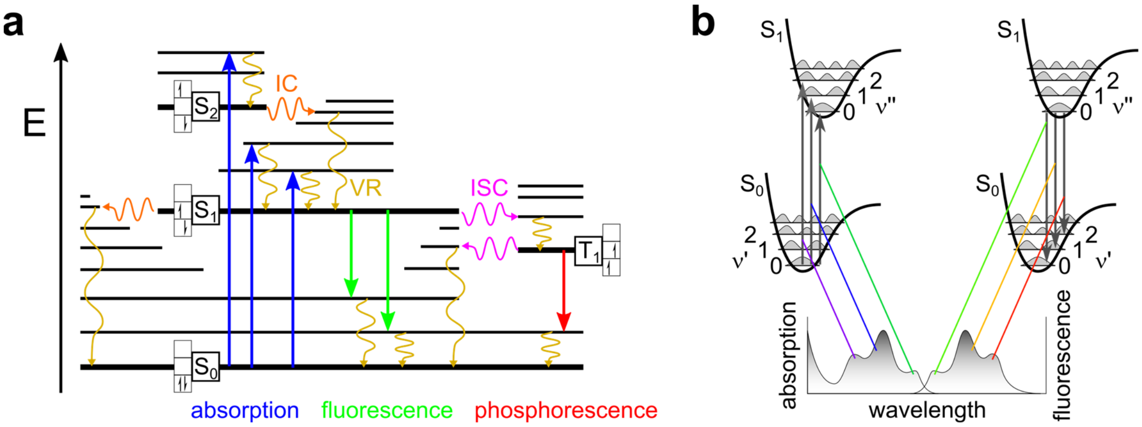

Figure 2.1 | Electronic and vibronic transitions in spectroscopy. (a) Jablonski diagram with electronic transitions of absorption (blue), fluorescence (green) and phosphorescence (red). A combination of the isoenergetic processes of internal conversion (IC, orange) or intersystem crossing (ISC, pink) with vibrational relaxation (VR, yellow) also allows for the non-radiative decay of excited states. **(b)** Franck-Condon principle. Vertical transitions (static nuclear coordinates) can lead into higher vibrational states of the corresponding electronic states for both absorption and emission. As both processes rely on the same vibronic structure, their spectra show a mirror symmetry.

Optical transitions as described above are caused by oscillations of the electric field interacting with the charge distribution of the molecule. In quantum mechanical terms, the probability of an optical transition between the initial and final state of a molecule is dependent on the transition dipole moment

$$\boldsymbol{\mu}_{i\to f} = \int \psi_f^* \hat{\boldsymbol{\mu}}_e \psi_i \, d\tau \tag{2.2}$$

integrated over the entire space τ with electric dipole moment operator $\hat{\boldsymbol{\mu}}_e$ and wave functions ψ_f and ψ_i for the final and initial state, respectively. These total wave functions include all contributions of translations, rotations, vibrations (vib), electronic states (el), as well as nuclear and electron spins (S). Following the Born-Oppenheimer approximation, these contributions can be considered independent from each other. For optical spectroscopy applications only vibrations, electronic states and electronic spins will be factored in. As the influence of $\hat{\boldsymbol{\mu}}_{\boldsymbol{e}}$ on spin functions is negligible, this results in

$$\boldsymbol{\mu}_{\boldsymbol{i}\rightarrow\boldsymbol{f}} = \int \psi_S^* \psi_S \, d\tau_S \cdot \int \psi_{vib}^* \psi_{el}^* \hat{\boldsymbol{\mu}}_{\boldsymbol{e}} \psi_{vib} \psi_{el} \, d\tau_{el,vib} \tag{2.3}$$

with the first integral describing the electronic spin functions. The conservation of angular momentum forbids electronic transitions that change the spin multiplicity and constitutes a selection rule. However, this does not mean that they do not happen at all, they just occur at much smaller rates. As depicted in Figure 2.1a, such an isoenergetic transition from the singlet state S_1 to the triplet state T_1 by spin reversal of the electron is called intersystem crossing (ISC). Following thermal equilibration, the direct emission of a photon from T_1 with simultaneous transition to S_0 by another spin conversion is called phosphorescence. Depending on the triplet state energy, a second ISC back to the singlet state could also result in non-radiative thermal equilibration to the ground state or delayed fluorescence. As transitions to and from a triplet state are improbable, they are long-lasting with typical lifetimes on the order of micro- to milliseconds. Considering only allowed transitions, the first integral in equation (2.3) is constant and will therefore be disregarded.

As the movement of electrons is much faster than vibrations of the nuclei, their wave functions can be separated and $\hat{\boldsymbol{\mu}}_{\boldsymbol{el}}$ now only acts on the electronic contributions:

$$\boldsymbol{\mu}_{\boldsymbol{i}\rightarrow\boldsymbol{f}} = \int \psi_{vib}^* \psi_{vib} \, d\tau_{vib} \cdot \int \psi_{el}^* \hat{\boldsymbol{\mu}}_{\boldsymbol{e}} \psi_{el} \, d\tau_{el}. \tag{2.4}$$

The second integral of equation (2.4) allows to derive additional selection rules. For example, as $\hat{\boldsymbol{\mu}}_{\boldsymbol{e}}$ is a directional operator, the electrical field vector $\boldsymbol{E}$ of a photon must not be perpendicular to it, otherwise their scalar product is zero, preventing absorption. This orientation dependency of the molecule on the polarization of light can be utilized in several spectroscopic techniques, such as fluorescence anisotropy.

The square of the first integral's absolute value in equation (2.4) is also known as the Franck-Condon factor [4-6] and describes the probability of electronic transitions into corresponding vibrational states. Electronic state changes will alter the charge distribution in a molecule and ultimately lead to a realignment of the nuclear distance. However, at the moment of electronic transition, the nuclear coordinates can be considered as static due to the much slower movement of the nuclei. Figure 2.1b depicts this by vertical arrows for absorption and emission. Since the nuclear potential wells are shifted with respect to each other, a vertical transition from the lowest vibrational state ends in a state farther away from the potential minimum. This changes the probability for the transition into higher vibrational states, and the intensity of this transition is proportional to the overlap integral of the involved vibrational wave functions. As the Franck-Condon principle applies to both emission and absorption, this often results in a mirror symmetry of the respective spectra (see Figure 2.1b, bottom). Instead of sharp lines, mostly partly overlapping absorption and emission bands are observed. This effect in part arises from Heisenberg's uncertainty principle [7], stating that the excited state lifetime and its energy cannot be precisely determined at the same time, which is also called natural broadening. Many inhomogeneous broadening effects are dominant at room temperature and relate to molecules interacting with their surroundings, resulting in a larger distribution of possible energy states.

2.1.2 Raman Spectroscopy

While absorbance and fluorescence emission spectroscopy probes the electronic structure of molecules and materials, Raman scattering [8, 9] allows access to their vibrational modes, thus providing additional structural information. In the classical wave interpretation, the oscillating electric field of the incident light induces a dipole moment in the molecule, which strength is dependent on its polarizability. Therefore, molecules with an extended π-system will have much higher scattering cross sections than small molecules with single bonds. In the more descriptive quantum particle interpretation, scattering is described as the excitation into so-called virtual energy states. For the subsequent reemission of the scattered photon, three cases can be distinguished: a) incident and scattered radiation show the same frequency (the return from the virtual energy state results in the initial state), this is called elastic or Rayleigh scattering; b) with much lower probability, the return from the virtual energy state results in a relatively higher (Stokes Raman scattering) or c) lower (Anti-Stokes Raman scattering) vibrational mode of the molecule than its initial one. Consequently, the two latter inelastic Raman effects shift the frequency of the scattered photon by the energy difference of the initial and final state. Due to the excitation into virtual states, the Raman shift is generally wavelength-independent and therefore often expressed as the difference in wavenumbers (cm^{-1}) relative to the incident wavelength. The vibrational modes then appear as sharp spectral lines with either positive or negative relative wavenumbers, so-called Stokes or (usually much weaker) anti-Stokes lines, respectively. As the typical cross section for Rayleigh scattering is several orders of magnitude higher than for Raman scattering, the incident wavelength must be suppressed by high-quality optical filters. Although scattering would be higher at lower wavelengths, many organic molecules will show dominant fluorescence bands in this region that can completely obscure Raman lines. Therefore, visible or near infrared excitation is much more common, as long as the spectral limit of the detector is not exceeded. Moreover, monochromatic light sources like lasers with narrow spectral linewidths and high-quality spectrometer gratings are crucial to achieve a high resolution of vibrational modes. Under these conditions, Raman spectroscopy is a highly selective technique that can detect the fingerprint of molecules or even structural changes in their molecular bonds. This makes it an important tool in many fields, including chemical-pharmaceutical analytics, physics, material sciences and increasingly also in live cell experiments with plant or mammalian tissue [10].

2.1.3 Optical Resolution

Ernst Abbe described the spatial resolution limit of optical systems (the minimum distance to distinguish two point sources) by researching the physical conditions for the imaging of fine line gratings [11]. His findings can be expressed by the equation

$$r_0 = \frac{0.5 \cdot \lambda}{n \sin \alpha} \tag{2.5}$$

with minimal resolvable lateral distance r_o and the wavelength of light λ. The product $n \sin \alpha = \mathrm{NA}$ (numerical aperture) is a characteristic feature of focusing optical elements like microscope objectives, including the refractive index n of the immersion medium and the half-angle α of the light cone that can enter the optical element. Equation (2.5) implies that typical light microscopes cannot resolve structures smaller than approximately 200 nm. There are several approaches to arrive at this conclusion that can be most illustratively described by diffraction effects due to the wave properties of light.

According to Huygens's principle [12], all points on a wave front can be considered as point sources of new, spherical secondary wavelets. Their envelope, or their sum, then describes the wave front position at a later time, thus illustrating standing wave propagation. Fresnel joined this principle with his own findings on wave interference [13] and was thus able to provide a physical description of the phenomenon of diffraction.

In case of far-field illumination (incident planar wave front and large distance between aperture and screen), the intensity distribution can be approximated by Fraunhofer diffraction. For circular apertures, featured in most optical devices, the relative angular intensity distribution it is given by

$$\frac{I(\theta)}{I_0} = \left[\frac{2J_1(x)}{x}\right]^2 \tag{2.6}$$

with intensity I in dependence of the angle θ to the optical axis, maximum intensity I_0 of the diffraction pattern, using a so-called Bessel function J_1 of the first kind and first order. The term $x = ka\sin\theta$ contains the diameter a of the aperture, while wave vector $k = 2\pi n/\lambda$ comprises the wavelength λ of the incident light and the refractive index n. The graphical representation of equation (2.6) is also known as Airy pattern, with its innermost bright region called Airy disk (Figure 2.2a, inset). The far-field approximation also holds true when the circular aperture is replaced by a lens with a finite aperture size. Point sources are also valid, as their radiation's wavelength is typically very small compared to the distance to the lens, and thus, their wave fronts can be considered as planar when they strike the lens. Consequently, each point source in the sample plane will be represented by an Airy pattern in the imaging plane (Figure 2.2a). When the sources get very close together, the optical resolution will be limited by the ability to separate their overlapping diffraction patterns. The Rayleigh criterion states that two objects can just be resolved when the central maximum of one Airy pattern coincides with the first minimum of the other (Figure 2.2b, top). For microscope optics, this angular resolution limit translates to the minimal resolvable distance

$$r_0 = \frac{0.61 \cdot \lambda}{\mathrm{NA}} \tag{2.7}$$

with the wavelength of light λ and numerical aperture NA of the microscope's objective. It should be pointed out that the underlying definition is slightly arbitrary, as it is based on the perceived separation of the Airy patterns, which would also be influenced by photon statistics, contrast and fitting algorithms. The Sparrow limit (Figure 2.2b, bottom) also provides a measure of a minimal resolvable separation. Nevertheless, the Abbe diffraction limit and the Rayleigh criterion provide very similar results. Similar considerations based on focus depth lead to the calculation of the axial resolution z_0 with

$$z_0 = \frac{2n \cdot \lambda}{\mathrm{NA}^2} \tag{2.8}$$

which is an approximation for high-NA lenses [14] and leads to an achievable resolution of approximately 1.5 µm.

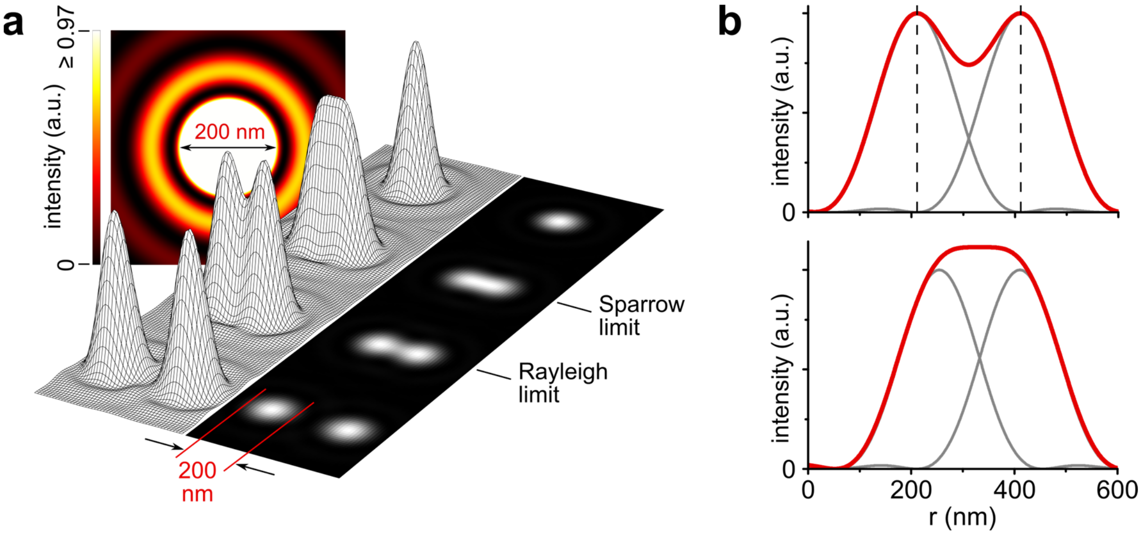

Figure 2.2 | Optical resolution limit. (a) Simulated two- and three-dimensional representations of the Airy pattern generated by a lens with a numerical aperture of 1.49, assuming monochromatic illumination with 488 nm. When two point emitters in the sample plane are closer than the diffraction limit, they can no longer be resolved in the imaging plane. This is shown in the topmost case; the other cases show sufficient separation (lowest case) and separations corresponding to the Rayleigh and Sparrow resolution limit. Upper left inset: contrast enhanced simulation of a 2D Airy pattern to show the pattern's outer rings. The innermost part up to the first intensity minimum is commonly called the Airy disk. **(b)** Intensity profiles of two emitters at the Rayleigh resolution limit (top, the dashed lines connect the respective minima and maxima) and Sparrow resolution limit (bottom, indicated by the flat peak of the added intensities, red line).

The resolving power of an optical system can also be defined as the full width at half maximum (FWHM) of the system's point spread function (PSF) which is identical to the Airy pattern if optical aberrations are negligible. In practice, imaging the PSF of a point source-like emitter, for example, quantum dots or fluorescently labeled polystyrene microspheres, is a very straightforward way to determine the optical resolution of a confocal microscope (see below). As can be inferred from Figure 2.2b, the PSF can be well approximated by a Gaussian function, which can be used to slightly increase the apparent resolution by deconvolution, a computationally intensive method to reduce diffraction blurring [15, 16]. Knowledge of the PSF is also important in localization-based superresolution techniques that allow for even better contrast as their resolution is no longer governed by the diffraction limit. They will be discussed in chapter 2.4 in greater detail.

2.1.4 Confocal Microscopy

Originally developed by Marvin Minsky [17], this microscopy type focuses an excitation light source on a single point in the sample plane while collecting the emerging fluorescence photons exclusively from this very point with a sensitive photon detector (Figure 2.3). To acquire an image, the specimen is scanned point-by-point until all points are translated into an intensity image of sufficiently small pixels. This, in itself, would not yet improve the image quality. However, by introducing a small pinhole in front of the detector in a conjugate plane to the focus plane, out-of-focus light is effectively blocked, leading to higher contrast, especially in the axial direction. Often, also the illumination source is described as confocal to the detection pinhole. As modern fluorescence microscopes mainly use lasers to excite fluorophores in the sample, it is better to generalize that the illumination light must be collimated when it enters the objective to ensure that both excitation PSF_{exc} and detection PSF_{det} are coinciding.

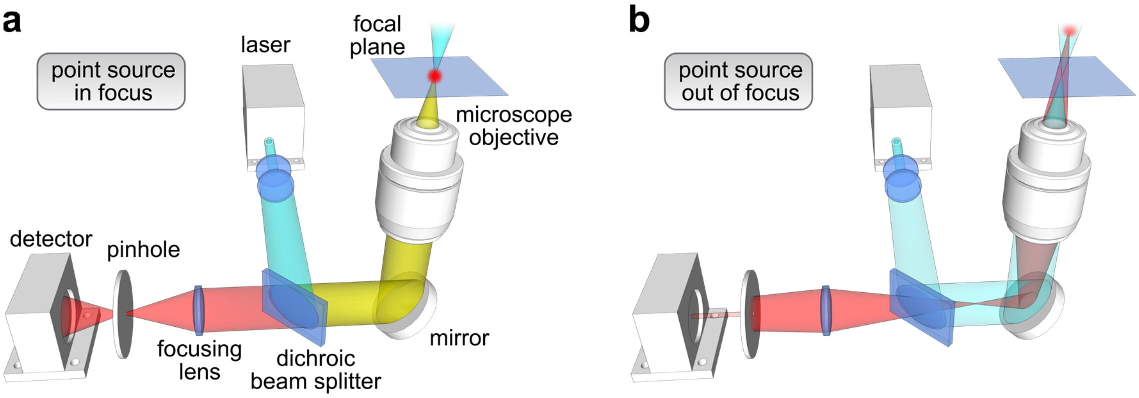

Figure 2.3 | Working principle of a modern confocal microscope. (a) The light of the emitter point source is detected if the emitter is in a conjugate plane to the pinhole in front of the detector. **(b)** Light from emitters outside the focus of the microscope objective is blocked by the pinhole (shown here for the axial case), leading to higher contrast for objects that are in focus.

Following the Rayleigh criterion, the optical resolution would then be given by the product $\mathrm{PSF}_{exc} \cdot \mathrm{PSF}_{det}$, or (ignoring different excitation and emission wavelengths) simply $(\mathrm{PSF}_{exc})^2$. As this would only narrow the peaks in the Airy pattern without changing the minima and maxima, the Rayleigh criterion cannot be applied here (see Figure 2.2d). Therefore, the resolution is better estimated by the FWHM of the squared PSF [14]. Due to the similarity with a Gaussian function, it can easily be inferred that the lateral resolution is thereby enhanced by a factor of $\sqrt{2}$. However, this represents the marginal case of an infinitesimally small pinhole and no color shift between excitation and emission. In practice, the pinhole size is usually set to one Airy Unit (1 AU), including the central intensity of the Airy pattern up to the first minimum (which is also denoted as Airy disk).

This is regarded as a good compromise between reducing extraneous light and losing too much intensity. In this case, a practical estimation for the image resolution of a confocal microscope is given by [18]

$$r_{0,\mathrm{FWHM}} = \frac{0.51 \cdot \lambda_{exc}}{\mathrm{NA}} \tag{2.9}$$

for the lateral resolution, only regarding the excitation wavelength λ_{exc} and

$$z_{0,\mathrm{FWHM}} = \frac{0.88 \cdot \lambda_{exc}}{n - \sqrt{n^2 - \mathrm{NA}^2}} \tag{2.10}$$

for the respective axial resolution. While this improves the lateral resolution only slightly when compared with equation (2.7), the gain in axial resolution is around threefold. Accordingly, the true power of confocal microscopy lies in the ability to block light from out-of-focus planes and stray light, which drastically enhances the image contrast, thus allowing optical sectioning despite relatively slow acquisition speeds. A modern confocal scanning microscope features lasers of different wavelengths as coherent excitation sources to cover the most common fluorophores, using adjustable pinholes for extended control over image contrast and intensity.

2.1.5 Total Internal Reflection Microscopy

In conventional wide-field optical epi-fluorescence microscopes, a considerable contrast improvement can be achieved with total internal reflection microscopy [19] (TIRFM). In objective-based TIRFM, a collimated laser beam is focused off-axis on the back focal plane of an objective with a high numerical aperture (Figure 2.4a, left), typically above 1.45. The emerging laser beam then strikes the coverslip/sample interface with an angle of incidence θ_{inc}.

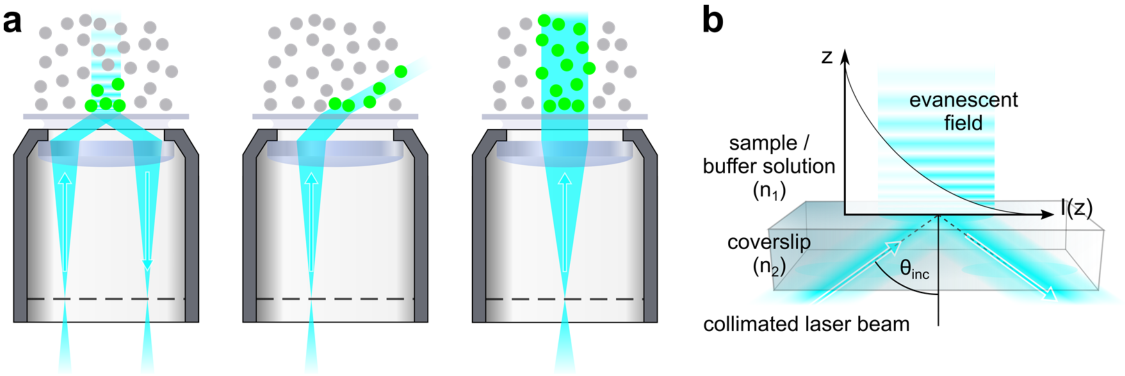

Figure 2.4 | Selected illumination techniques in fluorescence microscopy. (a) Different beam paths of a laser focused on the back focal plane of an objective, resulting in total internal reflection illumination (left), variable angle epi-fluorescence illumination (middle) and epi-fluorescence illumination (right). **(b)** When a collimated laser beam strikes a glass/water interface with an angle of incidence θ_{inc} larger than the critical angle, it is totally internally reflected. Part of the incident light intensity couples into the medium with lower optical density as a non-propagating evanescent field.

Beyond the critical angle θ_{crit}, total reflection of the laser beam occurs, coupling out part of its energy as a non-propagating evanescent wave that extends into the sample

(Figure 2.4b). The intensity I of this electromagnetic field decays exponentially according to

$$I(z) = I_0 e^{-z/d}$$

with incident light intensity I_0, distance from the interface z and penetration depth

$$d = \frac{\lambda_0}{4\pi}\left(n_1^2 \sin^2 \theta_{inc} - \frac{n_2^2}{n_1^2}\right)^{-\frac{1}{2}} \tag{2.11}$$

with wavelength λ_0, incident angle $\theta_{inc} > \theta_{crit}$ and refractive indices n_1 and n_2 for the materials at the interface with higher and lower optical density, respectively. In a typical configuration, the penetration depth ranges from 50 to 150 nm relative to the coverslip/sample interface. Thus, only fluorophores near the interface are excited, which strongly suppresses out-of-focus light (see Figure 2.4a, left). This results in much better image contrast for biological structures like mammalian cell membranes that adhere directly to the glass substrate. Other cell organelles or cell types may pose challenges: plant cells, in particular, can feature thick cell walls that preclude TIRFM from reaching the cell membranes. Here, a related technique called variable-angle epifluorescence microscopy (VAEM) can be applied [20]. A highly oblique, but subcritical angle of laser beam incidence at the coverslip/sample interface results in a slanted sideband of illumination, offering variable illumination depths over the field of view (Figure 2.4a, middle). While not delivering the excellent background suppression of TIRFM, this allows for a much larger penetration depth beyond 200 nm, while still improving the signal-to-noise ratio in comparison with widefield epi-fluorescence illumination (Figure 2.4a, right). Moreover, the transition between TIRFM and VAEM illumination is precisely and easily controlled by adjusting the off-axis translation with the lens that focuses the laser beam on the back focal plane of the objective.

2.2 Fluorescence Lifetime Imaging Microscopy

An intensity image can provide spatial information about the distribution of the sampled fluorophores. However, fluorophores also have other interesting properties that can be used to discriminate between them or acquire deeper insights of their nano-environment. For example, by passing the fluorescence light to a spectrograph, fluorescence spectra can be acquired. In doing this point-by-point (in other words, spectral mapping), a new, independent parameter dimension is added to the intensity information. An equally interesting attribute of a fluorophore is its fluorescence lifetime (FLT). As illustrated in the Jabłoński diagram (Figure 2.1a), a molecule in an excited state can follow different pathways determined by its decay rate constants. The average duration a fluorophore spends in the excited state is the reciprocal of the summed decay rates of the excited state population:

$$\tau = \frac{1}{k_r + k_{nr}} \tag{2.12}$$

where τ denotes the FLT and k_r and k_{nr} the radiative and non-radiative decay constants, respectively. It is influenced by many interesting physicochemical properties, such as temperature, viscosity, polarity, refractive index, pH and external fluorescence quenchers. Accordingly, τ is very sensitive to the nano-environment, which makes it an ideal parameter to analyze biological processes in live cell imaging. The collection of FLT information per pixel is called Fluorescence Lifetime Imaging Microscopy (FLIM) and adds τ as a very revelatory time-resolved spectroscopic parameter to the intensity data.

Data acquisition and analysis of τ is performed either in the frequency domain (FD) or time domain (TD), using technical solutions that have been described in great detail in literature [21, 22]. The following remarks are intended to summarize the basic theoretical and practical aspects necessary to understand the experiments in this work.

For FD measurements, an amplitude-modulated light source excites the sample with different modulation frequencies. Consequently, the detected fluorescence signal shows a modulation in amplitude and phase relative to the excitation, depending on τ. All FLT measurements in this work were based on TD measurements, therefore FD methods will not be discussed further. However, data from both methods can be interconverted through Fourier transform [23].

In TD measurements, the sample is excited by a short light pulse, typically from a pulsed laser source. The time-dependent intensity decay is recorded after the excitation, and τ is derived from the slope of a plot of $\log I(t)$ vs. t [21], which in case of a monoexponential decay follows

$$I(t) = I_0 \exp(-t/\tau) \tag{2.13}$$

with time-dependent intensity $I(t)$, and I_0 the intensity at time 0.

Conventional detection electronics for FLIM are not sufficiently sensitive or fast enough to collect a full intensity decay with high time-resolution. Therefore, a statistical approach, called time-correlated single photon counting (TSCPC), is applied (see Figure 2.5).

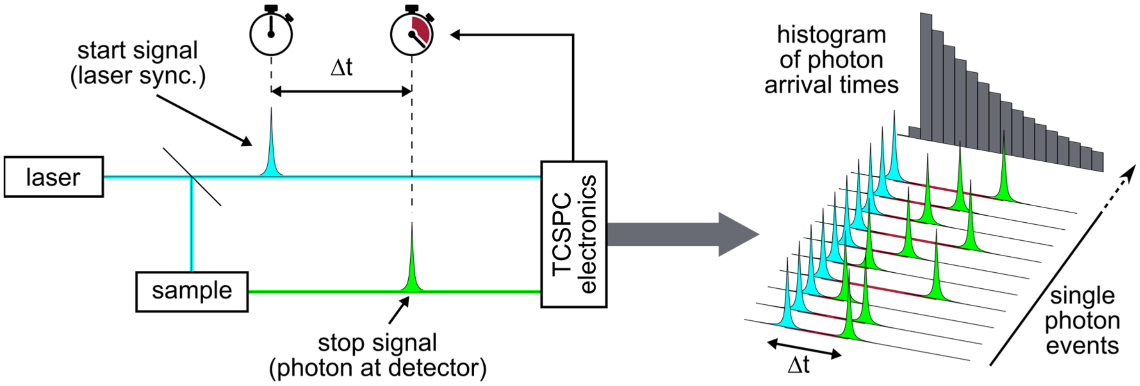

Figure 2.5 | Measurement principle of time-correlated single photon counting (TCSPC). An excitation laser pulse (blue) hits the sample and at the same time is registered as a start signal for the TCSPC electronics, while the first detected fluorescence photon from the sample (green) serves as the stop signal. The detection of many single photon events allows for a statistical estimation of the average fluorescence lifetime (FLT).

The data is collected for millions of excitation pulses, each starting a linearly increasing voltage ramp in the electronics, which stops with the signal of an incoming photon at the detector. Subsequent analog-to-digital conversion into time intervals allows for a time resolution in the range of picoseconds. To ensure the correct assignment of photon signals to the corresponding excitation pulse, laser intensities are kept low so that roughly only one in 100 laser pulses results in a detected fluorescence photon. However, high pulse repetition rates are essential: a) to reduce the acquisition time, which is particularly important for biological samples; and b) to overcome the intrinsic detector noise. Typically, pulse repetition rates of around 40 MHz enable to collect enough data to analyze the resulting photon arrival time histograms per sample point. These histograms (with their x-axis divided into time channels) represent the radiative decay of the excited state (Figure 2.6).

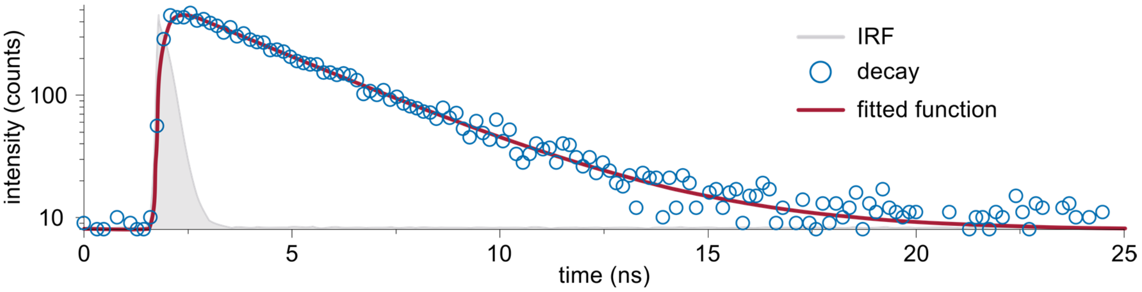

Figure 2.6 | Typical fluorescence decay curve. Time binned photon arrival times (blue circles) are fitted (red curve) with a convolution of the experimentally acquired instrument response function (IRF, gray curve) and an iteratively determined exponential function.

More details on the complexities and refinements in TCSPC instrumentation beyond the scope of this thesis can be found in literature [21, 22]. One consequential basic principle, however, is the influence of the instrument response function (IRF) on the acquired data. The IRF is a system-specific parameter that indicates a timing uncertainty, caused by optical elements, detector properties and timing electronics. It represents the apparent fluorescence decay that would result from a sample with instantaneous fluorescence emission. In contrast to an (ideal) infinitesimally sharp excitation pulse, the IRF shows a finite width (see Figure 2.6, gray curve) and, therefore, all acquired decay curves are a convolution of the real intensity decay of the fluorophore with the IRF. In consequence, this is limiting both the precision of the calculation of τ and the lower boundary of resolvable FLTs. However, the IRF can be acquired by recording fast processes well below the expected timing resolution, such as quenched dyes or dyes with very low intrinsic FLTs.

To determine the true parameters for an experimental decay, the IRF is convolved with a test function like equation (2.13) and compared with the experimental decay. Iteration of the test function in a computational optimization procedure produces a set of parameters that show the best match for the experimental decay (Figure 2.6, red curve). The common Nonlinear Least Squares (NLLS) approach minimizes the goodness of fit parameter χ^2 given by [21]:

$$\chi^2 = \sum_{k=1}^{n} \frac{1}{\sigma_k^2} [N(t_k) - N_c(t_k)]^2 \tag{2.14}$$

with the measured N and calculated N_c photon counts at each time channel t_k. As TCSPC counts single photon events, the standard deviation per time channel σ_k is given by Poisson statistics and therefore

$$\sigma_k = \sqrt{N(t_k)}\,. \tag{2.15}$$

To compare χ^2 of data sets with different numbers of data points, often the reduced χ^2 (χ_R^2, alternatively: reduced chi-square or red. chi²) is used [21], following

$$\chi_R^2 = \frac{\chi^2}{n-p} = \frac{\chi^2}{\nu} \tag{2.16}$$

with the number of data points n, the number of fitting parameters p and the number of degrees of freedom $\nu = n - p$. Although Poisson statistics are included in equation (2.15), the underlying noise in NLLS methods is assumed to be Gaussian, which is problematic if the number of photons per time channel is low. In single-molecule experiments, maximum likelihood estimation (MLE) methods give far better results, also in conjunction with IRF convolution and more complex fluorescence decay curves [24]. For higher photon counts, Poisson and Gaussian noise are equivalent: therefore, NLLS methods are usually sufficient to calculate τ from a fluorescence decay curve.

In conclusion, FLIM experiments deliver an important measurement parameter to, for example, discriminate between cell structures that are tagged with dyes of different fluorescent FLTs or to probe changes in the nano-environment around a fluorophore. However, the sensitivity of τ might also be an obstacle in experiments when the influence of several physicochemical parameters cannot be sufficiently differentiated, thus leading to distorted results with unclear origins. Fluorophores also often show significantly smaller FLTs in vivo, often depending on the cell compartment. Therefore, basic knowledge of cellular structures and processes is essential to interpret FLIM data correctly.

Furthermore, many cellular components are not only spectrally similar to common fluorescent probes, but also show comparable FLTs [25]. Chapter 2.2.2 will present a method to suppress this autofluorescence background based on the evaluation of the red. chi² values.

2.2.1 FLIM-FRET

Interaction assays are of key importance in biological research for several reasons. The knowledge about molecular interaction partners and their dynamics are essential to unravel the highly complex signal transduction pathways in cells. Most steps in gene expression involve the binding of effector molecules or conformational changes that alter inter- or intramolecular distances and orientations, for example to relay information or trigger metabolic changes. Methods that can show such processes in living organisms are therefore of prime interest. Förster Resonance Energy Transfer (FRET) is a highly distance-dependent physical phenomenon that shows a large dynamic range on biological interaction length scales. FRET occurs as a non-radiative dipole-dipole interaction between a donor and an acceptor molecule (see Figure 2.7a), first described by Theodor Förster [26]:

$$k_{ET} = \frac{\phi_D \cdot \kappa^2}{\tau_D \cdot r^6} \cdot \frac{9 \cdot \ln 10}{128 \cdot \pi^5 \cdot N_A \cdot n^4} \cdot J(\lambda) \tag{2.17}$$

where the energy transfer rate k_{ET} is dependent on the quantum yield ϕ_D and FLT τ_D of the donor in absence of the acceptor, the orientation factor κ^2, the distance r between donor and acceptor, the refractive index n of the surrounding medium and the spectral overlap integral $J(\lambda)$.

The spectral overlap integral (see Figure 2.7b) is given as

$$J(\lambda) = \int_0^\infty F_D(\lambda) \cdot \varepsilon_A(\lambda) \cdot \lambda^4 d\lambda \tag{2.18}$$

with absorbance coefficient $\varepsilon_A(\lambda)$ of the acceptor at wavelength λ and

$$F_D(\lambda) = f_D(\lambda) \, / \int_0^\infty f_D(\lambda) d\lambda \tag{2.19}$$

with $f_D(\lambda)$ as wavelength-dependent fluorescence intensity of the donor.

The orientation factor depends on how the dipole moments are aligned to each other (see Figure 2.7c) and varies from zero (perpendicular orientation) to four (collinear orientation). If both donor and acceptor can assume random orientations, for example when freely rotating in solution, κ^2 is averaged to a value of 2/3.

As most parameters in equation (2.17) are quantifiable constants, the equation can also be written as

$$E_{ET} = \frac{R_0^6}{r^6 + R_0^6} \tag{2.20}$$

with E_{ET} as the occurring energy transfer (ranging from 0 to 1) and R_0^6 as the Förster radius, indicating the interchromophoric distance that constitutes 50% energy transfer (see Figure 2.7a).

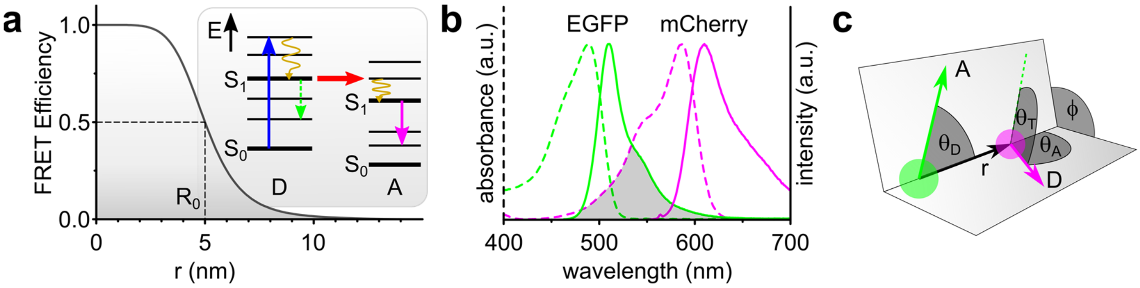

Figure 2.7 | Förster Resonance Energy Transfer (FRET) principle. (a) The Jablonski diagram shows the non-radiative FRET process (red) from a donor (D) to an acceptor (A). The interaction is highly distance-dependent: as shown in this simulated graph according to equation (2.20), the FRET efficiency quickly declines beyond a distance r of a few nanometers. The Förster radius R_0 is marked as the interchromophoric distance with 50% FRET efficiency. **(b)** For FRET to occur, a sufficient spectral overlap (gray) between the donor emission (solid green line) and the acceptor absorbance (dashed magenta line) is required. **(c)** The relative orientation of the donor and emitter transition dipole moments is expressed as the orientation factor κ^2, calculated from the angles in this diagram.

A direct interaction of two biological molecules, for example DNA and proteins, is usually inferred from their close vicinity. The high distance dependence of E_{ET} to the 6th power of r results in a dynamic range below 10 nm, thus discriminating between real binding events and random proximity by diffusion. FRET pairs in biological research are commonly based on fluorescent proteins (see chapter 2.5) that are genetically fused to the biological molecules of interest. In case of FRET, a part of the donor's excited state energy will migrate non-radiatively to the acceptor, thus resulting in a loss of donor fluorescence intensity. To measure E_{ET}, an intensity-based in vivo FRET assay relies on two data points: the donor fluorophore intensity with or without the accompanying acceptor fluorophore.

This is commonly accomplished by first recording the donor intensity with intact FRET pairs, then photobleaching the acceptor and recording the now uninfluenced donor intensity. Another technique uses differently tagged samples: one sample employs the complete FRET pair, the other only uses the donor fluorophore to analyze the undisturbed donor fluorescence. Here, free acceptor molecules are often still introduced to the corresponding cell compartment to exclude that FRET only arises out of crowding in densely packed environments. The energy transfer can now be quantified by

$$E_{ET} = 1 - \frac{I_{DA}}{I_D} \tag{2.21}$$

where I_{DA} and I_D are the donor intensities with or without the acceptor, respectively. Although equation (2.20) now would allow to calculate of the exact molecular distance, this is uncommon for typical FRET interaction assays. Since any measurable energy transfer infers that the distance between those molecules is below 10 nm and thus points to a direct interaction, this information is usually sufficient for the scope of many experiments.

For live cell imaging applications, the above presented ratiometric approach is subject to certain caveats. The detection of fluorophore intensities is dependent on the excitation power, detection sensitivity, chromophore concentrations, chromophore quantum yields and saturation effects, to name a few. This requires meticulous calibration measurements and precise control over these parameters, which is often problematic for intrinsically variable biological systems. As presented before, the FLT of a chromophore is very sensitive to its nano-environment, including external fluorescence quenchers. In case of FRET, introducing a decay rate constant for the donor-acceptor energy transfer results in a shift of the equilibrium of radiative and non-radiative processes. In consequence, the apparent donor FLT will drop and the energy transfer can be calculated analogously to equation (2.21) by

$$E_{ET} = 1 - \frac{\tau_{DA}}{\tau_D} \tag{2.22}$$

where τ_{DA} and τ_D is the donor FLT with or without the acceptor, respectively. As τ is largely uninfluenced by the abovementioned caveats, the FLIM-FRET combination allows for a much more robust and precise analysis of molecular interactions. For example, it can be used to highlight areas in a live cell image with high energy transfer, pointing to interaction sites on a structural level. More often, the spatial information is used to collect the FLT information only from a certain cell (sub-) compartment for further analysis. FLIM-FRET also can help to uncover both steady state and dynamic interaction processes of proteins in complexes, which are extensively described in literature [21, 22] and will be only briefly addressed here. In a dynamical and heterogeneous biological context, not every putative interactor will bind to its corresponding partner, leading to a mixture of donor subpopulations with different FLTs. Accordingly, the monoexponential fluorescence decay law in equation (2.13) is extended to a multiexponential model:

$$I(t) = \sum_{i=1}^{n} A_i \exp(-\frac{t}{\tau_i}) \tag{2.23}$$

with A_i and τ_i representing the respective amplitudes and FLTs of each subpopulation (or component) i. In case of interaction experiments, this raises the question of how the FLTs τ_{DA} and τ_D should be averaged. The FLTs can be calculated either as the intensity-weighted means

$$\tau_{int} = \frac{\sum_i A_i \tau_i^2}{\sum_i A_i \tau_i} \tag{2.24}$$

which is recommended for dynamic quenching, while the amplitude-weighted means

$$\tau_{amp} = \frac{\sum_i A_i \tau_i}{\sum_i A_i} \tag{2.25}$$

should be preferable for FRET applications, since they are proportional to the steady state intensities [21, 22]. However, as complex interaction patterns or other biological influences on the FRET pair's photophysics cannot always be excluded, τ_{int} proved to be a much more robust parameter [27] that justifies its use also in FLIM-FRET experiments and was consequently used throughout the interaction assays presented in this thesis. Moreover, there seems to be no consistent approach in the data analysis of published FLIM-FRET interaction experiments. While most researchers use the averaged FLTs, some directly compare the FLTs of the fractional components, while others employ strictly monoexponential test functions and only compare the red. chi^2 values to uncover molecular interactions. In case of simple interaction assays with strong interactors, all of these approaches result in reliable data. However, FLIM-FRET is a very powerful technique also for more complex research questions. In that case, the correct photophysical model is essential to arrive at accurate conclusions.

2.2.2 FIDSAM

A major problem in fluorescence imaging techniques is the emergence of autofluorescence, caused by a multitude of luminescing biological molecules that often spectrally overlap with commonly employed fluorescence probes. In many cases, their signal is partly obscured by a strong autofluorescence background, which leads to reduced image contrast and complicates the correct interpretation of fluorescence signals. To varying degrees, this is a troublesome phenomenon in microscopy across many life science disciplines. However, it holds especially true for plant cells and their strongly autofluorescent cell walls that frustrate the analysis of their adjacent cell membranes. This motivated the development of a technique called Fluorescence Intensity Decay Shape Analysis Microscopy (FIDSAM) by Frank Schleifenbaum (IPTC / ZMBP, University of Tübingen) to enhance the dynamic contrast of a fluorescence image by suppressing the autofluorescence contributions [25]. An overview of the FIDSAM principle, applied to a simulated image with high levels of autofluorescence, is presented in Figure 2.8.

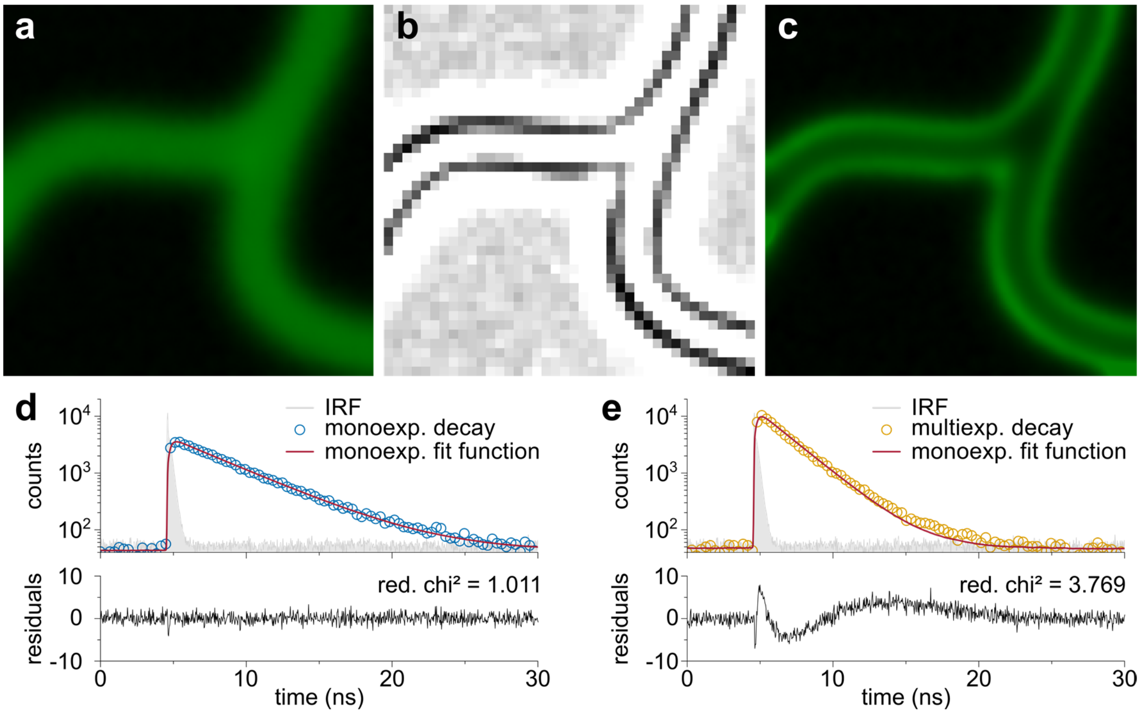

Figure 2.8 | The principle of FIDSAM. (a) Simulated biological structure; autofluorescence dominates the underlying fluorescence label. **(b)** Error image; brighter areas show higher red. chi² values. Pixels are binned for better photon statistics. **(c)** Dividing the intensity values of **a** by a Gaussian blurred version of **b** suppresses all areas with high red. chi² values. The unaffected pixels in the resulting FIDSAM image mainly feature the fluorescent label. **(d)** Monoexponential FLT decay data (blue circles) and IRF (gray), fitted with a monoexponential function (red). The residuals are evenly distributed with a red. chi² value close to unity. **(e)** Analog to **d**, with multiexponential FLT decay data (yellow circles). The residuals show non-random deviations from zero, also reflected in the high red. chi² value.

The analysis was carried out as follows: first, a binning procedure groups the decay data of several pixels into bigger (pseudo-) pixels. The apparent loss in spatial resolution is made up for with better photon count statistics per pixel. Furthermore, areas of autofluorescence are usually much larger than individual pixels in the original image, which makes the lower resolution negligible. Next, a global IRF shift is estimated, which is fixed for all pixels. In reality, the IRF shift might vary in parts of an image, due to inhomogeneities of spectral components and/or refractive indices of the sample. However, working with comparably narrow emission color filters and usually imaging the same kind of cell, tissue or compartment, the deviations are very small. Moreover, calculation of the IRF shift can be error-prone for pixels with low photon counts, so replacing this fitting variable with an average constant makes the results overall more reliable. Now, the data for each pixel is fed into a calculation procedure that convolves the IRF with a monoexponential test function and minimizes the error via an NLLS algorithm, using the red. chi^2 value as the error output parameter (see equations (2.14) and (2.16), also compare the differences in Figure 2.8d and e). It is important that the FLT can still be varied, as a fluorophore's FLT is highly susceptible to its physicochemical environment. Its general decay shape, however, remains largely unaffected. With these error values (signifying the deviation from a monoexponential decay curve) per pixel, an "error map" is constructed (Figure 2.8b), which is resized to the dimensions of the original (not binned) image. Each pixel in the original image now corresponds to an error value that is high for mainly autofluorescence intensity contributions and low if the intensity mainly originates from the fluorescent tag. The FIDSAM image is obtained by dividing each original pixel intensity by the corresponding error value. Only those pixels dominated by the fluorescent tag remain unaffected, while the intensities of pixels with high autofluorescence are subdued (Figure 2.8c). This effect can be amplified by applying an exponent (2, 3, … n) to the error values (which is equivalent to using the FIDSAM routine 2, 3, … n times). A blurring algorithm applies a Gaussian filter to the error map, which evens out smaller deviations and smoothens edges introduced by the pixel binning. The same principle not only applies to the fluorescence intensity, but also to the FLT data of FLIM images, resulting in corresponding FLIM-FIDSAM images.

While this technique performed excellently in a variety of projects [25, 28, 29], it is nevertheless ultimately limited by photon statistics. If the fluorescence tag is expressed very weakly, then a reliable analysis of individual decay curve shapes may be frustrated. While this sometimes can be compensated by pixel binning, the larger number of photons is accompanied by a loss of spatial resolution. Moreover, if the ratio of fluorophore signal to autofluorescence is too low, small unspecific differences may be artificially magnified by the overuse of filters. Apart from such severe cases, many experiments can employ FIDSAM to deal with a strong autofluorescence background to dramatically enhance the contrast, uncovering structures and processes that were formerly inaccessible.

2.3 Single-Molecule Spectroscopy

While many molecular characteristics are derived from bulk analyses, they can only represent the ensemble average properties, typically derived from millimolar sample solutions. Therefore, the signal of a single molecule is very difficult to detect against the overwhelming background and extremely demanding on the hardware of an optical setup. It was only around 1990 that the first single-molecule fluorescence experiments were successfully carried out [30, 31] and they since then became an indispensable tool for molecular physics. It soon became possible to study the behavior of single molecules even at room temperature, revealing subpopulations with different spectral properties that previously remained hidden in the ensemble average [32]. As single molecules are very sensitive to their nano-environment, they also represent optical sensors with a molecular resolution.

The most striking feature of individual chromophores is fluorescence intermittency or blinking, indicating the interruption of excitation-emission cycles by the transition to non-fluorescent states. Apart from long-lived triplet states, dark states ranging from milliseconds to several seconds can have very different origins and are still subject to ongoing research [33]. Blinking statistics can, however, allow access to photophysical properties and processes that are hidden in bulk measurements. Another feature of single-molecule fluorescence also poses a challenge: photobleaching. Organic molecules typically remain in excited states for a few nanoseconds, which makes them susceptible for either internal rearrangement of chemical bonds or external reactions with ubiquitous oxygen. This can destroy the chromophoric system and therefore drastically limits the acquisition time for single-molecule data. While the removal of oxygen, the use of polymer matrices or working at cryogenic temperatures can help to keep a single fluorophore intact over much longer periods, photobleaching is still a limiting factor for single-molecule spectroscopy under ambient conditions, especially in live cell imaging.

Many techniques make use of single-molecule detection to acquire ensemble parameters, for example TCSPC, which was already mentioned in chapter 2.2. Fluorescence correlation spectroscopy (FCS) [34] is a technique that records the intensity trajectories of single molecules as they drift through the observation volume, for example, of a confocal microscope setup. The temporal correlation analysis of intensity fluctuations provides information on concentration, diffusion coefficients, excited state dynamics and more.

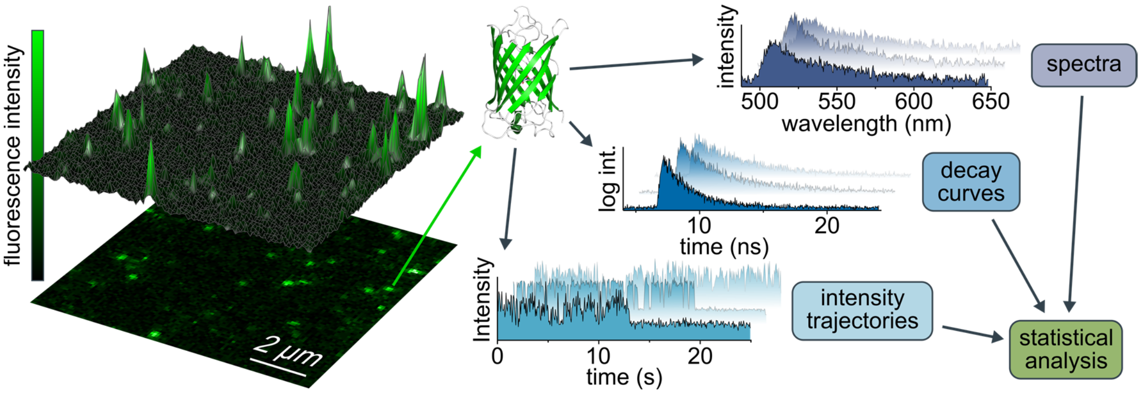

Figure 2.9 | Single-molecule spectroscopy. Left: 2D and superimposed 3D representation of single GFP molecules immobilized in a polymer matrix. Right: each molecule is addressed individually to measure a variety of spectroscopic parameters. The analysis of the single-molecule data often requires the acquisition of hundreds or thousands of individual molecules for a robust statistic.

The single-molecule experiments in this thesis deal in particular with the spectral analysis of individual molecules, which will therefore be discussed in more detail. To address single molecules, a common technique immobilizes the fluorophores by greatly diluting them in a thin polymer film, thus providing sufficient spatial separation. A statistical analysis now reveals the distribution of averaged spectral parameters, offering much more information than ensemble measurements alone (Figure 2.9). This allows to identify spectral subspecies and their dynamical transitions [35]. Inside a spectral subspecies, the absorption and emission maxima are usually statistically distributed around an average value, due to interactions of individual molecules with their nano-environment [36]. It could also be shown that the rigidity of this environment has a direct influence on the spectral distribution width; that is, more flexible systems show a narrower distribution of observed maximum positions [37]. The authors hypothesized that the reason lies in the facility to return to the energetic minimum position prior to fluorescence. A more rigid environment would force a stepwise return, offering more energetic states that a fluorescence photon can be emitted from.

In principle, most biological processes are based on the interaction of single molecules. It is therefore not surprising that single-molecule techniques have also found their way into biological research, for example FRET on single molecules (smFRET) [38], which was applied to numerous scientific questions in live cell experiments.

Although imaging techniques are constantly developed for enhanced sensitivity, they are still limited by the photostability of the molecules themselves. Moreover, the statistical distribution of properties might introduce some research bias in certain experiments. As single-molecule studies are technically demanding, researchers might tend to probe only the most accessible, that is, the most luminous molecules. Limited to optical techniques, dark or very dim molecular subspecies might therefore be omitted and are consequently absent in a full statistical description of a system. With these caveats in mind, single-molecule spectroscopy is nevertheless a seminal technique that can be applied to many research fields, allowing deep insights into photophysical properties and molecular physics.

2.4 Optical Superresolution Techniques

With regard to the resolving power of a classical microscope, superresolution can be achieved by a variety of microscopy methods. Techniques without beam irradiation use a physical probe (usually a tip with a very sharp apex) to raster scan the sample, achieving up to 5 nm lateral resolution for atomic force microscopy and up to 0.1 nm lateral resolution for scanning tunneling microscopy [39]. The related near-field scanning optical microscopy uses tips to sense the near-field of a sample and can reach a lateral optical resolution of 12 nm with specialized setups [40]. Electron or helium ion beam microscopy can typically resolve structures close to 1 nm, taking advantage of the short wavelengths of electrons or ions that are used as the illumination source. However, these methods are mostly used to give topographic information on rigid samples or rely on extensive chemical treatment to produce thin sample slices. This substantially limits their application for live cell imaging, for which optical microscopy remains the method of choice as a non-destructive analysis method. However, the resolution of an optical system is governed by the diffraction of light, which limits the achievable lateral resolution in typical microscopes to 200 nm [11]. As many subcellular structural features and biological processes happen on smaller size scales, they are typically obstructed from direct observation and analysis. This provided the motivation for many researchers to attempt to break or at least circumvent the fixed diffraction limit to achieve higher resolution in the optical regime. Viable techniques gained momentum in the 1990s, and currently many of these so-called optical superresolution methods are used to elucidate structures that were formerly out of reach for classical microscopy. While the Abbe diffraction limit only considers the spectral properties of light, superresolution techniques also exploit the properties of fluorophores as quantum emitters. The ability to switch these emitters between fluorescent and non-fluorescent states is the main principle of all optical superresolution techniques presented here.

Although Stimulated Emission Depletion (STED) microscopy was not applied in the scope of this thesis, it will still be shortly presented in chapter 2.4.1 as one of the pioneer superresolution techniques, along with the general concept of Reversible Saturable Optically Linear Fluorescence Transitions (RESOLFT). Developed in parallel, Single-Molecule Localization Microscopy (SMLM) uses an alternative concept to achieve superresolution, illustrated by the examples Photoactivated Localization Microscopy (PALM) and Stochastic Optical Reconstruction Microscopy (STORM) in chapter 2.4.2. The related method of Superresolution Optical Fluctuation Imaging (SOFI) is based on the same experimental setup, but uses a different analysis principle, discussed in chapter 2.4.3. Finally, SMLM techniques can also be applied to determine single-molecule dynamics, as shown in chapter 2.4.4 for Single Particle Tracking with PALM (sptPALM).

The list of established superresolution techniques and their advancements grows steadily. While they cannot be exhaustively described in this short introductory section, reviews of the most commonly employed methods can be found in literature [41-43].

2.4.1 STED and RESOLFT

The principle of STED microscopy was first introduced in 1994 [44] and later generalized to RESOLFT [45] to denote a group of similar microscopy techniques. RESOLFT is used in microscopy by switching fluorescence markers between states A and B with inhomogeneous illumination featuring at least one point of zero intensity (see Figure 2.10). For this example, the transition A → B will occur everywhere except at such points. By increasing the illumination intensity, the A → B transition saturates and leads to a narrow region of state A around these points, even though the intensity distribution itself will still be governed by diffraction. Consequently, Abbe's equation for the minimal distance of resolvable structures is extended with an additional term in the denominator:

$$\Delta x \cong \frac{\lambda}{2n \sin\alpha \sqrt{1 + \frac{I_{max}}{I_{sat}}}} \tag{2.26}$$

with peak illumination intensity I_{max} bordering the zero and the fluorophore-characteristic intensity I_{sat} at which the A to B ratio equals one. In theory, $I_{max} \to \infty$ would lead to $\Delta x \to 0$, so using reversible fluorescence transitions, this method is repeated for each pixel in confocal scanning microscopy, resulting in images with a higher spatial resolution.

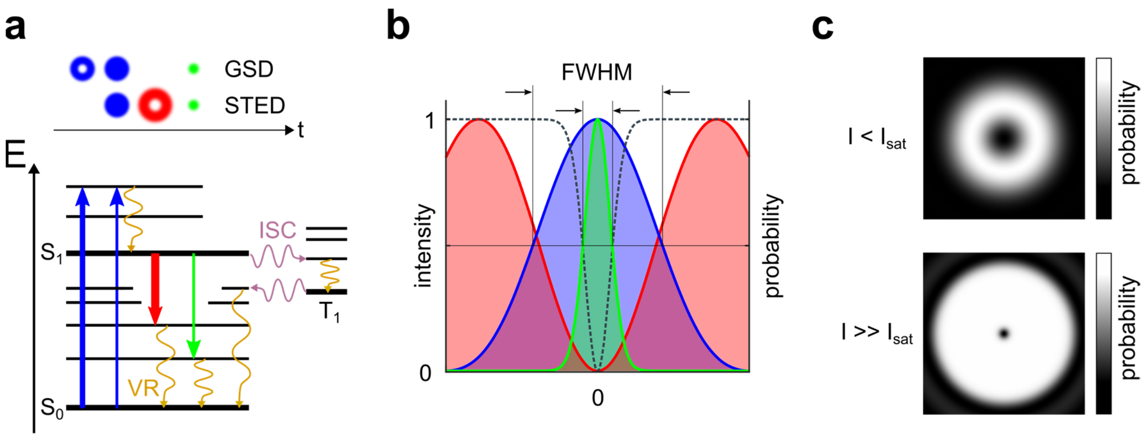

Figure 2.10 | Reversible saturable optically linear fluorescence transitions (RESOLFT) principle. (a) Jablonski diagram showing the corresponding electronic transitions. Ground state depletion (GSD) microscopy uses a donut shaped depopulation beam to excite and push fluorophores into triplet states, subsequently using a Gaussian shaped imaging laser of the same wavelength to address the unaffected fluorophores, leading to a much smaller PSF. Stimulated emission depletion (STED) first excites molecules in a diffraction-limited spot to the first excited state, then uses a red-shifted donut shaped laser to induce stimulated emission. The fluorescence emission of the remaining molecules thus shows a much smaller PSF. **(b)** Intensity profiles of a Gaussian beam (blue) and donut beam (red) used in STED. An intensity depletion beam that is much lower than the saturation intensity I_{sat} will not change the original Gaussian FWHM, however, higher intensities saturate the stimulated emission transition probability (dashed line), leading to a narrow emission PSF (green). **(c)** 2D representations of the transition probabilities as explained in **a**.

The point of zero intensity can be introduced, for example, by passing the laser beam through a commercially available spiral phase plate. By adjusting the refractive index and the pitch of the helical surface to the wavelength of the transmitted light, a helical phase front is imprinted onto the laser beam with a phase singularity in the center with zero intensity. In STED microscopy, the saturable transition takes place between electronic states S_0 and S_1. A diffraction-limited laser beam excites fluorophores from S_0 to S_1

which then can relax by radiative or non-radiative mechanisms. Stimulated emission, induced by a red-shifted, spatially overlapping beam with abovementioned geometry, depletes the excited state, effectively preventing fluorescence from all molecules outside the region in the very center of the focus. Due to the red-shifted depopulation of S_1, the emission of the remaining fluorophores can be detected by suitable color filters. However, the rate of stimulated emission must far outweigh the competing spontaneous emission rate, requiring high intensities I_{max} (compare equation (2.26)) of the depletion beam.

While this superresolution method is theoretically possible with any fluorophore, the technical demands for STED are relatively high. Apart from costly high-powered depletion lasers, the precise alignment of a perfectly shaped STED with the excitation beam and phototoxicity set practical limits to the achievable resolution enhancement. Newer developments discriminate between photon arrival times to further improve the contrast, as stimulated emission also increases radiative decay rates and thus reduces FLTs in regions with high STED beam power. This combination with FLIM, termed time-gated STED [46] features better background suppression, enhanced spatial resolution and requires lower illumination intensities. With repeatedly demonstrated resolutions around 30 nm [43], STED has become an essential superresolution method for many biological research projects.

Another superresolution technique based on RESOLFT is called ground-state depletion (GSD) microscopy [47, 48] that achieves a lateral resolution of around 50 nm. The excitation-emission rate of fluorophores is typically much higher than inter-system crossing rates from singlet to triplet state $S_1 \rightarrow T_1$ and the subsequent relaxation to the ground state $T_1 \rightarrow S_0$. Therefore, high excitation intensities will accumulate molecules in long-lived triplet states, effectively depleting the ground state population. By shaping the depletion beam as mentioned above, the temporary trapping in metastable triplet states only occurs for fluorophores outside the center. The emission of the remaining fluorophores can be subsequently probed with a low-powered Gaussian beam of the same wavelength. After relaxation of all fluorophores from $T_1 \rightarrow S_0$, the next point is addressed, yielding superresolution images from the sample in confocal scanning microscopes. Since triplet state lifetimes are typically on the order of milliseconds, this practically limits the acquisition speed for GSD microscopy. Although requiring only moderate illumination intensities, the control of photobleaching, inter-system crossing rates and triplet lifetimes are essential to ensure sufficient ground state depletion with optimized recording speeds. These photophysical parameters are often adjustable by changing the environmental conditions with suitable buffers [47].

Other RESOLFT methods use specialized fluorophores such as photoswitchable fluorescent proteins that feature a saturable transformation between two conformational states with much lower I_{sat} and therefore much lower required illumination intensities [45]. However, these transitions are significantly slower than the settling of electronic states in STED, thus the acquisition speed is accordingly slower. As in the case of STED and GSD, the precise spatial alignment of excitation and depletion beam is a main factor for the achievable resolution enhancement.

Recently, a new optical superresolution method called MINFLUX was published [49], resolving molecules only 6 nm apart with 1-nm precision. Similar to RESOLFT methods, a ring-shaped excitation pattern addresses single emitters. Here, the localization precision will be highest when the emitter coincides with the central intensity minimum of the excitation beam and thus shows no fluorescence at all. Minimal deviations from the exact center will result in a photon flux, so sampling in a small triangular search pattern around the center offers high localization precision with only minimal photon counts. To ensure that single, separable emitters are present, photoactivatable or -switchable fluorophores are activated in only small subsets. Afterward, a diffraction limited overview image is acquired with low illumination intensity to reveal the approximate single emitter positions, then the laser beam with the zero-intensity minimum addresses each emitter in the abovementioned pattern, controlled by a fast beam-scanning mirror. This approach also applies to the tracking of single fluorescent molecules with high spatiotemporal resolution. In contrast to STED, this technique works with low illumination intensities and small photon budgets, thus showing great potential for the application in life sciences due to low sample stress and reduced fluorophore bleaching.

2.4.2 PALM and STORM

Approximating a single emitter PSF with a 2D Gaussian function allows to determine its center with high precision. However, if a heavily stained specimen is investigated, the diffraction-limited image of a fluorescent structure consists of millions of overlapping individual emitter PSFs. Their necessary separation now takes place in the time domain, that is, recording movies instead of a single image, making sure that each frame features different subpopulations of sufficiently isolated single emitters. Since the data collection usually spans several hundred frames with low photon counts, wide-field imaging techniques must employ fast and sensitive digital cameras that typically use imaging sensors based on electron-multiplying charged-coupled devices (EMCCD) or complementary metal-oxide-semiconductors (CMOS). Depending on the sample, further contrast enhancement can be achieved by different illumination modes (see TIRFM, VAEM in chapter 2.1). In the ideal case, each emitter is sampled at least once, and the original image is reconstructed by plotting all emitter positions with higher precision, resulting in superresolution imaging. These techniques fall within the category of Single-Molecule Localization Microscopy (SMLM). A short overview of the main principle is presented in Figure 2.11.

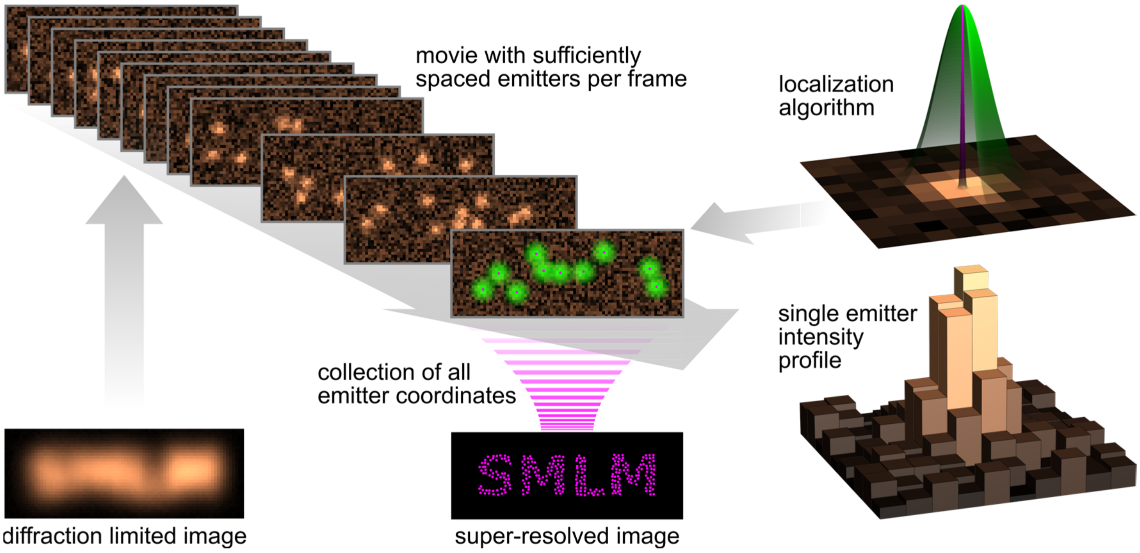

Figure 2.11 | Main principle of single-molecule localization (SMLM) superresolution techniques. As fine structures in diffraction-limited fluorescence images are obscured by overlapping emitter point spread functions (bottom left), wide-field image stacks are recorded that feature stochastic subsets of spatially separable emitters. Computer-aided processing of each frame in the stack localizes individual emitter positions (top right) by fitting them with 2D Gaussian functions (green) with high precision (magenta). All emitter coordinates are compiled into one image, now revealing structures beyond the diffraction limit (bottom middle).

A technique called (fluorescence) photoactivated localization microscopy ([F]PALM) [50, 51] uses special fluorophores or fluorescent proteins (FPs) as markers that can be switched between two optical states. Photoactivatable FPs can be switched from a native dark form to a fluorescent form, while photoconvertible FPs can be switched to spectrally red-shifted species (thus they are natively “dark” in the red channel). This enables to activate a small, random emitter subset (typically by short exposure to light around 400 nm), which is then excited with a different wavelength and detected until photobleached. For the next frame, another random emitter subset is activated, and so on, until all emitters in the specimen have been recorded.

Stochastic optical reconstruction microscopy (STORM) [52] was developed independently and employs the same principle with different markers. Here, the photoswitchable organic dye pair Cy3-Cy5 was used to ensure spatially separated emitters per movie frame, but this method is also applicable to photoswitchable FPs like Dronpa. As this process is reversible, one fluorophore can cycle multiple times between its fluorescent and dark forms before it is photobleached.

The intrinsic fluorescence intermittency of individual chromophores was later exploited for the closely related techniques direct STORM (dSTORM) [53, 54], spectral position determination microscopy (SPDIM) [55] and ground-state depletion followed by individual molecule return (GSDIM) [56]. They all rely on light-induced transitions of single fluorophores to long-lived dark states (typically via excited triplet states) from which they can stochastically return to the fluorescing state.

As emitter subsets no longer need to be manually activated and photobleached, this technique acquires images continuously under constant illumination, which drastically increases data collection speed. However, the blinking frequency of individual emitters must be adjusted to the camera acquisition frame rate to adhere the above requirements of SMLM. The photoswitching depends on several parameters that are summarized in this technical review [57] and will be shortly described here. Usually the specimen is immersed in a special imaging buffer including an enzymatic oxygen scavenger system. The removal of oxygen is essential to reduce photobleaching, but its complete absence as a triplet quencher prolongs dark states and reduces the overall photon flux. Consequently, reducing agents like 2-mercaptoethanol are added as both alternative triplet quenchers and to control dark radical states originating from redox reactions. Moreover, completely reduced forms can be driven back to fluorescence states by photooxidation, allowing further control by illumination with 400 nm. In principle, all conventional organic dyes are suitable for dSTORM due to their natural blinking behavior. The composition of the imaging buffer and the photon statistics of the dye have, however, great influence on the resulting image quality.

The large variety of spectrally distinct fluorophores for PALM and STORM also allows for sequential or parallel multicolor experiments, if their illumination and detection schemes do not introduce undesired crosstalk.

Data evaluation is a central part of all SMLM techniques to reconstruct images with superresolution. The first step for each frame is to apply a segmentation algorithm that finds isolated fluorescence spots. Depending on specified quality parameters, overlapping or distorted spots are already filtered out at this point. Each remaining spot is now fitted with a 2D Gaussian function to determine each corresponding underlying emitter position. Assuming a two-dimensional, isotropic system, the localization error (or precision) along the x-axis is given by

$$\Delta x_{loc} = \sqrt{\frac{s^2}{N} + \frac{a^2/12}{N} + \frac{8\pi s^4 b^2}{a^2 N^2}} \tag{2.27}$$

with the standard deviation s of the emitter PSF approximated by the two-dimensional Gaussian function, the number of detected photons N, pixel size a of the image sensor and standard deviation b of the background. The first term shows the dependency of the localization precision on the photon shot noise. The second term results from the uncertainty of where a photon arrived in a pixel of finite dimensions and can be dominant for undersampled images. On the other hand, oversampling spreads the PSF over too many pixels, leading to worse signal-to-noise ratios. The Nyquist-Shannon sampling theorem [58] states that an analogue signal must be sampled with at least twice its frequency to digitize the signal without loss of information. Applying this principle to pixel sizes on digital image sensors, the PSF should spread over at least two image pixels, which can be achieved with suitable optics in front of the camera (see chapter 4.2.5 for a detailed calculation). The third term in equation (2.27) describes background noise that arises from the sample and the detector itself. Due to the electronic signal processing of EMCCD cameras, their detector noise can be assumed as a constant pixel offset.

However, CMOS cameras feature analog-to-digital converters for each pixel and therefore pixel-dependent noise statistics. The use of calibration images (noise maps) and CMOS-specific localization algorithms [59] can therefore make a significant difference, in particular for experiments with low photon counts.

If the photon flux per emitter is high, equation (2.27) simplifies to

$$\Delta x_{loc} = \frac{s}{\sqrt{N}} \tag{2.28}$$

and the localization precision only depends on the number of collected photons. Therefore, the right choice of the fluorophore is an essential factor for superresolution imaging. The average photons per switching event, on/off duty cycles, photostability and number of switching cycles are important parameters that have been evaluated for the most common organic dyes [60]. Corresponding evaluations [61] also exist for FPs and their use in PALM, additionally taking into account protein maturation times and oligomerization tendencies. By now, almost every spectral range can be addressed with fluorescent probes specifically tailored for their use in PALM and STORM. Further developments are nevertheless necessary to ensure their robust use in challenging situations that especially arise in life cell imaging.

The labeling efficiency of particular structures can also influence the image resolution. The Nyquist-Shannon sampling theorem applies here as well: to resolve structural features of a certain size, they must be covered with at least two data points, such as fluorescence labels. Insufficiently labeling might introduce gaps in superresolution images, which can easily be misinterpreted as missing structural features. Excessive or clustered labeling, on the other hand, might frustrate the acquisition of isolated emitters in each frame. Therefore, control of the labeling density is crucial to achieve the best possible resolution. Moreover, depending on the labeling technique, up to 20 nm can be introduced between the structure and fluorophore, which represents a limiting factor for the localization precision of the original features.

In vivo applications also deal with other factors that influence the achievable resolution. Sample autofluorescence can introduce artifacts or decrease the signal-to-noise ratio, thus impairing the photon statistics. Moreover, sample or stage drift can limit the viable acquisition time. While lateral movement can sometimes be corrected by the use of fiducial markers as reference points, the correction of axial movement requires hardware-based solutions like automated focus systems.

Despite these complexities, superresolution techniques like PALM and STORM regularly achieve a lateral resolution of 50 nm in live cell applications [62]. In 3D STORM, the axial resolution could be improved to 50-60 nm by introducing optical astigmatism (for example, with a weak cylindrical lens) to change the ellipticity and the orientation of the PSF depending on the emitters' position in z [63].

It should be pointed out that the term "superresolution" or "breaking the diffraction limit" is misleading in the context of SMLM as the resolution power of the optical microscope remains unchanged. Strictly speaking, due to the spatial isolation of single emitters in the time domain, their localization precision is no longer dependent on the diffraction limit. Despite this necessary distinction, superresolution has since become widely used as a comprehensive term for a variety of techniques that manage to resolve structures beyond the limits of classical optical microscopy, but still work within the physical bounds of diffraction limited optics.

2.4.3 SOFI

SOFI analyses the fluorescence intermittency of emitters to produce background-free, contrast-enhanced images with a resolution below the diffraction limit [64]. In contrast to the superresolution techniques presented in chapter 2.4.2, SOFI requires comparably few conditions. It can be applied to multiple imaging methods, but is most commonly used in wide-field microscopy with EMCCD or CMOS cameras. The employed fluorescent labels must have at least two optically distinguishable emission states, for example, fluorescent and non-fluorescent, and they have to switch between these states independently from each other stochastically. Therefore, this method shows many parallels to dSTORM. SOFI, however, does not require isolated emitters in time and space, but only intensity fluctuations in each pixel, caused by the random intensity contributions of all nearby, activated fluorophores.

In general terms and very briefly, SOFI uses higher-order statistics to analyze the origin of the intensity fluctuations. This is achieved by autocorrelation, which is the correlation of a signal with a time-shifted copy of itself as a function of the time shift. Since a single emitter will only fluctuate between two states, its signal will be highly correlated. If the intensity fluctuations originate from multiple emitters, the correlation decreases and is lowest for uncorrelated background noise. In SOFI, this is used to reduce the effective PSF width, thus not only providing better contrast, but also a higher image resolution (Figure 2.12).

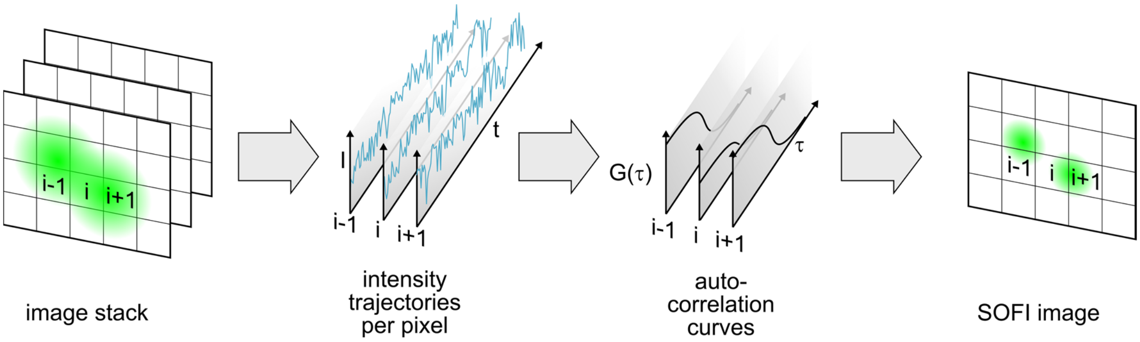

Figure 2.12 | Superresolution optical fluctuation imaging (SOFI) principle. A recorded image stack with overlapping emitters is analyzed by extracting the fluctuating intensity trajectories per pixel. Autocorrelation analysis can discriminate if the signal originated from a single emitter or from overlapping emitters / background. This information is used to enhance the contrast in the SOFI image. Adapted from [64].

While the exact mathematical description is given in [64], only its main points will be presented in the following. The fluorescence source distribution of N single, independently fluctuating emitters at position $\boldsymbol{r}_k$ is given by

$$\sum_{k=1}^{N} \delta\,(\boldsymbol{r}-\boldsymbol{r}_k)\cdot \varepsilon_k \cdot s_k(t) \tag{2.29}$$

with constant molecular brightness ε_k and time-dependent fluctuation $s_k(t)$. Assuming fixed emitter positions and a constant system PSF $U(\boldsymbol{r})$, the fluorescence signal is then given by

$$\delta F(\boldsymbol{r},t) = \sum_{k=1}^{N} U\,(\boldsymbol{r}-\boldsymbol{r}_k)\cdot \varepsilon_k \cdot \delta s_k(t) \tag{2.30}$$

expressed here for zero-mean fluctuations. The correlation of intensities requires a second-order function, therefore the equation for the second-order autocorrelation function $G_2(\boldsymbol{r},\tau)$ becomes

$$G_2(\boldsymbol{r},\tau) = \sum_{k=1}^{N} U^2\,(\boldsymbol{r} - \boldsymbol{r}_k) \cdot \varepsilon_k^2 \cdot \langle \delta s_k(t+\tau) s_k(t) \rangle_t \tag{2.31}$$

with time shift τ and time average $\langle \dots \rangle_t$. This rather simple form can be assumed because the signal of different emitters is not time-correlated, therefore all cross-correlation terms can be disregarded. As the SOFI image relies on the value of $G_2(\boldsymbol{r},\tau)$, the PSF is replaced by the square of the original PSF, resulting in a resolution enhancement of $\sqrt{2}$.

Higher order correlation functions are calculated from nth-order cumulant functions to ensure the elimination of cross-terms and result in a resolution enhancement of $\sqrt{n}$. Although simplified calculations of cumulants are algorithmically easy to realize, they are beyond the scope of this section. The use of higher order functions also has practical limitations. Higher statistical orders also enhance the dynamic intensity range in the image non-linearly, which can lead to artifacts or the concealment of dim emitters. After the generation of a SOFI image, it is typically further deconvolved with the Richardson-Lucy-algorithm, if the PSF can be estimated reliably.

For a more precise estimation of the underlying PSF, further developments of the SOFI algorithm use Fourier reweighting schemes and spatio-temporal cross-cumulants that also include the information of circumjacent pixels [65]. The nonlinear response to brightness and blinking heterogeneities in the sample can be mitigated by including estimated blinking statistics in the calculations [66]. SOFI presents as an easy-to-use, robust superresolution method with low demands on labeling and instrumentation. While SMLM techniques like STORM can deliver higher resolution enhancements, SOFI can work more consistently over different blinking dynamics [67] and is also less vulnerable to sample and stage drift due to much shorter acquisition times. Accordingly, SOFI is considered a viable alternative to the localization-based superresolution techniques presented in chapter 2.4.1, depending on the sample and scope of the experiment.

2.4.4 sptPALM

The cell membrane is the interface between the intra- and extracellular world and thus hosts numerous highly dynamic processes to fend off pathogens and to control the in- and efflux of metabolites and information. Many of these processes are mediated by the action of membrane proteins that are therefore an integral part of current biological research. As explained in chapter 2.3, the analysis of single molecules offers a wealth of information when compared with the properties of the ensemble. This also holds true for the heterogeneous dynamics of single membrane proteins and, consequently, requires to track their movement within cell membranes with high spatial and temporal resolution, typically beyond 100 nm in the millisecond regime. Ever since single particle tracking could be applied to live cells [68], it evolved into a well-established tool for the statistical characterization of membrane dynamics [69, 70] and will be shortly outlined below.

As this technique depends on localizing membrane proteins tagged with single fluorophores, it shares many requirements that were described for single-molecule detection (chapter 2.3) and superresolution methods (chapter 2.4.2). In contrast to PALM or STORM, single molecules are now observed for as long as possible with relatively low excitation intensities to avoid premature photobleaching. The resulting low signal-to-noise ratio thus places especially high demands on the camera. Moreover, high frame rates with acceptable noise levels are essential to address fast dynamic processes.

Since the cell membrane is the outer boundary of single cells, it represents the compartment that will be closest to the coverslip when they are attached to the surface. Accordingly, image contrast can be vastly improved by the use of TIRFM illumination. In case of more complex organisms, they can be gently pressed onto the coverslip to bring the outer membrane of several cells into the evanescent field. Plant cells with thicker cell walls correspondingly benefit from VAEM illumination to reach their cell membranes.

To achieve high localization precision of single emitters over time, the fluorophore density is also of great importance. Due to the abundance of most membrane proteins, their co-expression with FPs as fluorescence markers may result in many overlapping fluorescence spots, which greatly impairs their correct localization. Moreover, if they move around and cross paths with other emitters, the time one emitter can be reliably tracked is severely limited. While other labeling techniques such as the SNAP-tag [71, 72] or CLIP-tag [73] allow for a better control of the emitter density itself, photoactivatable or -convertible FPs offer a quite elegant solution. Even if all membrane proteins of interest are tagged with these FPs, the density of their visible, fluorescent population can be controlled with an activation laser to make sure that their fluorescent spots are sufficiently isolated. Moreover, once some emitters are photobleached, others can be activated, which theoretically gives access to all tagged membrane proteins. The combination of single particle tracking with FPs that were originally developed for PALM applications was termed sptPALM [74] and allows excellent synergy with superresolution techniques.

After the localization procedure for each image frame, high-resolution particle trajectories are built by linking the particle coordinates. For this, mathematical algorithms have to take into account preceding and subsequent frames, gaps by missed localizations or blinking fluorophores, the crossing of particle trajectories and other uncertainties. A detailed description and comparison of single particle tracking algorithms is, however, beyond the scope of this section can be found in the literature [75].

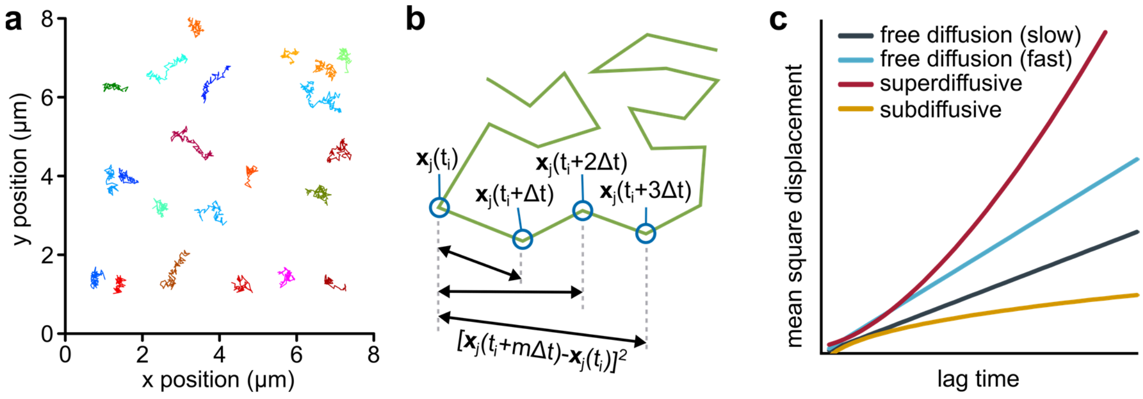

Figure 2.13 | Particle trajectory analysis and mean square displacement (MSD) plots. (a) Typical example of particle tracks recorded from single fluorescence-tagged proteins moving in a live cell membrane. **(b)** Calculation of MSD values for a single particle trajectory (green), as described in equation (2.34). **(c)** Exemplary MSD plots of Brownian movement (free diffusion) with a low (black) or high (green) diffusion coefficient, superdiffusive behavior (magenta) and subdiffusive behavior (orange). Adapted from [70].

Once the particle tracks are found (Figure 2.13a shows exemplary trajectories), movement and diffusion parameters can be calculated. The mathematical framework for the spatial extent of random motion was famously laid in Einstein's investigations of the theory of the Brownian movement [76]. Accordingly, if the motion of each particle in an ensemble starts in a coordinate system from the same point at $t = 0$, the ensemble will have the density

$$f(x,t) = \frac{n}{\sqrt{4\pi Dt}} e^{-\frac{x^2}{4Dt}} \tag{2.32}$$

with displacement x at time t, number of particles n and diffusion coefficient D. From this, the mean square displacement (MSD) of a particle relative to its original position is calculated and applied to two-dimensional diffusion problems that are relevant for the movement in cell membranes:

$$MSD(t_{lag}) = 4Dt_{lag} \tag{2.33}$$

with t_{lag} as the sampled time interval or lag time. Consequently, in case of Brownian motion (unrestricted diffusion), the MSD plot will assume a linear form where the diffusion coefficient is directly linked to the slope (Figure 2.13c, black and blue). For the recorded particle tracks, such plots are derived by calculating the MSD for each time interval that can be applied to the trajectories [70]:

$$MSD(t_{lag} = m\Delta t) = \frac{1}{N-m} \sum_{i=1}^{N-m} \left[x_j(t_i + m\Delta t) - x_j(t_i)\right]^2 \tag{2.34}$$

with position coordinates x_j of particle j that are sampled at N discrete times, where the values for t_{lag} are defined as Δt (the smallest time difference between two localizations, such as the frame acquisition time in a recorded movie), multiplied by the interval distance m (= 1, 2, 3 ...), thus the track's start and end determine the largest possible interval (see Figure 2.13b). This also means that distances for smaller lag times can be sampled more often than for larger lag times, for example, there is only one data point from the first to the last frame of a specific track. Therefore, the statistical significance decreases toward the averaged larger lag times.

While applying equation (2.33) to real particle tracks now would allow for the direct estimation of diffusion coefficients of membrane proteins, the heterogeneous environment of cell membranes seldom permits free diffusion. Many biological systems feature anomalous diffusion types that are better described by including a power law with α as the so-called anomalous exponent:

$$MSD(t_{lag}) = 4D{t_{lag}}^{\alpha} \tag{2.35}$$

Active transport or flow gradients result in $\alpha > 1$, as the particle is pulled in a certain direction (Figure 2.13c, red), while $\alpha < 1$ indicates restricted or confined motion, for example due to the trapping of a protein in membrane subdomains (Figure 2.13c, yellow). These types of motion are of course also highly interesting for the analysis of membrane dynamics and can be further quantified by

$$MSD(t_{lag}) = 4Dt_{lag} + \left(v \cdot t_{lag}\right)^2 \tag{2.36}$$

for directed motion with speed v [77] and

$$MSD(t_{lag}) = \frac{L^2}{3}\left(1 - e^{-\frac{t_{lag}}{\tau}}\right) \tag{2.37}$$

for confined motion with L as the apparent domain size and τ as the characteristic equilibration time after the boundary effect appears in the MSD plot [78].

Accounting for all particle tracks in a measurement, ensemble MSD plots can be calculated for better statistics, especially for larger time tags. Even with non-uniform diffusion, average diffusion coefficients may still be extracted [79]. However, this also obscures the heterogeneity of membrane protein dynamics, which is the most interesting aspect of the subpopulation analysis and the dynamic organization of cell membranes. This will be discussed in greater detail with experimental data in chapter 3.5.3.

The application of sptPALM in live cell imaging applications is also subject to some caveats. While the uncertainties of track linking have been mentioned above, the localization precision for sptPALM is usually lower than for other superresolution experiments, as each emitter position must be determined from the photon output in a single frame. These localization errors are sometimes visible in the MSD plots as a nonzero offset, which must be taken into account prior to further calculations.

Diffusion coefficients are dependent on the size of the protein and can thus be influenced by the markers, in particular for smaller proteins. Just as in PALM, the fluorophore has a decisive influence on the success of the experiment (see chapter 2.4.2).

The acquisition parameters are equally important: high frame rates increase the temporal resolution, but at the same time decrease the spatial resolution, high illumination intensities increase the signal-to-noise ratio but limit track lengths due to photobleaching.

Therefore, the right balance of these parameters must be adjusted for a particular experiment.

As mentioned before, stage and sample drift can be corrected to some extent by software and hardware measures. However, phototoxicity induced by laser illumination can lead to cell contraction, which translates to an apparent directed motion of membrane proteins and cannot be corrected for by normal means.

Assuming the careful consideration of the abovementioned challenges, the study of individual molecule dynamics with sptPALM is a very powerful method to gain deeper insights into the role and characteristics of membrane proteins. The labeling with spectrally different FPs also offers multicolor experiments that, for example, can enable interaction assays. Moreover, the diffusion coefficients determined with sptPALM can be cross-checked with results from other single-molecule techniques like FCS, allowing for the inter-methodological verification of measurements.

2.5 Applied Techniques of Cell Biology

For the success of a spectroscopy experiment, the quality of the sample and the biological context can be decisive. Particularly in fluorescence spectroscopy, a basic knowledge of the fluorescence markers and the labeling technique is highly beneficial. It does not only provide crucial information to interpret results, but also allows for the anticipatory refinement of the system as sample cultivation and preparation often constitute a time-consuming bottleneck in biological research.

In addition, the publication-based projects described in chapter 3 mention many biochemical and molecular biology methods. Since the interpretation of experimental results become more robust when different methods lead to the same conclusions, they serve to validate the spectromicroscopy techniques. The basic working knowledge and limitations of the most important biological procedures referenced in this thesis will be shortly outlined in the following section.

2.5.1 Fluorescent Proteins (FPs) as Biological Markers

Since the first report [80] on the *Aequorea victoria* jellyfish's Green Fluorescent Protein (GFP) in the 1960s, it took almost 30 years until the sequencing of its genetic code [81] allowed its first demonstration as a genetically encodable fluorescent marker [82]. One of the most peculiar structural features of this protein is that it folds into a protective β-barrel [83] (Figure 2.14, left), which enables the autocatalytic chromophore formation (Figure 2.14, right) involving three amino acids in its interior [84]. The importance of GFP in biological research was rising rapidly, not least because structure-based mutagenesis allowed for the optimization and diversification of its photophysical properties. While straightforward mutations of the chromophore resulted in new spectral variants [84], so did mutations of the protein shell [85], underlining the shell's role as the nano-environment for the chromophore. Another expansion of the available spectral range started in 1999, when analogous FPs were extracted and cloned from other marine organisms [86], producing red-shifted classes like red fluorescent protein (RFP) and many other variants with colorful names like mCherry [87]. To this date, researchers have engineered countless variants covering the entire visible spectrum, enabling the use of generally termed fluorescent proteins (FPs) across research disciplines in a wide range of applications [88].

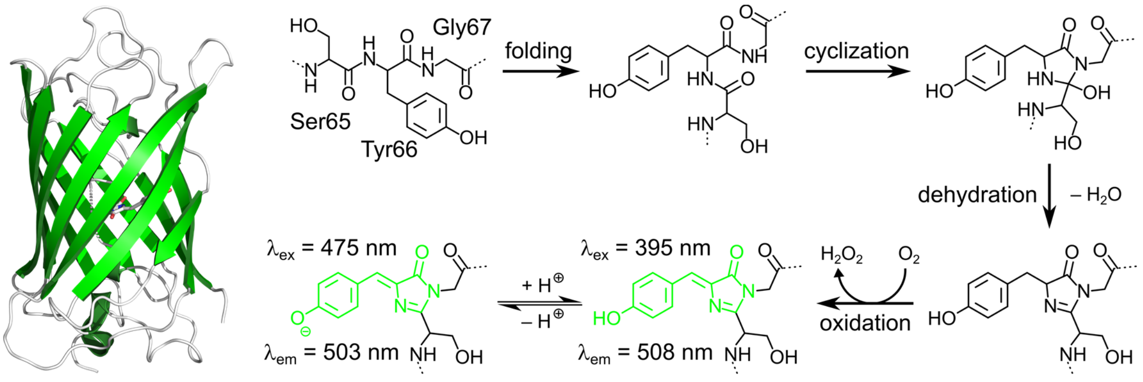

Figure 2.14 | The green fluorescent protein (GFP). Left: tertiary barrel structure of *Aequorea victoria* GFP formed out of eleven β-sheets. Right: posttranslational, autocatalytic chromophore formation.

The labeling of a target protein with FPs is usually done on the genetic level. The genetic sequence encoding the target protein is associated with a regulatory sequence such as the promoter that controls the transcription of the DNA sequence to mRNA and its subsequent translation to the target protein. By inserting the FP gene next to the target protein gene, their translation products are now expressed as one combined amino acid sequence, subsequently folding into the target protein and its covalently attached fluorescent marker. This step may already present some challenges, as the fused proteins might influence or even prevent each other’s correct folding. Depending on the position of the FP, it also might block localization sites or specific interactions. However, this can be mediated by encoding a small amino acid linker between the target protein and its marker or by changing the fusion terminus. The highly variable duration of FP maturation, that is, the folding and subsequent autocatalytic chromophore formation, can range from minutes to hours, reducing their usefulness to resolve the kinetics of protein expression [89]. Another limiting factor for the application of FPs is their size. While the molecular weight of organic dyes is typically below 1000 g/mol (1 kDa), GFP is a protein of about 27 kD. Thus, it might act as a proverbial "ball and chain" when connected to a similar or smaller sized target protein, possibly influencing its physiological properties.

Despite these limitations, fluorescent proteins are unparalleled in their applicability and adaptability to countless biological experiments (see Figure 2.15 for typical applications). While not as bright and stable as organic dyes, FPs can be expressed endogenously, thus their cell toxicity and influence on normal physiological functions is relatively low in comparison to other labeling methods.

For the use of FPs in (FLIM-)FRET interaction assays, additional factors must be considered. Due to their β-barrel structure, the minimal distance of two FPs is approximately 3 nm, thus slightly limiting the dynamic range of FRET. While the orientation factor κ^2 for two freely rotating FPs in solution can be averaged to 2/3, this might not be true for protein fusions. For example, rotational restriction in protein complexes might lead to a predominantly perpendicular orientation of their transition dipole moments, thus negating energy transfer despite their close vicinity. Although such a hypothetical case is mostly negligible for interaction studies, the uncertainty of κ^2 for tethered FPs can limit quantitative distance measurements.

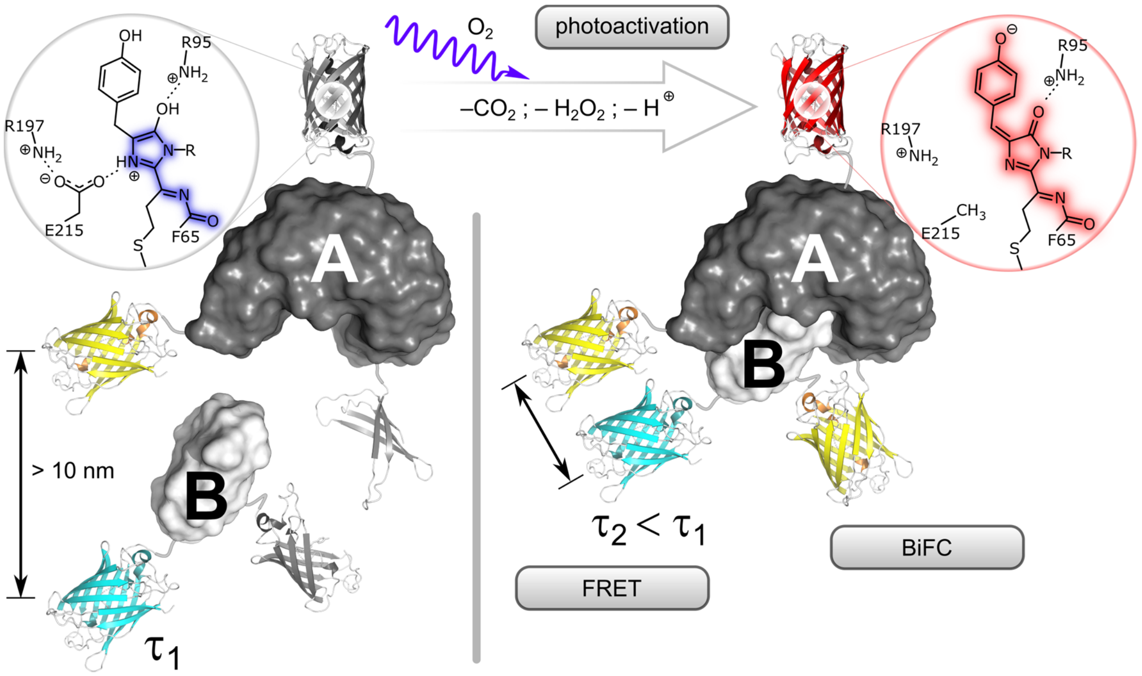

Figure 2.15 | Applications of fluorescent proteins in biological research. The interaction of two proteins A and B can be analyzed with Förster Resonance Energy Transfer (FRET) when A and B are labeled with a suitable FRET pair (blue and yellow), bringing the labels into close vicinity when A and B interact. In FLIM-FRET measurements, this shows in the lowered donor FLT. Alternatively, interactions can be probed by Bimolecular Fluorescence Complementation (BiFC), with A and B being labeled with the fragments of a split fluorescence protein (gray). Interaction of A and B also brings the fragments into close range, which fold to reconstitute their fluorescence. Photosensitive fluorescent proteins (top) are commonly used as labels in superresolution microscopy and change their spectral properties upon photoactivation due to intramolecular reactions or rearrangements of the chromophore.

The position of FPs in the target protein sequence also has a decisive influence. If they are tethered to unfavorable ends of an interacting protein complex, the interchromophoric distance might be outside the detectable FRET range of 7-8 nm for common FRET pairs. This can be mediated by the change of the fusion termini, possibly putting the FPs closer together when the target proteins interact. However, false negatives must always be considered with this method. Furthermore, the kinetics of protein-protein association of different interactors is hardly comparable without precise structural knowledge of the interaction complexes, if only the amount of energy transfer of their fluorescent markers is considered. In case of multimeric complexes with unequal stoichiometry, one donor might be surrounded by several acceptors, resulting in higher energy transfer rates. The exchange of donor and acceptor can therefore produce very different outcomes. However, this can also be turned into an asset to elucidate the structure of such complexes.

Another problem might arise if donor and acceptor fusion proteins are expressed in very different quantities. Although FLT based FRET experiments are much more robust in this respect than those based on intensity, even for FLIM-FRET assays, an excessive donor fraction might obscure the signal of only few complete donor-acceptor pairs. Therefore, it is always advisable to inspect the protein expression levels via respective color channels in live cell imaging, particularly because they even might differ from cell to cell due to biological diversity. Recently, a new cloning system was developed to improve the co-expression of two customizable genes with comparable quantities in combination with state-of-the-art FPs for (FLIM-) FRET experiments [90].

Aside from FRET experiments, FPs are also often used in Bimolecular Fluorescence Complementation (BiFC) interaction assays. This method exploits the tendency of two non-fluorescent FP fragments to reassemble their native tertiary structure with subsequent maturation of the chromophore. By fusing the FP fragments to target proteins, the interaction will also bring the fragments into close vicinity, which can be read out by the emerging fluorescence of the completed FP (see Figure 2.15). The application as a tool for interaction studies was first shown for GFP [91] and later for yellow fluorescent protein (YFP) [92], hence the alternative name “split-YFP assay”. However, it could be demonstrated that this method is not only extendable to other FP mutants, but can also use fragments of spectrally different FPs to produce functional BiFC complexes with new spectroscopic properties [93]. This provided an approach for multicolor BiFC analyses that can visualize multiple protein interactions in the same cell by spectral discrimination. The most striking advantage of BiFC is that the interaction signal is measured against a zero-background signal. This facilitates the visualization of protein-protein interactions with physiological expression levels or interactions of only small subpopulations.

However, BiFC complex formation is dependent on the productive collision of its fragments, which might be prevented due to sterical reasons (false negatives). This is mediated by using longer linkers or changing the fusion termini. Generally, BiFC is less susceptible to this aspect as the complex formation is deemed irreversible [94], thus allowing for larger initial distances as long as the fragments can successfully complement each other at one point. While this irreversibility also allows access to transient interactions, it also presents major drawbacks. High expression levels of the fragments might facilitate their spontaneous association (false positives). They may also act as an unphysiological linker to otherwise transient protein complexes thus rendering the study of interaction kinetics largely impossible. Nevertheless, BiFC is an important analysis tool for in vivo protein-protein interactions, not only as an alternative to (FLIM-)FRET experiments, but also in combinations such as BiFC-FRET for the analysis of multimeric protein complex formation [95].

2.5.2 Functional Expression of Fusion Proteins in Plants

In plant science, the introduction of the foreign genetic material is typically done by a process called *Agrobacterium*-mediated transformation [96]. *Agrobacterium tumefaciens* is a plant-pathogenic bacterium that carries the Ti-plasmid (a tumor inducing, circular piece of double-stranded DNA) that is partly inserted into the plant's genome. This natural ability for genetic engineering is exploited by replacing the pathogenic sequences with custom sequences, using the bacteria as so-called vectors. The customized plasmids are typically constructed in vitro by standard molecular biology techniques and amplified in *Escherichia coli* bacteria before transferring them into *A. tumefaciens* by electroporation or chemical transformation. As the DNA insertion happens at random points in the plant's genome, the plasmid must carry a promoter, the target protein gene and the FP gene to ensure the expression. Instead of the native promoter that is naturally associated with the target protein, often the 35S promoter of cauliflower mosaic virus is used for high levels of gene expression. Accordingly, the overexpression of certain proteins can lead to artifacts and abnormal cell reactions, obscuring the biological processes under physiological conditions. Depending on the experiment, plants can undergo transient or stable transfections. If a temporal expression of the tagged target protein is sufficient, tobacco (*Nicotiana benthamiana*) is the favored model organism to study the distribution and dynamics of proteins in planta. Infiltration with *A. tumefaciens* is commonly carried out by injecting the bacterial suspension into the tobacco leaves. The altered gene expression levels are typically highest after 2-3 days, after which the corresponding areas are excised and analyzed. Stable transformations of the plant model organism *A. thaliana* are routinely realized with the floral dip method [97]. Here, the above-ground parts of flowering plants are dipped into a solution containing *A. tumefaciens*, often resulting in 1% of transgenic progeny seedlings [98], which is rather striking considering the simplicity of the method. Although requiring only minimal practical effort, the generation of stable lines is very time-consuming, as it relies on plant growth and can take up to several months. Starting from the construction of a plasmid carrying the desired sequence to the successful expression of the fusion proteins in planta, many obstacles can arise. Often, the resulting gene products are toxic to the cells, while in other cases, cells simply resist the DNA insertion or silence the sequence. Accordingly, the choice of transformation vectors for the Ti-plasmid and the appropriate strain of *A. tumefaciens* may prove critical. To ensure correct gene expression, the sequence should also be adapted to the host's DNA machinery by codon optimization.

2.5.3 Fixation

When the experiment mainly focuses on elucidating cellular (sub-) structures, it is often advisable to analyze fixed specimens. As the dynamics of cells and their compartments can blur their structural features in live cell imaging applications, eliminating this movement allows for higher image contrast. This is especially important to ensure high localization precision in superresolution SMLM techniques. In a typical chemical fixation procedure, the sample is immersed in a solution of a fixative, such as formaldehyde. When this chemical compound is diffusing into the tissue, it readily reacts with various functional groups of biological macromolecules, effectively cross-linking them. This serves to stabilize the tissue morphology and prevents proteolytic enzymes from degrading the sample. The type of fixative, its concentration and the duration of the procedure play a decisive part to preserve the cell structures as lifelike as possible.

Fluorescent proteins are often used as markers in biological samples and they are targeted by the fixative as well. Consequently, this can result in lower quantities of functional FPs and thus diminished fluorescence, which must be factored into the choice of fixation parameters.

2.5.4 (Cryo-)section

When the target structures are to be stained by other measures, they can be physically sectioned into thin slices by a microtome to provide better access to the cellular structures and further increase the contrast. In simple terms, the specimen is fixed on a sample holder and moved over a knife to cut away thin sections. The thickness is adjusted by the lateral movement of the sample holder with respect to the knife with a high-precision advancement mechanism. To allow for the thinnest sections, the sample can be embedded into a resin block to protect its integrity while cutting. Another method, called cryosection, hardens the sample by freezing it prior to cutting. For this purpose, the sample must be infiltrated with high concentrations of sucrose to prevent the tissue-damaging formation of ice crystals. By freezing and cutting in a cryo-ultramicrotome, extremely thin sections of 100 nm can be achieved, which are afterward thawed and transferred to standard coverslips.

2.5.5 Immunolabeling

In contrast to fluorescence markers like FPs that are endogenously expressed with the target protein, brighter and more stable organic dye markers can be introduced exogenously via antibodies. Biological macromolecules either naturally present certain recognition structures (epitopes) on their surface or they can be added by recombinant DNA techniques. As antibodies are highly specific for a certain epitope, they can be engineered to uniquely bind only to the target structure with high affinity. Since producing fluorescence-tagged antibodies for every conceivable epitope would be unreasonable, a two-step approach is commonly used. For this, a specific primary antibody binds to the epitope, while a secondary antibody carries the fluorescence tag and targets the primary antibody. As secondary antibodies can target different domains of the primary antibody, this also leads to a high fluorescence signal. Moreover, commercially available secondary antibodies are engineered to target a wide variety of primary antibodies, allowing greater flexibility.

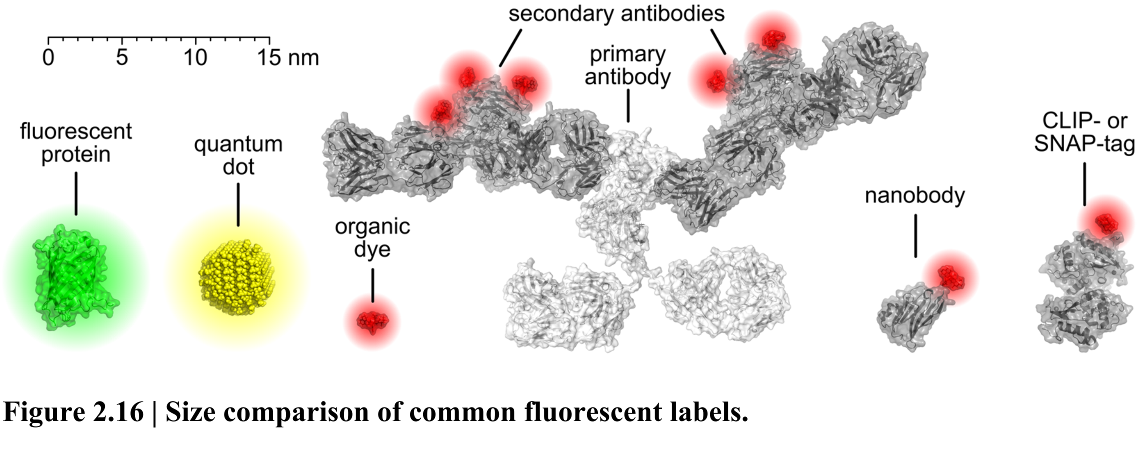

Figure 2.16 | Size comparison of common fluorescent labels.

This labeling method is largely dependent on the affinity and specificity of the employed antibodies, while its biggest advantage for imaging applications is the diversity of possible labels (metal nanoparticles, organic fluorophores) and the control of the labeling density. In particular for superresolution techniques like dSTORM, this enables using state-of-the-art organic dyes with favorable photophysical characteristics. However, secondary labeling also introduces some problems: as the antibodies are about 10 nm in size, this might introduce distances up to 20 nm between fluorescence label and target structure, thus limiting the achievable resolution (see Figure 2.16 for a size comparison of commonly used fluorescent probes). While the multiple labeling of one epitope might be advantageous for the improved signal-to-noise ratio, excessive clustering can negatively influence spatial or temporal separation of single emitters in SMLM techniques and therefore necessitates more control of the labeling density.

2.5.6 Pull-Down Assays and Co-Immunoprecipitation (Co-IP)

Pull-down assays serve as a biochemical tool to identify protein-protein interactions in vitro (Figure 2.17a). As a general principle, target proteins are immobilized on a solid substrate, such as small beads of various material compositions. In a next step, they are added to a solution of putative interaction partners. The physical interaction of the target proteins with other proteins in solution effectively immobilizes the latter on the solid support, “pulling” them out of solution; hence the name for the assay. After washing steps and elution from the solid substrate, the interaction partners can then be identified by molecular biology or biochemical methods.

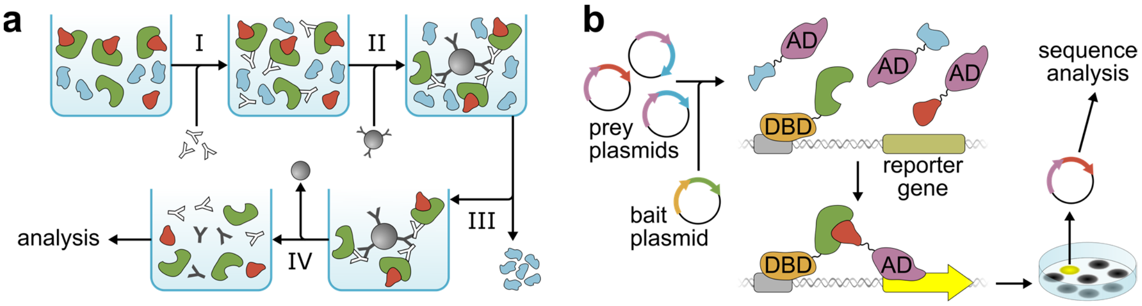

Figure 2.17 | In vitro interaction assays. (a) Pull-down assay. To find interaction partners (red) of a known biomolecule (green), the latter is targeted (I) with a specific antibody (white). A secondary, immobilized antibody (gray) is added (II) targeting the primary antibody. Washing (II) disposes all other components (blue) not bound to the solid support. After removal of the solid support (IV), the solution contains only the interaction partners that can now be analyzed. **(b)** Yeast-2-hybrid assay. A bait plasmid includes the genetic sequence of one interaction partner (green) fused to a DNA-binding domain sequence (DBD, orange), while one of several prey plasmids codes for a putative interaction partner (red, blue) fused to an activating domain (AD, violet). After expression of the proteins, only those yeast cells with interacting proteins (red and green) have both DBD and AD to activate a reporter gene. Corresponding yeast cell colonies can now be subjected to sequence analysis to determine the interacting partner.

One widely used strategy to immobilize the target protein requires its fusion to the enzyme glutathione S-transferase (GST). This protein has a very strong binding affinity to glutathione (GSH), thus the coating of a solid support with this chemical compound will reliably immobilize GST and any protein fused to it.

Co-immunoprecipitation (Co-IP) is a common pull-down assay using immobilized antibodies to specifically bind a target protein. As other proteins or ligands can interact with the target protein in solution, they are both precipitated by the antibody from the solution. This technique has the advantage that it requires no prior modification of the interacting proteins, thus allowing for their analysis in their native state.

Since these assays remove the proteins from their physiological environment, it is by no means certain that the proteins would show the same behavior in vivo. Transient interactions or those with low affinities may be lost during the washing procedure (leading to false negatives), as it introduces non-physiological conditions that might influence protein affinities. Non-specific binding of antibodies or their contamination in Co-IP experiments also present a common problem that can cause false positives.

Therefore, the results obtained by these methods must be verified with other interaction assays like yeast-two-hybrid assays or by spectromicroscopy, for example, with FRET experiments. However, they are particularly interesting for screening experiments, as they can also check for protein-protein interactions in complex mixtures or even entire cell lysates.

2.5.7 Yeast Interaction Studies

Since the development of so-called yeast two-hybrid systems in the late 1980s [99], they have become an invaluable tool to detect protein-protein interactions in vivo (Figure 2.17b). Originally, this method made use of yeast's transcription factor (TF) GAL4 that consists of two separable domains, a DNA-binding domain (DBD) and an activating domain (AD). Only the complementation of both domains results in a functional transcription factor that triggers enzyme production to metabolize galactose. By fusing each GAL4 domain to a different target protein, the physical interaction of the latter will also reconstitute the transcriptional factor's function. Therefore, only a successful interaction between the target proteins allows yeast to grow on galactose-rich media, which becomes evident from the size of corresponding yeast colonies.

The method was quickly adopted and developed further, using other transcription factors, interaction readouts or different host organisms. Universally, the protein fused to the DBD is referred to as “bait,” while the protein fused to the AD is called “prey”. By introducing a third protein that must act as a bridge between bait and prey to enable their interaction, so-called yeast-three-hybrid assays [100] make it possible to investigate ternary protein complexes.

Yeast two-hybrid assays are a very cost-effective technique, as target proteins are introduced into the yeast cells via plasmids with relative ease. This also made them popular for interaction screenings, for example, by using one known protein of interest as bait and testing it against whole libraries of prey proteins. The plasmids of yeast cells with a positive readout can then be sequenced to identify the interacting prey proteins.

Despite these advantages, yeast-two-hybrid assays are also associated with several methodological problems. Although the interactions take place under in vivo conditions, yeast might introduce posttranslational modifications that would not happen in the proteins’ original host organism. Furthermore, as the method relies on transcription factors, the interactions must take place in the nucleus, thus presenting a very different environment for cytosolic or membrane proteins. These factors regularly lead to both false positives and false negatives, which necessitates the verification of all results with other biochemical or spectroscopic techniques. Nevertheless, yeast-two-hybrid assays offer an important and straightforward first step in the analysis of most protein-protein interactions.

3 Application of Spectromicroscopy to Selected Scientific Projects

Throughout this thesis, the work on projects from different scientific fields mainly relied on various techniques of spectromicroscopy. The primary focus of each project rested on the successful answering of the respective scientific questions. The successful application of spectromicoscopy thus constitutes the central part of this scientific work, utilizing the capabilities of the custom-built research microscope. Moreover, the thematic range of the different projects also offered the opportunity to assemble and evaluate a set of methods that have proved particularly important across the included research areas. The following subchapters will concentrate on techniques and results, but also give a short overview of the experiment in the context of the respective field of study.

As individual techniques are becoming more and more specialized, interdisciplinarity and a high level of expertise in the respective fields (for example, microbiology, genetics, spectroscopy, sample preparation) are crucial for new insights. Cooperation and the coordination of joint research efforts are highly beneficial to answer even complex scientific questions, using novel approaches that go beyond the established framework of methods in the individual specialized fields. Consistent with this strategy, my thesis work mainly concerns the development, refinement and application of spectromicroscopy methods and related data analysis. The presented studies serve to validate the microscopy methods implemented in the course of this thesis. In addition, they underline the topicality of these techniques in current research. While the individual publications are briefly described in the corresponding chapters, they mainly focus on the application and analysis of spectroscopic techniques. Further details on the scientific background and discussions are provided by the full publications cited here.

The main contributions of my interdisciplinary cooperation partners and co-workers for the individual projects will be presented in the following subchapter overviews.

Chapter 3.1 is based on:

Sheerin, D. J.*, Menon, C.*, **zur Oven-Krockhaus, S.***, Enderle, B., Zhu, L., Johnen, P., Schleifenbaum, F., Stierhof, Y. D., Huq, E., and Hiltbrunner, A., "*Light-Activated Phytochrome A and B Interact with Members of the SPA Family to Promote Photomorphogenesis in Arabidopsis by Reorganizing the COP1/SPA Complex*," The Plant Cell, vol. 27, no. 1, pp. 189-201, 2015.

Here, the confocal technique FLIM-FRET will be applied to analyze interactions of labeled biomolecules. In this case, it was used to examine the reorganization of a certain effector complex involved in the plant developmental program. In vivo FLIM-FRET analyses were key to establishing a model for the molecular mechanism that triggers the photoreceptor-mediated change in that developmental process. This project was done in cooperation with the group of Andreas Hiltbrunner (Department of Molecular Plant Physiology, University of Freiburg). The main microbiological work, including sample preparation as well as confocal colocalization studies and the luciferase assay, was performed by Chiara Menon (Center for Plant Molecular Biology (ZMBP), University of Tübingen), yeast interaction assays and pull-down assays were performed by David Sheerin (Department of Molecular Plant Physiology, University of Freiburg).

Chapter 3.2 is based on

Weidler, G., **zur Oven-Krockhaus, S.**, Heunemann, M., Orth, C., Schleifenbaum, F., Harter, K., Hoecker, U., and Batschauer, A., "*Degradation of Arabidopsis CRY2 is regulated by SPA proteins and phytochrome A*," The Plant Cell, vol. 24, no. 6, pp. 2610-23, 2012,

and briefly discusses a related interaction study that further underlines the utility of this method. Here, FRET-FLIM confirmed that a physical interaction of effector proteins with blue light photoreceptors occurs within cell nuclei of living plants, which is involved in their switch from the vegetative to reproductive phase. In this cooperation with the group of Alfred Batschauer (Department of Plant Physiology, University of Marburg), the main microbiological work was done by Guido Weidler (Department of Plant Physiology, University of Marburg) and the transient transformation of tobacco plants performed by Michael Heunemann (ZMBP, University of Tübingen).

Chapter 3.3 is based on:

Nolte, A., Braun, T., **zur Oven-Krockhaus, S.**, Munz, A., Vogel, U., Schlensak, C., Wendel, H., and Walker, T., "*Stented Vessels: A Challenge for Histological Preparation and Microscopy*," Journal of Interdisciplinary Histopathology, vol. 1, pp. 104-112, 2013.

Here, a spectromicroscopy technique based on the evaluation of FLT curves (FIDSAM), developed by Frank Schleifenbaum (ZMBP / Institute for Physical and Theoretical Chemistry (IPTC), University of Tübingen) was adapted and used to achieve contrast enhancement in arterial histopathological sections, with the objective to better monitor the diffusion of anti-inflammatory drugs in stressed tissue. In cooperation with the group of Hans Wendel, Andrea Nolte was the principal investigator, overseeing and performing histopathological imaging and analyses, while Theresa Braun (all Department of Thoracic, Cardiac and Vascular Surgery, Tübingen University Hospital) performed the sectioning, grinding and polishing of the samples that were also used for the FIDSAM analysis.

Chapter 3.4 is based on

Peter, S.*, **zur Oven-Krockhaus, S.***, Veerabagu, M., Rodado, V., Berendzen, K. W., Meixner, A. J., Harter, K., and Schleifenbaum, F., "*Chimeric Autofluorescent Proteins as Photophysical Model System for Multicolor Bimolecular Fluorescence Complementation*," The Journal of Physical Chemistry B, vol. 121, no. 11, pp. 2407-2419, 2017,

and deals with analysis methods that rely on the ability to perform single-molecule spectroscopy, demonstrated by the photophysical characterization of biologically relevant probes for BiFC. In-depth analyses of their spectral characteristics largely relied on single molecule analyses and revealed photophysical properties that were evaluated for their effective use in biological assays in a cooperation project with Klaus Harter (ZMBP, University of Tübingen). Here, the spectromicroscopy work and analysis were shared with Sébastien Peter (ZMBP / IPTC, University of Tübingen) who additionally generated and purified all chimeric FPs. Manikandan Veerabagu, Virtudes Mira Rodado and Kenneth W. Berendzen (all ZMBP, University of Tübingen) provided samples for the in vivo validation.

Chapter 3.5 comprises the implementation of single-molecule localization superresolution techniques, first using dSTORM for fixed biological test samples (chapter 3.5.1) that were provided by York Stierhof (ZMBP, University of Tübingen). The general applicability was then demonstrated on a current biological research question, clarifying the structure of protein complexes in plant cell nuclei by applying the related superresolution technique SOFI in chapter 3.5.2 that is based on:

Speth, C., Szabo, E. X., Martinho, C., Collani, S., **zur Oven-Krockhaus, S.**, Richter, Droste-Borel, I., Macek, B., Stierhof, Y. D., Schmid, M., Liu, C., and Laubinger, S., "*Arabidopsis RNA processing factor SERRATE regulates the transcription of intronless genes*," eLife, vol. 7, p. e37078, 2018.

This cooperative project with the group of Sascha Laubinger (ZMBP, University of Tübingen) mainly focused on plant genetics with biochemical and microbiological methods that were primarily performed by Corinna Speth (ZMBP, University of Tübingen). For the SOFI visualization of the protein complexes, plant samples were cryo-sectioned and immunolabeled by York Stierhof, while Sandra Richter (ZMBP, University of Tübingen) acquired images on a Zeiss commercial microscope with the Airyscan extension. Subsequently (chapter 3.5.3), sptPALM, a related technique using single-molecule localization in live cells, is validated by comparing own results with published data. Nina Glöckner (ZMBP, University of Tübingen) cultivated the plant seedlings that were used for this analysis.

The project described in chapter 3.6 involves a FRET-based sensor developed by Frank Schleifenbaum (ZMBP / IPTC, University of Tübingen), which was designed to measure nanoscopic flow with high resolution. Due to its interdisciplinary approach, parts of this project were popular topics for student internships and theses. Accordingly, it had many contributors, starting with the work of Daniel Basler, who synthesized the original sensor and produced the measurements for the original publication. Richard Martin Kemmler immobilized the sensor on metal and plastic supports and explored other working fluids in flow cells, while Tim Rammler further investigated viable polymer supports and tested different sensor geometries (all abovementioned persons: IPTC, University of Tübingen). Alexander Stuhl (Applied Chemistry, Reutlingen University) currently works on a mathematical model to simulate the sensor response. As the work on this project is not yet concluded, the chapter should be taken as a snapshot of the current state of research. In the context of this thesis, it serves as an example for multidisciplinary methodological research, ranging across molecular biology, chemistry and molecular engineering. At the same time, it also shows that such an approach greatly benefits from access to multiple spectromicroscopy techniques to characterize the underlying mechanics and properties of the nanoscopic sensor.

The description all individual projects will focus on their employed methods and their applicability to other scientific fields. Their benefits and possible challenges, as well as their technical prerequisites, serve as important points for the design of the interdisciplinary research microscope that is described in chapter 4.

3.1 In vivo FLIM-FRET Interaction Analysis of a Ternary Protein Complex Involved in Light-Mediated Plant Development

The investigation of protein-protein interactions has long been the domain of biochemical and molecular biological methods. However, they have always been subject to numerous uncertainties. It cannot be ruled out that dynamic and most importantly intact, living systems operate quite differently than what the results of ex vivo techniques like co-immunoprecipitation would suggest. Moreover, assays done in a different host organism such as yeast-2-hybrid assays might raise concerns regarding the transferability of results. If possible, live cell imaging techniques would be clearly preferable to elucidate the actual cellular processes. Fortunately, protein-protein interactions have also become an integral part of modern microscopy, not least due to its growing synergy with physicochemical methods. A widespread technique to uncover in vivo protein-protein interactions combines the high-resolution imaging capabilities of a confocal microscope with the analysis of FRET. Co-expression of the putative interaction partners with biological markers like GFP further minimizes interference with the natural cellular processes.

While microscopy provides the necessary spatial resolution to address the appropriate cell (sub-) compartments or tissues up to the diffraction limit, FRET assays can uncover protein-protein interactions on much smaller length scales of several nanometers. Moreover, they are suitable for time-dependent or dynamic studies. However, intensity-based FRET experiments suffer from undesirable dependencies on laser excitation power, detection sensitivity, chromophore concentration and more. The combination of FLT imaging microscopy with FRET (FLIM-FRET) is largely free from the aforementioned issues and therefore the method of choice for in vivo interaction studies. The most common type of a FLIM extension for a confocal microscope setup requires a pulsed laser source, a TCSPC unit, a suitable detector and the analysis software. This financial investment pays off quickly, as the increasing number of publications with FLIM-FRET shows. However, this does not detract from the success of biochemical in vitro methods: their simplicity, speed and ability to screen for many interactions simultaneously makes them effective tools. In fact, both methods should be understood as complementary to corroborate each other's results. In this regard, this project [101] can serve as a good example for interdisciplinary research and will be briefly outlined in the following.

The main objective was the investigation of light-dependent signaling pathways in plants. While they possess very different classes of photoreceptors, covering almost the entire visible spectrum, this study focused on the class of phytochromes. Apart from photosynthesis, plants also use light conditions as an information signal, for example, to adapt to their environment, to control their circadian rhythm or their life cycle according to the seasons. Following germination, the main developmental program in the dark is skotomorphogenesis. At this stage, seedlings mainly grow opposite the gravity vector to reach the top of the soil. In the light, the program changes to photomorphogenesis, which reduces the longitudinal growth and triggers leaf development and chlorophyll production for photosynthesis. The role of phytochromes on the switch between these two developmental programs was of particular interest. In dark-grown seedlings, photomorphogenic growth factors are constantly degraded, actuated by a protein complex consisting of CONSTITUTIVELY PHOTOMORPHOGENIC1 (COP1) and SUPPRESSOR OF *phyA-105* (SPA). Therefore, this complex effectively maintains skotomorphogenesis. In the light, the activity of the COP1/SPA complex diminishes, which accumulates the aforementioned growth factors, in turn initiating photomorphogenesis. Previous studies showed that phytochrome A (phyA) and phytochrome B (phyB) are the main photoreceptors mediating this light-dependent response, yet the exact molecular mechanism remained unclear at that point. As signal transduction pathways are often intricately interwoven, the scientific approach relied on multiple methods. The working hypothesis was that a direct interaction of phyA with the COP1/SPA complex, either competing with the interaction partners or otherwise reorganizing the complex, inhibits its activity. Therefore, biochemical analyses like yeast-two-hybrid assays focused on the screening of interaction partners for the putatively involved proteins. Members of the SPA family were the most promising candidates, in particular SPA1 showed a strong affinity to phyA, which was also confirmed by in vivo Co-IP experiments. Additional assays also examined protein domains for binding or localization sites. As these and other findings are essential for the biological context, they are presented in detail in the attached publication [101], however, they are beyond the scope of this chapter.

Focusing on the FLIM-FRET analyses, all the above suggested interactions were also analyzed in vivo in transiently transfected tobacco leaves. Due to its multiexponential fluorescence decay properties, the employed donor cyan fluorescent protein (CFP) is technically not well suited for FLT analyses. In case of FRET to the acceptor YFP, this would result in additional rate constants that could further complicate data analysis. However, as this project built on previous studies and already established libraries of protein constructs, CFP was nevertheless used throughout this project. The necessary increase of free fitting parameters makes it mathematically more difficult to distinguish actual interaction events from random data fluctuations. This could result in false negatives for fast transient interactions or unfavorably attached fluorophores. As already explained in chapter 2.5.1, this must always be considered for negative FLIM-FRET results and must be checked with alternative methods in case of doubt. The protein complexes investigated in this project were largely unaffected by the challenges mentioned above, so basic test statistics allowed clear conclusions for the analyzed protein-protein interactions. Therefore, the fit curves for “donor only” and “donor with acceptor” experiments were restricted to two and three exponents, respectively. After the calculation of the intensity-weighted average FLTs, they were evaluated with two-sample *t*-tests assuming unequal variances, which reliably produced robust results.

First, (co-) localization experiments determined the main cell compartments where the interactions would take place. It could be shown that all complex compounds localize to subcompartments of the cell nucleus, so-called nuclear bodies (NBs). The precise role of these structural elements is still unclear, but their formation often coincides with physiological activity or the degradation of light signaling components. It therefore stands to reason that they are crucial for signal transduction. Phytochromes must be in their light-induced, active form (Pfr) to translocate to the nucleus, while SPA and COP1 also form NBs in the dark.

As phyA nuclear import in the transfected organism *N. benthamiana* was rather inefficient, a nuclear localization signal (NLS) was attached to the fusion constructs for sufficiently high phyA levels in leaf epidermal cell nuclei. After exposure to light, photoactivated phyA colocalized and interacted with SPA1 in NBs, as shown in Figure 3.1a. Here, the donor FLT of phyA-NLS-CFP served as the negative control, while a fused donor-acceptor construct (CFP-YFP) provided a positive control to assess the dynamic range of expectable results. Co-expression of protein fusion constructs phyA-NLS-CFP and YFP-SPA1 resulted in a significantly reduced donor FLT. This confirmed the phyA/SPA1 interaction and generally proved the validity of the FLIM-FRET approach for the planned in vivo interaction analyses. The interaction of phyA/COP1 was investigated in a similar fashion (see Figure 3.1b). Co-expressed phyA-NLS-CFP and YFP-COP1 again visibly colocalized in NBs. Accordingly, the significant FLT decrease of the donor (CFP) verified this interaction, too.

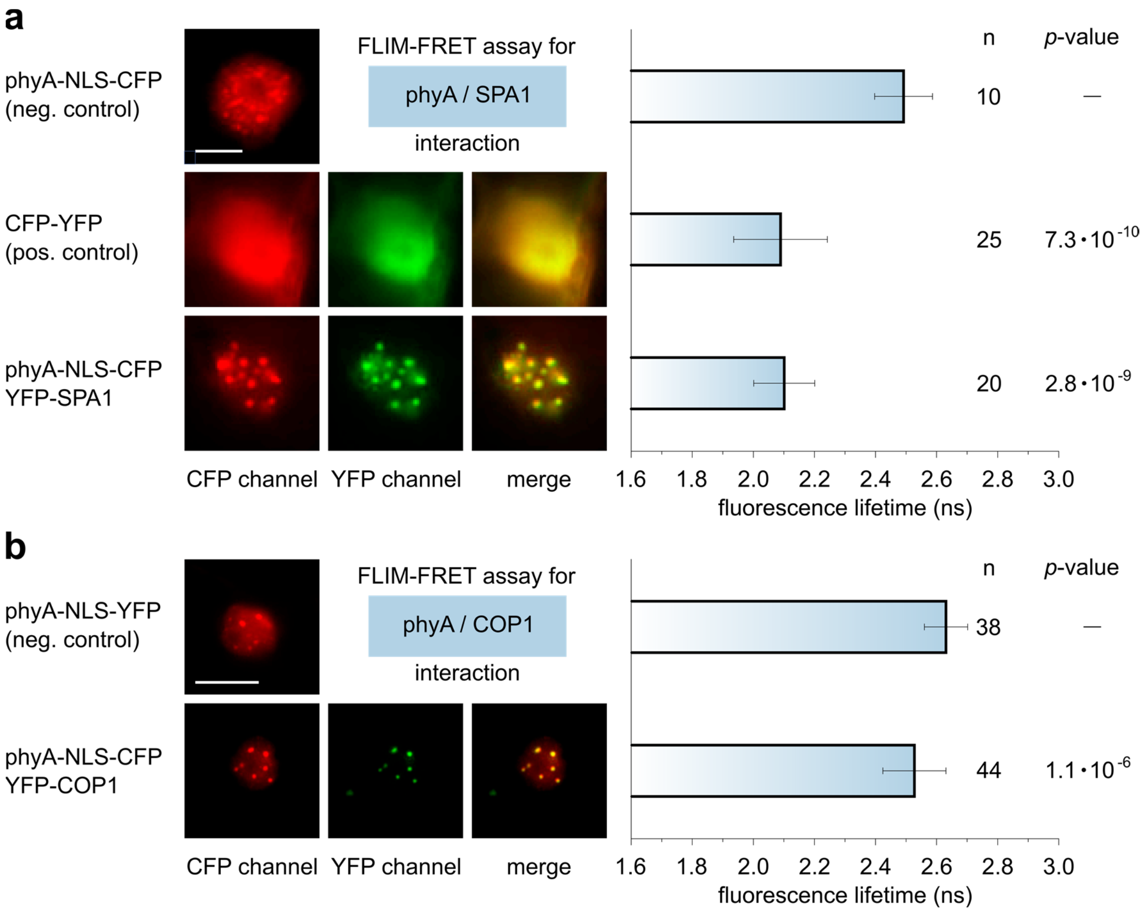

Figure 3.1 | FLIM-FRET interaction analysis of phyA with SPA1 and COP1. (a) Left: subcellular localization of phyA-NLS-CFP (negative control, upper row), a direct fluorophore fusion of CFP and YFP (positive control, middle row) and co-expressed phyA-NLS-CFP and YFP-SPA1 (lower row), all in transiently transformed *N. benthamiana* plants. Right: corresponding mean donor FLTs of n measurements. Error bars represent one standard deviation of uncertainty, p-values indicate *t*-test analysis results for statistically significant differences. **(b)** Analog interaction assay for the co-expression of phyA-NLS-CFP and YFP-COP1. Scale bars, 10 µm.

As the COP1/SPA1 interaction was already well documented, these findings suggested that active phyA interacts with the COP1-SPA1 complex in the form of an at least ternary complex, which was also backed up by yeast-3-hybrid experiments. To evaluate the initial hypothesis, an in planta experiment had to be designed to show how phyA influences the COP1-SPA1 complex. While it seemed compelling to set up a triple-FRET assay, the inclusion of CFP with multiexponential fluorescence decay statistics would introduce too much uncertainty into the necessary calculations. Due to the extensive prior investigations, a straightforward and more robust alternative presented itself: as phyA is the key component that enters the complex in a light-dependent fashion, a mere change of the light conditions should show if phyA accumulating in the nucleus has any effect on the distance between a FRET-pair attached to COP1 and SPA1 (see scheme in Figure 3.2a, bottom).

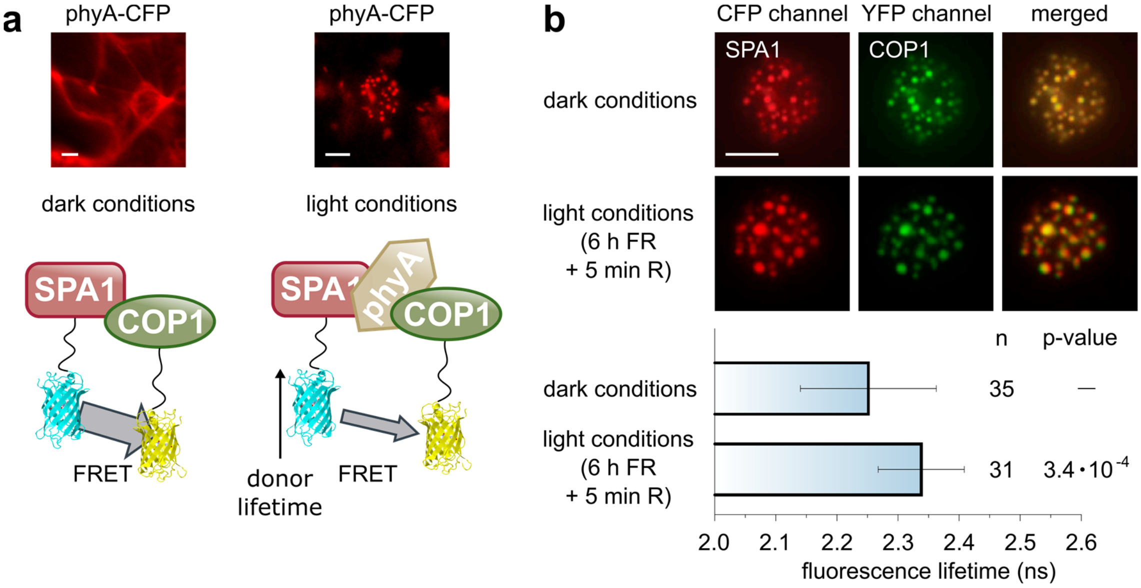

Figure 3.2 | FLIM-FRET analysis of the COP1-SPA1 complex reorganization by phyA. (a) Top: light-dependent nuclear transport of phyA-CFP into NBs of transiently transformed *N. benthamiana* plants. Bottom: schematic setup of the experiment. **(b)** Top: subcellular localization of CFP-SPA1 and YFP-COP1 in transiently transformed *N. benthamiana* plants under dark and light (6 h far-red (FR) + 5 min red (R)) conditions. Bottom: corresponding mean donor FLTs of n measurements. Error bars represent one standard deviation of uncertainty, p-values indicate *t*-test analysis results for statistically significant differences. In these experiments, phyA was co-transformed in a firefly luciferase fusion to confirm its expression in a separate assay. Scale bars, 10 µm.

Without a nuclear localization sequence, phyA relies on the host plant's transport machinery for nuclear transport, which is triggered by exposure to six hours of far red light (FR, $\lambda = 720$ nm), followed by activation into the active Pfr form with a five-minute pulse of red light (R, $\lambda = 670$ nm). As repeatedly verified and shown in Figure 3.2a (top), dark-grown plants accumulate phyA only in the cytosol, while the abovementioned light conditions reliably transport phyA into NBs. Moreover, the interaction of COP1 and SPA1 is light-independent (not shown here). Therefore, any differences in the COP1-SPA1 distance under different light conditions can be assigned to phyA's presence with high probability. With all other experimental conditions held constant, the donor indeed showed a significantly lower FLT under dark conditions than under light conditions (Figure 3.2b).

To ascertain that phyA was indeed co-expressed, it was fused to the firefly luciferase enzyme to show its presence by a separate luciferase assay. Conveniently, this does not introduce potentially interfering fluorophores into the system. The over-expression of all target proteins also largely ruled out that yet undiscovered other components would be able to mimic the significant alteration.

The initial hypothesis can therefore be supported with high confidence: under in vivo conditions, the light-dependent localization of phyA to nuclear bodies results in its direct interaction with the COP1-SPA1 complex, leading to the latter's separation or conformational restructuring thus affecting its ability to degrade photomorphogenic growth factors. Supported by the biochemical and microbiological assays in this project, the FLIM-FRET analyses serve to strongly emphasize this proposed model. More importantly, this in planta technique demonstrated these findings under physiological conditions.

In the presented project, one crucial aspect of experimental conditions must still be mentioned: the influence of irradiation caused by the imaging system itself. The work on living systems that react to minute changes in their light environment can thus be extremely demanding, especially if the objects of study are sensitive photoreceptors like phyA and phyB. Particularly for plants kept in the dark for several days, it is part of their survival strategy to quickly respond to light stimuli. For example, even the briefest exposure to room light (or the search for suitable cell structures in the microscope under white light) can trigger the accumulation of phyA in cell nuclei, which makes its localization under truly dark conditions challenging. Even sharply defined illumination wavelengths far off the photoreceptors' absorption bands might have physiological effects under prolonged exposure. This kind of possible external influence by the irradiation during imaging must always be kept in mind and checked by appropriate control experiments. In this project, a two-pronged approach was pursued. On one hand, each plant sample was imaged instantly after removing it from the specified light conditions, replacing them continuously to limit each sample's imaging exposure. On the other hand, control experiments with chemically fixed samples were carried out, thus negating any dynamic biological reactions to light. When they resulted in the same outcome as the live cell analyses, this pointed to the negligible influence of imaging irradiation, thereby validating the in vivo experiments. Furthermore, it was discovered that even transiently transformed tobacco leaves could be chemically fixed and imaged under the right conditions. Assuming that the findings for this plant host system are transferable to *A. thaliana*, this proved to be extremely time-effective, as new experiments in transiently transformed systems could be set up much quicker than the cloning and selection of stable lines. It could also apply to experiments outside this project, in which external influences on the biological system or excessive movement of cell compartments have to be suppressed. This serves as an example for the development or adaptation of techniques, when the experimental setup must comply with the sample's necessities.

Correspondingly, this also refers to the abovementioned choice of fluorophore (CFP), which does not have optimal properties for FLIM. However, since it had to be retained to be consistent with previous experiments, some flexibility was required on the methodological side. The evaluation of FLTs thus had to be more prudent, but this never influenced the consistently positive results. Nevertheless, as the choice of fluorophores can have a large impact on FLIM experiments, they will be briefly discussed at this point. As indicated above, several types of fluorescent probes can be utilized in different experiments. The development of ever better and more specialized FPs for protein fusions offered an improved adaptation to the demands of microscopy analyses, but also led to a high variability in fluorophore sets employed by different research groups. It may not always be possible to use fluorophore combinations deemed most suitable from a photophysical point of view. For example, the difficulty of cloning new fluorophore fusions highly depends on the target molecule. For an interdisciplinary research microscope, this calls for high flexibility in excitation wavelengths and the filtering and detection of multiple emission wavelengths. To provide meaningful results with less suited fluorophores, it also requires an advanced understanding of the underlying photophysical processes. FLIM-FRET experiments narrow the (perfect) fluorophore choice to monomeric, bright, quickly maturing donor/acceptor pairs with excellent spectral overlap, low cross-excitation, well separated emission signals and monoexponential donor fluorescence decay statistics. In case of FPs, the development and optimization of their biological and spectroscopic properties across the spectral range seem largely complete. However, the adoption of a standard system that can be extensively used for various experimental methods in fluorescence microscopy, was still missing. The abundance of experimental data collected in multiple collaborations between the plant physiology and physical chemistry department subsequently led to the design of such a system [90], incorporating the specialized knowledge of the biological and spectroscopic requirements. The novel vector set uses a recombination-based 2in1 cloning system for an improved and equalized co-expression of proteins and makes use of carefully selected state-of-the-art fluorescent proteins. This not only enables specialized FLIM-FRET experiments, but also improves intensity-based FRET and (co-) localization experiments as well as BiFC assays.

Furthermore, this illustrates how a strong interdisciplinary cooperation can pool the expertise from each scientific field to create new innovative methods that benefit a wider field of research.

3.2 In vivo FLIM-FRET Interaction Analysis of a Family of Developmental Signaling Components in Plants

Similar to the previous chapter, this project [102] deals with the transition of plant developmental programs, in this case the switch from the vegetative to the reproductive phase that includes flowering. Cryptochromes act as UV-A / blue light receptors and play a role in many plant signaling pathways, but cryptochrome 2 (CRY2) in particular is accredited to induce flowering under long-day conditions. Its fundamental role in these regulatory processes therefore makes it and its interactions with other signaling components an interesting research target.

Following blue light absorption by its photopigments pterin and flavin, CRY2 quickly undergoes phosphorylation, which enhances its activity but also targets it for degradation. Such feedback loops are typical and necessary for highly adaptive networks: to react quickly, interactors must have short effector spans. They are constantly expressed and degraded to adjust protein levels. Prominent examples for this mechanism are the circadian clock or the drastic metabolic switch from day to night. For CRY2, downregulation of gene expression under blue light exposure was largely ruled out, meaning that a drop in CRY2 levels is mainly caused by proteolytic degradation at the posttranslational level. The COP1/SPA1 complex, a focal point of light-dependent signaling (also see chapter 3.1), was expected to be mainly responsible. Indeed, light-independent CRY2/COP1 interactions were already shown in yeast-two-hybrid experiments. Shortly prior to the study presented here, blue-light-dependent interactions between CRY2 and SPA proteins were demonstrated in yeast-two-hybrid and Co-IP assays. These findings suggested that SPA proteins may play an active role in degrading the activated CRY2. However, as all interaction experiments lacked in vivo data in a plant system, this picture was still incomplete. Being part of the same complex, it could not be excluded that COP1 may have acted as an adaptor protein, mediating a merely indirect interaction between CRY2 and SPA. Therefore, this project set out to demonstrate the SPA-dependent CRY2 degradation by light-dependent kinetic experiments with spa mutants and also to show the CRY2/SPA interaction for the first time in vivo with FLIM-FRET in plant cell nuclei.

In short, the kinetic studies measured the remaining CRY2 protein levels under light irradiation of different colors and intensities. If SPA had a direct effect on CRY2 degradation, then spa mutants lacking this protein should show higher CRY2 levels. A full description of this assay can be found in the accompanying publication [102]. Key conclusions from the analysis are: a) CRY2 degradation depends exclusively on blue light, which triggers the active form of CRY2; b) all *spa* mutants showed significantly higher CRY2 levels, underlining that SPA proteins impact CRY2 degradation under physiological conditions. The SPA proteins were further able to complement each other's function, indicating redundancies and mutual influences on their respective activities. Interestingly, also the photoreceptor phyA had a considerable effect on CRY2 levels under blue light with low fluence rates. This previously unreported finding suggested cross-talk between phytochromes and cryptochromes and stresses the interwoven function of photoreceptors in light-signaling, in particular as phyA enters the COP1/SPA1 complex under very different light conditions (also see chapter 3.1).

For the FLIM-FRET experiments, CRYPTOCHROME-INTERACTING BASIC-HELIXLOOP-HELIX PROTEIN1 (CIB1) is a known interactor for activated CRY2 and was therefore chosen as a positive control. GFP-SPA1 and GFP-SPA1/mCherry-NLS fusions served as negative controls. Putative interactions of CRY2 were tested with SPA1-4.

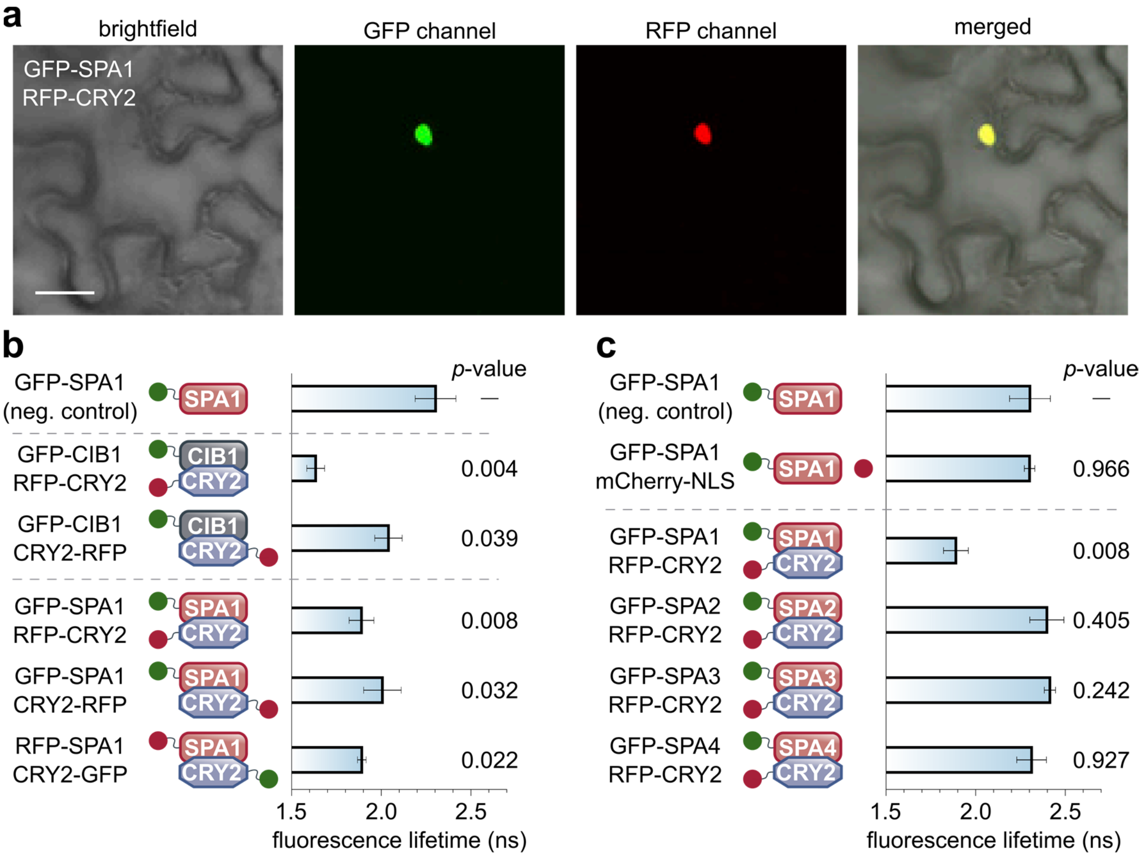

Figure 3.3 | FLIM-FRET analysis of CRY2 with SPA proteins and CIB1. (a) Subcellular localization of GFP-SPA1 and RFP-CRY2 in transiently transformed *N. benthamiana* plants. Scale bar, 10 µm. **(b)** FLIM-FRET interaction assays of CRY2 with CIB1 or SPA1. Left: for more clarity, schematic representations of the proteins accompany the interaction experiments. The positions of their fluorescent tags (GFP, green circles and RFP, red circles) show if they were fused to the N- (left) or C-terminus (right). Right: corresponding mean donor FLTs of three independent measurements. Error bars represent one standard deviation of uncertainty, p-values indicate *t*-test analysis results for statistically significant differences. **(c)** Analog interaction assay for the co-expression of CRY2 with SPA1-4. GFP-SPA1 was co-expressed with an mCherry-NLS fusion as an additional negative control.

The respective interaction partners were co-expressed in *N. benthamiana* leaves, confirmed by confocal microscopy (see Figure 3.3a for an example with GFP-SPA1 and RFP-CRY2). The negative control showed a FLT of 2.30 ns (Figure 3.3b, top), which did not change when it was co-expressed with mCherry-NLS (Figure 3.3c, top). The latter demonstrates that no unspecific interaction between the fluorophores took place, even when they localize to the same spatially constricted (sub-) compartment. Moreover, the positive control GFP-CIB1/RFP-CRY2 (Figure 3.3b) showed a strongly reduced donor FLT of 1.65 ns, resulting in a solid dynamic range for the subsequent experiments. Interestingly, fusing the RFP fluorophore to the C-terminal end of CRY2 resulted in a much higher FLT (2.05 ns). This still represented a significant reduction compared with the negative control, but it showed that the attachment points of the fluorophores can have a severe influence on measured FLTs. Without prior knowledge of the exact structural orientation of two interactors, it is therefore very difficult to quantify protein interaction strengths based solely on the FRET rates of the fluorescent probes. Confirming the proteins' close vicinity (implying their interaction) is, however, often sufficient to meet the objective of the study. GFP-SPA1/CRY2-RFP also showed a significant reduction in donor FLT, substantiating the initial claim of a direct CRY2/SPA1 interaction. This was further validated by the positive FRET signal when RFP was attached to the C-terminal end of CRY2 or if the fluorophores were swapped. These findings and a simple estimation of protein sizes and possible chromophore distances made it highly unlikely that the interaction is just mediated by COP1. Interactions of SPA2-4 with CRY2 could not be shown with this FLIM-FRET assay (see Figure 3.3c). Nevertheless, this could be explained with their lesser affinity to CRY2 in comparison to SPA1, which was already apparent in prior conducted in vitro interaction studies in this project [102].

In conclusion, there is strong evidence for a direct interaction of SPA1 with CRY2 in living plant nuclei, suggesting that at least a trimeric SPA1-CRY2-COP1 complex is needed for the efficient degradation of CRY2 under blue light conditions. It should be pointed out that the application of FLIM-FRET at the time was not widespread in plant sciences. The combination of classical microbiological and biochemical analysis techniques with this powerful in vivo method gave this project the edge to publish it in a high impact journal (The Plant Cell) in a very competitive field. Accordingly, the spectromicroscopy experiments presented in this and the previous chapter validate FLIM-FRET as an essential capability for straightforward interaction analyses in a physiological context.

The FRET-FLIM studies presented here have largely dealt with binary interaction assays. However, the technique is extremely versatile and can also be combined with other confocal methods, such as FCS, to Fluorescence Lifetime Correlation Microscopy. Here, information from the obtained fluorescence decay curves can be used to better separate the individual FCS channels. But FLIM can also be combined with quite different methods, such as anisotropy. With the latter technique, it is possible to measure molecular orientation, energy migration (homo-FRET), and rotational diffusion, which can all lead to the depolarization of the emitted fluorescence [103]. This is especially useful to analyze the structure of protein clusters, as the depolarization correlates with the number of nearby fluorophores. Additionally, FLIM can provide a second approach to analyze homo-FRET by evaluating the FLTs. Researches utilized this combination to capture 3-D cluster size images in cell membranes in which GFP was linked to a lipid raft marker [104]. This is just one example of the versatility of time-resolved methods. The next chapter will also demonstrate how TCSPC has contributed to the development of new methods beyond protein-protein interaction assays.

3.3 Application of FIDSAM to Histopathological Sections

Originally, the driving factor to conceptualize and develop the FIDSAM technique has been the wide-spread problem of imaging highly autofluorescent tissues or cell compartments in plant microscopy. Separating the signal of employed fluorescent probes from other, intrinsically fluorescent molecules in a sample can be an arduous task. This is particularly true if the desired fluorescence signal shares spectral and temporal characteristics with an underlying strong autofluourescence background. This applies not only to plant microscopy, but to all scientific areas using fluorescent microscopy.

In the study [105] described in this chapter, autofluorescence was a major obstacle for the analysis of animal histopathological sections that were prepared to study treatment options for atherosclerosis. The latter classifies a very common vascular disease characterized by the narrowing of arterial blood vessels, caused by a chronic inflammatory response in thickening artery walls. Advanced stages can lead to arterial blockages with lethal consequences like heart attacks or strokes and are among the most frequent causes of death in western, industrialized civilizations. A common treatment option for atherosclerosis is pushing a balloon catheter into the blocked passage, which is pumped up and then removed, leaving behind a widened vessel. A metal support tube mesh (stent) is pushed into the endangered arterial section to bolster the vessel against renarrowing. This is often done in one step with the stent already being wrapped around the balloon catheter. Despite this precaution, in one fifth of angioplasty patients the arteries renarrow over time. The exact reason for the arterial reaction after the stent implantation is still unclear. Possibly, the renewed inflammation is due to prior tissue damage or the irritation by the angioplasty itself. Therefore, implanted stents are often coated with chemical compounds to counter inflammation reactions or other undesired vascular responses. However, developing suitable pharmaceutics is largely hindered by the lack of techniques to monitor the drug distribution and their effect in the afflicted tissue with high resolution. The underlying problem is twofold. On one hand, the preparation of clean and intact histopathological sections for microscopic studies, particularly including metal stents, is highly challenging. On the other hand, due to the angioplasty procedure, the compressed and inflamed tissue shows a high degree of autofluorescence background in microscopy, which would be otherwise ideal to track fluorescently tagged compounds in the direct vicinity of the stents. Nolte et al. [105]

managed to drastically improve upon the preparation techniques. They also embedded surgically excised samples in a polymethyl methacrylate (PMMA) block instead of conventional embedding materials for histopathological sections. This proved necessary to limit the amount of photobleaching and deterioration of the fluorescence labels, as PMMA does not rely on ultraviolet light or high temperatures for polymerization. After sawing, grinding and polishing, the thin (< 30 µm) sections showed no scoring or folding artifacts and were therefore suitable for fluorescence imaging. The microscopy experiments were designed to answer the fundamental question if drug diffusion from the stents into the tissue can be visualized at all. A conceivable development for stent coatings are small (or short) interfering RNAs (siRNAs), which are used for short-term silencing of protein coding genes, for example, the ones responsible for inflammation. Furthermore, such RNA fragments can be tagged with biological markers like GFP. Consequently, the stents were coated with a GFP reporter gene to validate if the fluorescent tag would be visible in the histopathological sections despite a strong autofluorescence background. The negative control lacked the reporter gene, but was otherwise treated equally. All images were acquired under the same conditions and instrument settings.

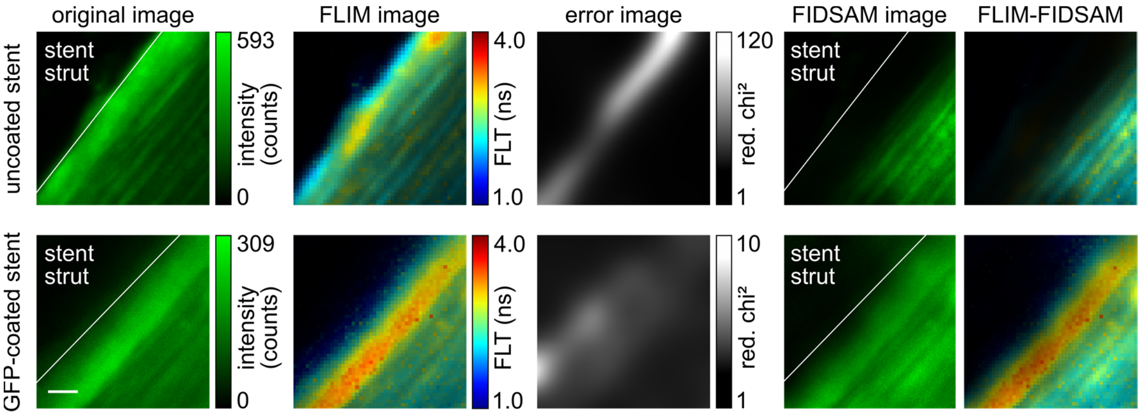

Figure 3.4 | Fluorescence intensity shape analysis microscopy (FIDSAM) applied to cross sections of stented coronary arteries. Upper row: uncoated stents (negative control). Lower row: stents coated with a GFP reporter gene. From left to right: original confocal image (with indicated stent strut position), FLIM image, error image (map of Gaussian blurred red. chi² values), resulting FIDSAM image (with stent strut position for comparison) and FLIM-FIDSAM image. Scale bar, 5 µm.

A first comparison of the original fluorescence images showed that negative control and sample were largely indistinguishable (Figure 3.4, first column). As mentioned before, the arterial tissue adjacent to the stents is compressed and damaged, resulting in a significant autofluorescence background. Although at first glance the FLIM images (Figure 3.4, second column) displayed differences in the distribution of FLTs, their range near the stents was very similar. This underlines the problem that autofluorescence and common fluorescent tags are not only spectrally similar, but often also show comparable FLTs. Neither the intensity nor the FLT distribution could hence be used as a basis for discriminating the GFP signal from the background.

FIDSAM was applied to both negative control and sample according to the workflow in chapter 2.2.2, with identical parameters. The underlying differences in the fluorescence decay curve shapes per pixel were now uncovered by their red. chi^2 values, that is, their error images (Figure 3.4, third column). The affected region of the uncoated stent was not only sharper defined, but the absolute error values were also much higher compared with the GFP-coated stent. Consequently, the differences between the FIDSAM images (Figure 3.4, fourth column) were significant: in case of the uncoated stent, the intensity directly adjacent to the stent was visibly subdued. This was also noticeable when comparing the FLIM and FLIM-FIDSAM images (Figure 3.4, second and last column). The FLIM image for the coated stent showed the expected FLT for GFP (around 3 ns) and the FIDSAM routine had negligible influence on that region. The effect on the negative control was quite different: although pixels this region featured different FLTs than the rest of the image, they were completely dark in the FLIM-FIDSAM image, indicating strong autofluorescence. This effect could also be observed for replicates of this experiment.

In summary, FIDSAM provided a crucial technique to visualize a fluorescence tag in a strong autofluorescence background. Above all, it could be demonstrated that, indeed, the fluorescent marker GFP and not autofluorescence was visible when using accordingly coated stents. This was a fundamental result for all experiments in that line of study, as the advantages of high-resolution fluorescence microscopy can now be utilized to analyze drug distribution into the stent-adjacent tissues. More precisely, this now allows to answer how far the coating diffuses into the tissue. Additionally, the effectiveness of the coating can also be assessed, as a reduced inflammatory response would also result in lower autofluorescence levels, which in turn would be visible with FIDSAM.

Previous experiments using FIDSAM demonstrated its value for plant microscopy. Applying the technique to histopathological sections of animal tissue now also showed its demand in other research areas. It further validates FIDSAM as a technique with practical, general usefulness across scientific disciplines which employ microscopy as an analysis tool. As the hardware requirements for FIDSAM are the same as for FLIM, this again (see chapters 3.1 and 3.2) underlines that time-resolved fluorescence measurements are highly beneficial for an interdisciplinary research microscope.

The analysis software is an integral part of FIDSAM, which has to be adaptable for different data formats or the implementation of new analysis parameters or routines. The chosen programming software was MATLAB (Mathworks, Natick, USA), a programming language oriented toward scientific applications, extensible with numerous research-specific toolbox packages. It can also interface with other programming languages and is supported by an active, helpful online community. Furthermore, it is easy to learn and use, widely spread in academia and already licensed to many universities. This ensures that analysis programs written for the research microscope are accessible to changing personnel and open to further additions and developments. Although slow in comparison with widespread programming languages like C/C++ or Javascript, the accessibility of MATLAB was the main reason to choose it as the main programming tool for data analyses. For this project, this approach also ensured that other data format inputs could be implemented easily and the FIDSAM data could quickly be cross-examined with analysis results of other spectroscopic methods.

The graphical user interface (GUI) of the original version (CILA 3.0, developed 2009 by Marcus Sackrow) served as a design template for an otherwise completely newly written program in MATLAB, which GUI is shown in Figure 3.5.

First priority was the processing of SymPhoTime files (PicoQuant, Berlin, Germany), the proprietary software for the TCSPC equipment used throughout this work. A demo data reader for SymPhoTime’s *.pt3 files (read_pt3.m, P. Kapusta [05/2007], rewritten by J. Robison [06/2012]), was adapted to accept multiple data formats. This allows for reading raw data files of the current SymPhoTime version (*.ptu) and different scan types (monoand bidirectional sample scanning as well as frame stacks that are produced by beam scanning systems, such as the Leica TCS SP8 FLIM extension). Pre-binned *.sdt data files, the output of the SPCImage software (Becker & Hickl, Berlin, Germany), can also be processed. Therefore, the rewritten FIDSAM software now covers the most common data formats of the major companies that specialize in time-resolved fluorescence measurements.

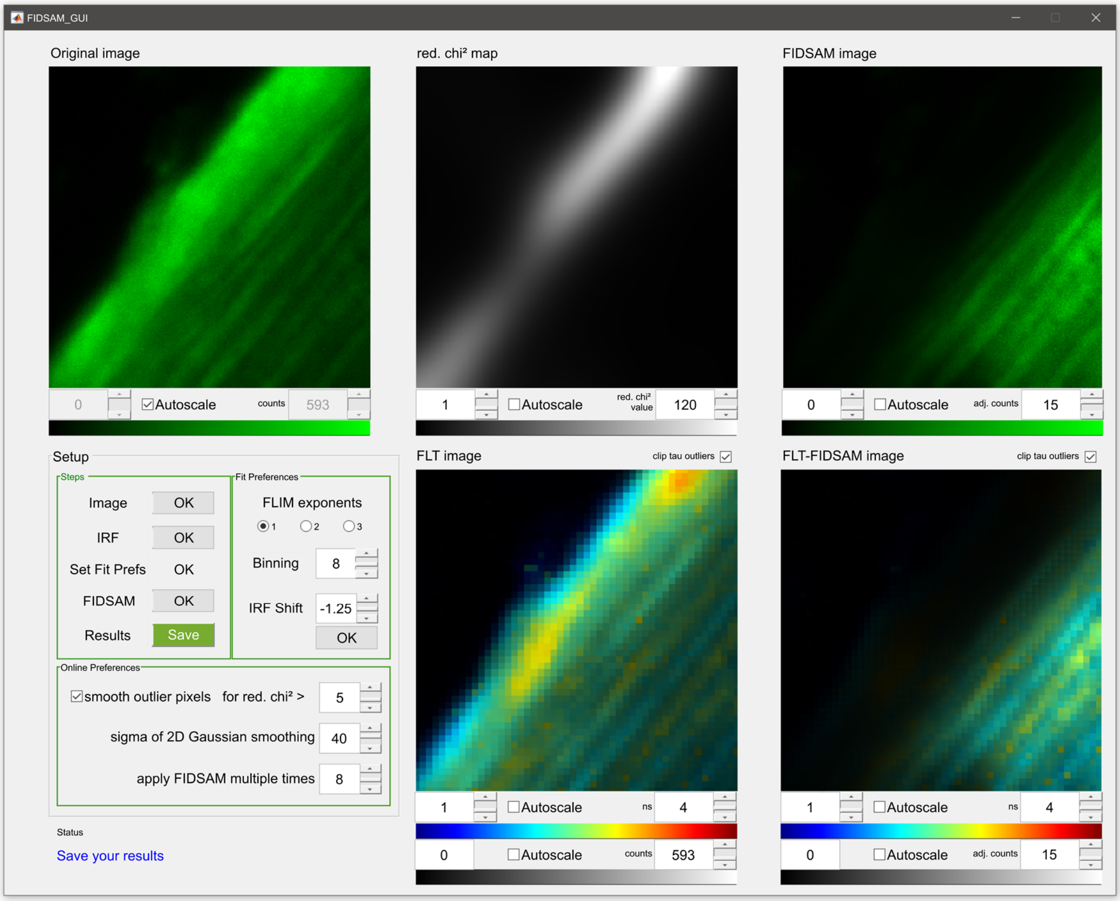

Original image: 0 ☑Autoscale counts 593

red. chi² map: 1 ☐Autoscale red. chi² value 120

FIDSAM image: 0 ☐Autoscale adj. counts 15

Steps: Image OK; IRF OK; Set Fit Prefs OK; FIDSAM OK; Results Save

Fit Preferences: FLIM exponents ● 1 ○ 2 ○ 3; Binning 8; IRF Shift -1.25; OK

Online Preferences:
☑smooth outlier pixels for red. chi² > 5
sigma of 2D Gaussian smoothing 40
apply FIDSAM multiple times 8

Status: Save your results

FLT image (clip tau outliers ☑): 1 ☐Autoscale ns 4; 0 ☐Autoscale counts 593

FLT-FIDSAM image (clip tau outliers ☑): 1 ☐Autoscale ns 4; 0 ☐Autoscale adj. counts 15

Figure 3.5 | New graphical user interface (GUI) for FIDSAM calculations. In the setup box (lower left), users can load images and instrument response function files. Fit preferences are set before applying FIDSAM, the primary results can then be adjusted dynamically with additional settings and saved as bitmap images or ASCII files for further data processing.

The FLT fitting routine utilized parts of the MATLAB program fluofit.m by Jörg Enderlein (III. Physical Institute, University of Göttingen) and was further developed to perform calculations up to six times faster.

An entirely new feature of the FIDSAM software is the removal of outliers. Low photon statistics for a pixel can produce unexpectedly high red. chi^2-values. This might happen occasionally in dark image areas or if binning leaves behind pixels with low photon counts at the edges. These pixels, notably in conjunction with blurring and multiple FIDSAM executions, would dominate the FIDSAM image due to their high error value. The new option replaces outlier pixels exhibiting red. chi^2-values beyond a specified threshold with the average value of their neighboring pixels.

Additionally, the display of FLIM and FLIM-FIDSAM images was corrected. Instead of just overlaying the original intensity image with the FLT values, the overhauled version now uses the photon counts per binned pixel to darken or brighten the pseudo-colored FLT map. This ensures that contrast enhancement does not change a pixel's color but only its brightness, which is the convention used by commercial FLIM software packages like SymPhoTime.

In another new feature, the user can now set the number of exponents used for the FLT decay fitting. This could allow for a more reliable application of FIDSAM to FLIM-FRET experiments. Assuming that a fluorescence decay comprises two rate constants in case of FRET, a biexponential test function can be used to calculate the error values. This should still provide enough contrast to the commonly multiexponential decay curves for the autofluorescence background. A possible further development of the software could add an entirely different fitting type. As MLE algorithms can take into account the Poissonian distribution of photon statistics, they are much more reliable for low photon counts than least-square algorithms. This would be particularly valuable for FLIM of weakly expressed protein constructs. However, fitting with the MLE method relies on maximizing the likelihood function, which is an entirely different parameter than the red. chi^2 value used for FIDSAM. Therefore, the applicability of MLE to FIDSAM still has to be evaluated.

The above examples demonstrate the potential of the modular FIDSAM software: its accessibility and configurability facilitate updates as well as the development of new analysis methods.

3.4 Single-Molecule Spectroscopy of BIFC Model Systems

Bimolecular Fluorescence Complementation is another widely used method to analyze protein-protein interactions, most commonly used in split-YFP assays. Combining spectrally distinct fluorescent protein fragments extends this technique to detect multiple interaction partners in parallel, for example, in different cell compartments (multicolor BiFC). However, the photophysical characteristics of these reconstituted complexes were largely unknown, which essentially precluded a more targeted or quantitative approach of this otherwise powerful technique. That gap of knowledge was the primary motivation for the project [106] presented in this chapter.

As a first step, the photophysical properties of the biological fluorescence markers used in BiFC were analyzed in a controlled environment (in vitro). The molecular biological expression of single BiFC fragments was frustrated by protein aggregation effects. However, by fusing different fluorophore fragments on the genetic level prior to expression, artificially complemented complexes were accessible in high yields and purity. The consequent lack of complementation dynamics was considered negligible as BiFC is regarded an irreversible process. The validity of the so-called, artificial "BiFC chimeras" as an in vitro model system for their in vivo counterparts was assessed in the comparative experiments below.

The analysis depended on three common FPs: mCerulean, enhanced GFP (EGFP) and Venus (their abbreviated fragment designations being C, G and V, respectively). The commutation of all fragments resulted in nine different combinations: three base FPs and six mixed chimeras. This provided a robust basis for the analysis of physical and spectroscopic differences. Additionally, including the base FPs served as both an internal control and a useful reference point for published data. The designations for the BiFC chimeras were based on the employed fragments and their length. For example, G154-V fuses the anterior 154 amino acids of EGFP with the posterior part of Venus, starting with amino acid 155. Accordingly, the combination V-154V just reconstitutes the base FP Venus.

Different spectroscopic methods were employed for a basic characterization, including the ensemble parameters acidity constant $\mathrm{p}K_a$, molar attenuation coefficient ε, fluorescence quantum yield Φ_F, and λ_{abs}, λ_{exc} and λ_{em} as the wavelengths of maximum absorbance, excitation and emission, respectively (Table 1, for additional data see attached publication).

Table 1 | Photophysical and -chemical parameters of selected BiFC chimeras.

	mCerulean	C154-V	EGFP	G154-C	G154-V[a]	Venus
λ_{abs} (nm)	434	469	490	490	515	516
λ_{exc} (nm)	453	471	488	491	515	516
λ_{em} (nm)	477	508	510	511	525	529
pK_a	5.2	5.9	5.8	5.9	8.5	5.7
ε ($M^{-1}cm^{-1}$)	43000	35000	56000	55000	7600	92200
Φ_F	0.48	0.16	0.60	0.6	0.64	0.58
τ (ns)	3.24	2.02	2.73	2.69	3.36	3.15
2σ (SMS) (nm)	n.d.	n.d.	3.3	3.4	10.1	4.5

[a] Indicated values for the fluorescent (deprotonated) form

The ensemble FLT is a crucial parameter for a fluorophore, allowing for an in-depth analysis of its photophysical processes. Favorably, the FLIM extension of the custom microscope setup (presented in more detail in chapter 4.2.5) provided easy access to this important parameter. To obtain the ensemble FLTs of the BiFC chimeras, a 10 µL drop of a micromolar, buffered solution was deposited on a coverslip, while the excitation laser focused into the drop to avoid possible reflections. Due to thermal convection, fluorophores in the confocal volume were constantly exchanged. This rendered photobleaching irrelevant when collecting the average photon arrival times and allowed for fast FLT analyses with minimal sample quantities, easily verified with standard substances.

While the ensemble experiments already offered a solid foundation, they only represented the average over possibly multiple emitter subpopulations or other statistical peculiarities. Therefore, many interesting photophysical properties remain hidden in these kinds of measurements and can only be uncovered with single-molecule experiments. Fulfilling the requirements for single-molecule sensitivity, the custom-built microscope allowed access to such cutting-edge spectroscopic techniques. For this project, the statistical distribution of emission maxima was of special importance, as it relates to the chromophores' direct physical environment. In case of fluorescent proteins, the spectral distribution indicates the rigidity of the protein β-barrel that encapsulates the central chromophore. Highly diluted, buffered samples were prepared in a thin-film polymer matrix on a meticulously cleaned cover slide. The used polymer polyvinyl alcohol (PVA) had two advantages: a) it produced pores large enough to take up BiFC complexes in a quasi-natural environment provided by the buffer solution; and b) the polymer film reduced oxygen permeation to decrease photobleaching. After acquiring a raster-scanned overview image, spectra were taken from bright, spatially well isolated fluorescence spots (Figure 3.6a). In contrast to small organic dyes, fluorescent proteins are relatively dark and photolabile. Consequently, robust statistical data analysis required hundreds of spectra for each BiFC chimera and placed the highest demands on a microscope platform in terms of sensitivity and reproducibility.

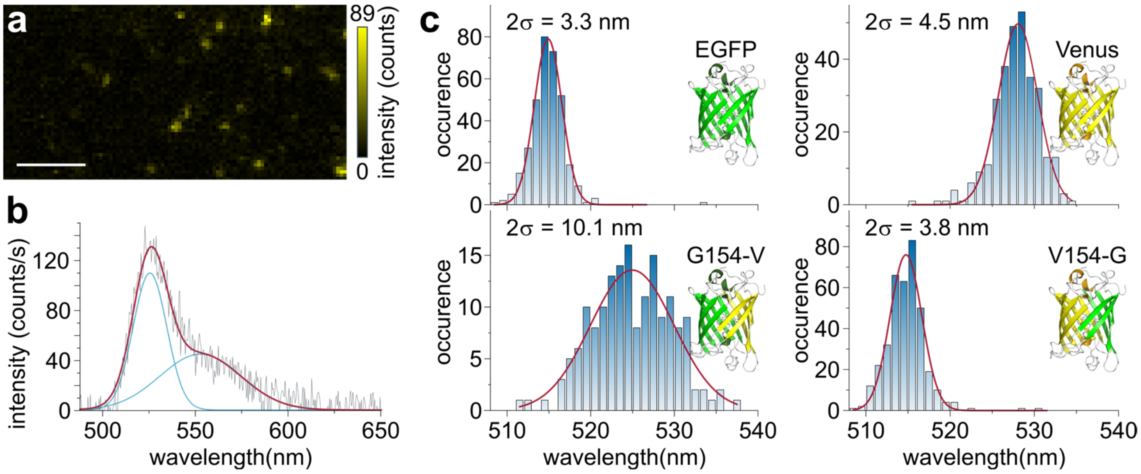

Figure 3.6 | Spectral distribution analysis for selected BiFC chimeras. (a) Confocal fluorescence image of single fluorescence proteins (Venus) embedded in a thin PVA film matrix. Scale bar, 2 µm. **(b)** Fluorescence spectrum of a single Venus molecule, fitted with two Gaussians (blue curves). The emission maximum was determined from the sum of the Gaussians (red curve). **(c)** Statistical analyses of the emission maximum positions found for EGFP (n = 338), Venus (n = 300), G154-V (n = 167) and V154-G (n = 371). Normal distribution fitting (red curves) of the histograms provided the indicated spectral distribution widths (2σ).

In this study, large collections of single-molecule spectra were successfully acquired and each spectrum was analyzed to determine its emission maximum position (Figure 3.6b). Statistical analysis uncovered the spectral distribution width as an important single-molecule parameter (Figure 3.6c). Furthermore, the distribution maxima were in good agreement with the respective ensemble emission maxima. The combination of certain BiFC fragments had significant influence on the rigidity of their protein shell, pointing to structural features which were not always inferable from the ensemble information alone. The above findings not only provided a basis to choose the most feasible combinations in practical multicolor BiFC assays, but also demonstrated previously unreported influences of certain amino acids in the fluorophore protein shell. A detailed interpretation of all collected photophysical parameters can be found in the accompanying publication [106].

Additionally, the spectroscopic characteristics found in vitro were compared with data under physiological conditions. To this end, protein combinations known to interact in vivo were co-expressed with BiFC fragments. The three selected fragments were either the N-terminal parts of Venus (VenN) or mCerulean (CerN) or the C-terminal part of Venus (VenC). As the basic leucine zipper bZip63 readily forms homodimers, the interaction of bZip63-VenN and bZip63-VenC would reconstitute a fluorophore comparable to in vitro Venus. Another interaction partner, the two-component response regulator ARR18, can form heterodimers with bZip63. Accordingly, the combination ARR18-CenN with bZip63-VenC would result in a fluorophore comparable to in vitro C154-V.

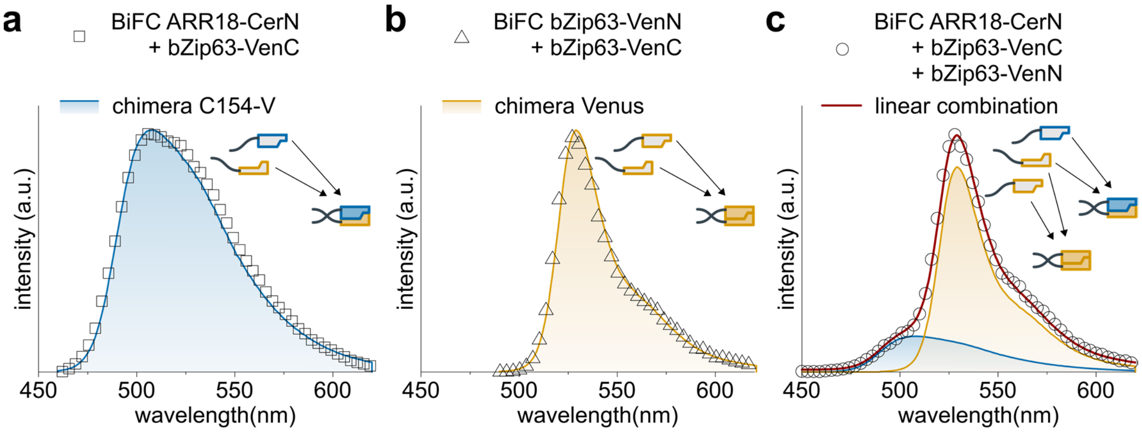

Figure 3.7 | In vivo validation of BiFC chimeras as a model system. (a) Fluorescence spectra from in vivo reconstituted BiFC fragments ARR18-CerN and bZip63-VenC (squares) and the corresponding in vitro spectrum of BiFC chimera C154-V (blue curve). **(b)** Fluorescence spectra from in vivo reconstituted BiFC fragments bZip63-VenN and bZip63-VenC (triangles) and the corresponding in vitro spectrum of BiFC chimera Venus (yellow curve). **(c)** In vivo reconstitution of all three aforementioned fragments. The raw data (circles) is in good agreement with a linear combination (red curve) of the two possible BiFC combinations (in vitro spectra and color scheme same as in **a** and **b**). For more clarity, compare the schematic representations of the involved fragments. All in vivo spectra were acquired from the nuclei of transiently transformed *N. benthamiana* plants.

Combinations of these constructs, expressed in the nuclei of transiently transformed *N. benthamiana* plants showed a slight offset in the FLTs which is common and most likely caused by the different environment in a live cellular matrix in comparison to a buffer solution. The in vivo fluorescence spectra were, however, in perfect agreement with the in vitro data (Figure 3.7a,b). This validated the use of artificial BiFC chimeras as a model system for live cell BiFC assays. Sum spectra of multiple, coexistent BiFC complexes (Figure 3.7c) depend on the parameters of their individual complexes, which were collected during the thorough photophysical characterization (see Table 1). This now allowed for linear unmixing and the calculation of their relative amounts, furthermore verifiable by analogous calculations involving their respective FLTs. This served to show the first quantitative estimation of protein complexes in a multicolor BiFC assay.

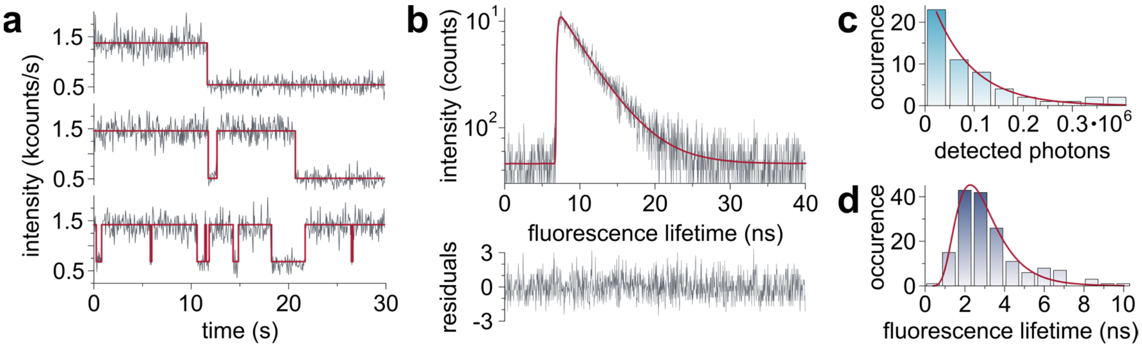

Figure 3.8 | Additional single-molecule spectroscopy characteristics of Venus. (a) Typical single-molecule time traces, showing bleaching and intermittent blinking. For better visibility, the spectra were fitted with a simple threshold algorithm (red curves). **(b)** Single-molecule FLT decay curve with a monoexponential fit (red curve) and residuals. **(c)** Statistical analysis of the photon output of single fluorescence proteins. For time traces indicating single-molecule fluorescence with one terminal bleaching step (the upper two spectra in **a**), the detected photons were calculated by integration after background subtraction. As photobleaching constitutes a spontaneous decay process from the first excited singlet state, the resulting histogram (n = 57) can be fitted with a monoexponential function (red curve). **(d)** Statistical analysis of single fluorescence lifetimes. Only time traces that showed single-molecule behavior and FLT decay curves with acceptable signal-to-noise ratios (compare **b**) were included. The resulting histogram (n = 168) followed a lognormal distribution (red curve).

In combination with TCSPC, further experiments with the BiFC chimeras were conducted on the single-molecule level to investigate their photophysics in more detail. Since some chimeras were too photolabile to include them in all single-molecule experiments, only the decidedly more robust spectral distribution analysis was included in the publication. Nevertheless, Figure 3.8 shows additional single-molecule spectroscopy parameters, which could be valuable for future, similar experiments. While the observation of antibunching is the most reliable proof of a single emitter, fluorescence time traces can also provide strong evidence. This can be seen in Figure 3.8a, where the time traces show similar intensities at two distinctive levels ("on" and "off"). The detected photons up to the final bleaching step can be statistically analyzed and correlate with the photostability of the fluorophore (Figure 3.8c). Likewise, blinking statistics can be derived from such time traces, which are important characteristics for fluorophores used in SMLM techniques. Similar to the spectral distribution width, single-molecule fluorescence decay curves (Figure 3.8b) can also be used to analyze the statistical distribution of FLTs (Figure 3.8d).

In summary, fluorescence spectra and FLTs are crucial components for in-depth studies of living systems and extremely beneficial for any microscope platform. Moreover, the capability for single-molecule analyses allowed for an extensive physicochemical approach to characterize widely-used probes in live cell fluorescence imaging. As the in vivo validation can be performed on the same microscope platform, this combination proves to be a powerful tool for the development or enhancement of spectromicroscopy techniques.

3.5 Superresolution Microscopy

The previous chapter illustrated that single-molecule studies can reveal many properties of a system that remain hidden in the ensemble. Similarly, this concept also applies to fluorescence imaging: overlapping PSFs obscure the spatial arrangement of the underlying single emitters, thereby limiting the resolution in optical microscopy. Since many biological functions are organized on the length scale of molecules, this significantly limits the available information in live cell microscopy. Accordingly, single-molecule sensitivity is essential for imaging techniques that aim to unravel the complex molecular machinery of life.

Over the last decades, this was reflected in the remarkable rise of optical superresolution techniques utilizing single emitter properties. The following subchapters will highlight several of these methods and their application in life sciences.

3.5.1 Application of dSTORM to Biological Test Samples

To establish superresolution based on localizing single molecules, good signal-to-noise ratios are of utmost importance. Therefore, the use of highly sensitive detectors and TIRFM or variable-angle illumination were prerequisites to achieve high contrast. For the following experiments, direct STORM (dSTORM) was applied, a straightforward superresolution technique featuring continuous illumination and image acquisition. Accordingly, this renders synchronization and parameterization procedures unnecessary and also takes advantage of the sCMOS camera’s high frame rates for fast data acquisition. In the search for an appropriate sample, York Stierhof (ZMBP, University of Tübingen) proposed and produced immunolabeled cryosections of protozoan parasites *Trypanosoma brucei*. These ca. 20 µm long, unicellular eukaryotes use a single flagellum for cell propulsion. The cytoskeletal core of the flagellum consists of a microtubule-based 9 + 2 axoneme with a diameter close to the diffraction limit (200 nm). Therefore, its highly ordered structural elements are resolvable in electron micrographs (Figure 3.9a), but not with classical light microscopy. Immunolabeling of the microtubules with the fluorescent organic dye Cy3 thus would demonstrate if these structures could be resolved with dSTORM. In fact, the specimen had several advantages: a) the biological nature allowed for a direct assessment of the technique in a biological context; b) the fixation of the sample eliminated movement during the acquisition; c) organic dyes are bright and stable fluorophores; d) the small sample thickness of 100 nm further improved contrast; and e) similar samples were imaged with a commercial microscope featuring GSDIM, which could serve as a benchmark.

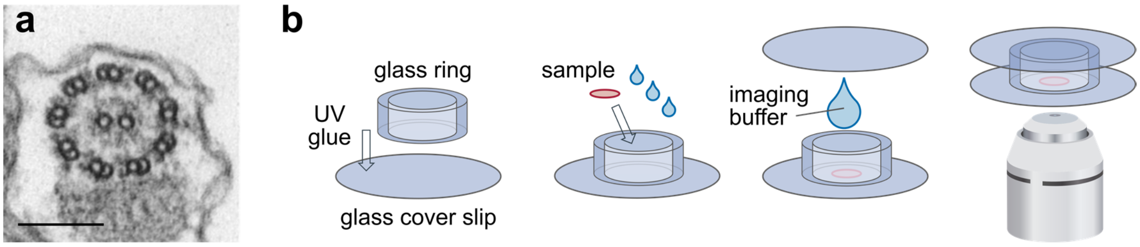

Figure 3.9 | Test sample structural features and preparation for dSTORM analysis. (a) Thin-section transmission electron micrograph showing a cross section through a *Trypanosoma brucei* flagellum, revealing microtubules in the 9 + 2 axoneme arrangement. Adapted from [107]. Scale bar, 100 nm. **(b)** Sample chamber construction for dSTORM measurements. A small glass ring was affixed to a cover slip (30 mm diameter) with UV glue. After transferring the sample section into this small basin, immunolabeling and washing steps were performed. Prior to measurements, 1 mL of imaging buffer was added and the sample chamber was sealed by capping it with another coverslip on top.

Samples were prepared on a clean coverslip inside an affixed glass ring (Figure 3.9b). This allowed for the copious addition of imaging buffer solution which was capped with another coverslip on top, reducing evaporation and permeation of additional oxygen. The imaging buffer was prepared with 1 mg/mL glucose oxidase (G7141-10KU, Sigma), 0.08 mg/mL catalase (C9322-1G, Sigma), 10% (w/v) glucose, 137 mM β-Mercaptoethanol (M6250-100ML, Sigma) and 2 mM COT (138924-1G, Sigma) in a buffer solution containing 154 mM Tris and 38 mM NaCl, adjusted to pH 8.0.

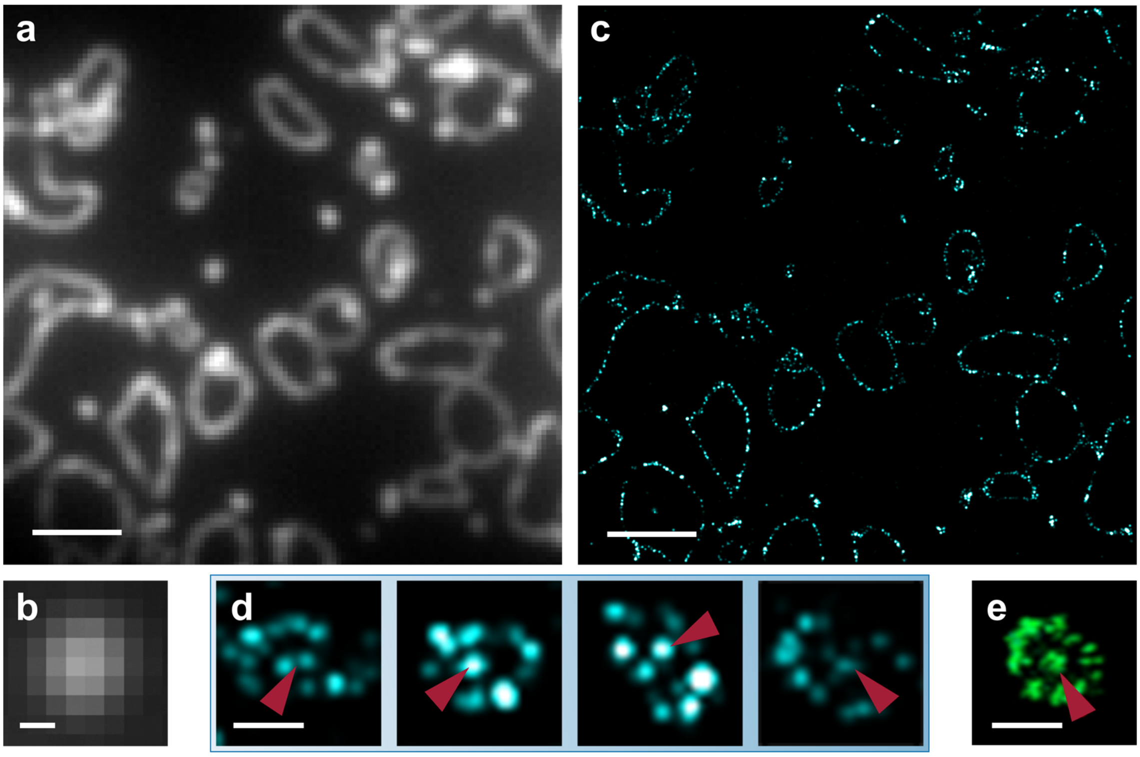

Figure 3.10 | Application of dSTORM to biological test samples. (a) Conventional TIRF microscopy image of trypanosome cells (100 nm thin cryosection, microtubules immunolabeled with Cy3). **(b)** Diffraction-limited expanded view of a crosscut flagellum. **(c)** dSTORM superresolution image of **a**. Each fluorophore localization in the image is enlarged by its respective localization precision. **(d)** Examples of superresolved flagella. The red arrows point to the position of the central microtubule pair. **(e)** Comparison measurement, using GSDIM (Leica). Scale bars, 2 µm (**a**,**c**), 200 nm (**b**,**d**,**e**).

For comparison, a diffraction-limited image was acquired (Figure 3.10a). While the outline of trypanosome cells can be seen (the fluorescently labeled microtubules are also part of their cytoskeleton), their crosscut flagella showed no discernible substructures (Figure 3.10b). Constant illumination with the imaging laser (561 nm) lead to stochastic blinking of the fluorophores which was further adjusted with a second activation laser (405 nm). After achieving sufficient spatial separation of single-molecule fluorescence events, 10000 movie frames were acquired with 100 frames/s (10 ms acquisition time per frame). Subsequently, the open-source software Localizer [108] analyzed the movies on a frame-by-frame basis to determine the emitters' center positions. More precisely, an image segmentation algorithm first located viable fluorescence spots that were then fitted by a 2D Gaussian function. The emitter positions in all frames were displayed in one image, with each position point enlarged by its respective localization precision (Figure 3.10c). The trypanosome cells now showed much sharper and dotted outlines, attributable to microtubule bundles in the cytoskeleton. In further contrast to the diffraction-limited image, crosscut flagella revealed their substructure; for individual cases, even the separation of the inner two microtubules (Figure 3.10d, red arrows) became visible. Superresolution images acquired by York Stierhof at a commercial microscope featuring GSDIM (Figure 3.10e) were of comparable quality, their resolution was estimated to be better than 50 nm. These results show that the addition of single-molecule localization based superresolution to the microscope platform was certainly successful. This capability was further validated by a related experiment presented in chapter 3.5.2.

Depending on the sample system, it might be more appropriate to use PALM with photo-switchable fluorescent proteins as tags. On the technical side, this involves the synchronization of activation laser pulses with intermittent image acquisition. Fortunately, these requirements are fulfilled by the microscope platform as it can be controlled with customizable software packages (see chapter 4.2.6). Freely available algorithms can be used to adjust pulse durations and image acquisition in real time, compensating for falling signal intensities in the course of an experiment.

The performance of the technique presented in this chapter largely relies on clean sections, proper labeling and the photophysical characteristics of the fluorophores. For the above experiment, Cy3 was the best dye available at the time for immunolabeling. However, other fluorophores like Cy3B show better photon statistics for the same excitation wavelength, and red-shifted fluorophores like Alexa 647 are reported to perform even better in dSTORM experiments [60]. As discussed in chapter 2.5, immunolabeling with secondary antibodies can introduce up to 20 nm between the structure and the fluorescence label, thus limiting the achievable resolution. Depending on the target protein, the specificity or quality of available antibodies might also be insufficient. These problems can in part be circumvented if the protein can be fused to GFP that is then targeted with high-affinity camelid antibodies (so-called nanobodies) [109]. These highly specific anti-GFP nanobodies are easily labeled with bright organic fluorophores and are only 2.5 nm in size, which significantly shortens the linking distance (including GFP) between structure and label below 10 nm.

In summary, the test sample in this chapter already demonstrated the impressive gain in structural information. By adjusting the aforementioned parameters, it will be possible to improve the resolution even more. The logical next step was to apply this technique to a research project, which will be presented in the next chapter.

3.5.2 Structural Analysis of Nucleic Protein Clusters With SOFI

Non-coding introns play a key role in the regulation of gene expression. They not only enable proteome diversification by alternative splicing, but also positively influence transcription, RNA stability and translation. Nevertheless, intron-less genes (ILGs) are abundant in all higher eukaryotes. In particular, plant genomes comprise up to 20% ILGs. They make up for their lower expression levels by a much higher transcription speed, which can prove beneficial in situations when gene expression has to be changed quickly, for example, environmental stress. The higher responsiveness of ILGs and intron-poor genes (IPGs) could be shown for many crop model species exposed to drought, osmotic or cold stress. Therefore, their regulation is a highly interesting research topic. In *A. thaliana*, the SERRATE (SE) nucleic protein was found to be an important regulator of ILGs and IPGs. This project analyzed its function with numerous biochemical and molecular biological experiments, as can be read in detail in the accompanying manuscript [110].

This chapter, however, will focus on the application of superresolution imaging to a part of the overall investigation. SE binds DNA mostly at exonic regions and close to transcriptional start sites. SE also enables protein-protein interactions, possibly recruiting or associating transcriptional enzymes like RNA polymerase II (pol II). Therefore, it was of great interest if such recruitment processes can be observed in cell nuclei. Colocalization experiments already showed that SE and pol II accumulate in cell nuclei clusters, but due to diffraction-limited imaging their exact spatial arrangement was still obscured (Figure 3.11a).

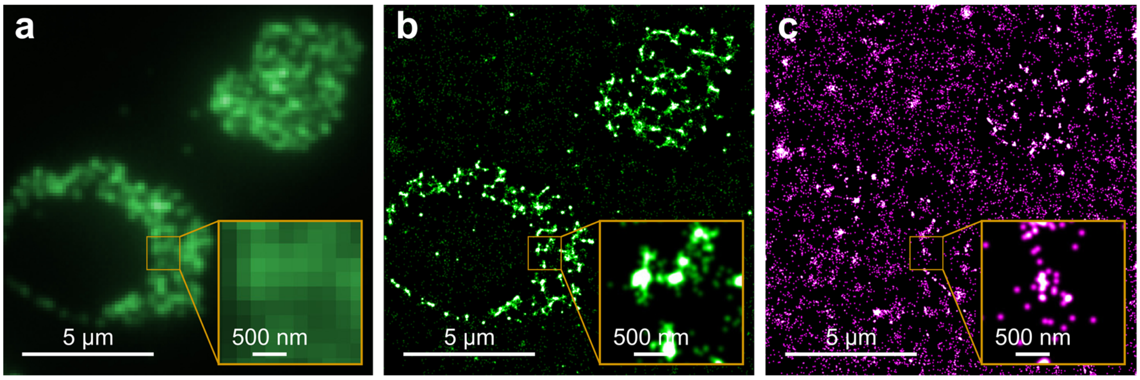

Figure 3.11 | Application of dSTORM to protein clusters in cell nuclei of *A. thaliana*. **(a)** Conventional TIRF microscopy image of a 100 nm thin cryosection, showing two cell nuclei. RNA Polymerase II (pol II) was immunolabeled with Alexa Fluor 488 (green), SERRATE (SE) was immunolabeled with Cy3 (not shown in this channel). **(b)** Superresolution image of **a**, using dSTORM. **(c)** Superresolution image of SERRATE (SE) immunolabeled with Cy3 (magenta), using dSTORM. Insets show expanded views of the respective yellow-boxed regions.

This limitation provided an excellent opportunity to apply superresolution, thus validating the superresolution capability presented in chapter 2.4.1 with a current research project. The cryosection of four-day-old *A. thaliana* seedling root tips provided thin (100 nm) specimen slides that were thawed and subjected to immunolabeling. Effectively, this procedure tagged pol II and SE proteins with the organic dyes Alexa Fluor 488 and Cy3, respectively. Superresolution imaging with dSTORM was performed as described in chapter 3.5.1. First, image acquisition of Cy3 tagged structures with 561 nm excitation was conducted until all Cy3 fluorophores were bleached. This made sure that they would not influence the subsequent recording of the Alexa Fluor 488 tagged structures with 488 nm excitation. Inspection of the superresolved images revealed a significant resolution gain for the localization of pol II, allowing for a far better contrast than in TIRF microscopy (Figure 3.11b). However, because of the strong background that is especially severe for SE (Figure 3.11c), a reliable interpretation of protein cluster arrangements was hardly possible. As dSTORM works best inside a narrow range of labeling densities, it can be frustrated if too many fluorophores have to be bleached before acquiring separated fluorescence spots for each image. Although different labeling densities and illumination schemes were applied, the densely fluorescent regions in the sample were difficult to deal with. This is partly due to the localization algorithm, which intrinsically excludes clustered spots occurring in one frame from the localization procedure. In consequence, it can also be observed that not all fluorescent spots in the TIRF microscopy image seem to have their counterparts in the dSTORM image.

Therefore, an alternative superresolution approach had to be used. Superresolution Optical Fluctuation Imaging (SOFI) proved to be a viable method, as it also relies on blinking fluorophores in a series of images, but copes much better with high labeling densities and provides excellent background suppression. For this, the illumination parameters were adjusted to achieve high, but fluctuating intensities over the course of the image acquisition. Data processing was performed by the open-source Localizer software package which also includes SOFI routines. The recorded image sequences underwent second-order correlation analyses, generating superresolved images which were further deconvolved with three iterations of a Richardson-Lucy algorithm using a Gaussian point spread function ($\sigma = 1.6$ pixels). Although second-order SOFI typically improves the resolution only by a factor of $\sqrt{2}$ [64], the obtained images showed a drastically improved contrast in comparison to the diffraction-limited epifluorescence images (Figure 3.12). This allowed for a more refined interpretation of the cluster arrangements. The intensity line scans (compare insets in Figure 3.12a,c) are much clearer in the SOFI image and show that SE and pol II indeed localize to different clusters. However, they mostly adjoin or slightly overlap each other, strongly pointing to some kind of recruitment process.

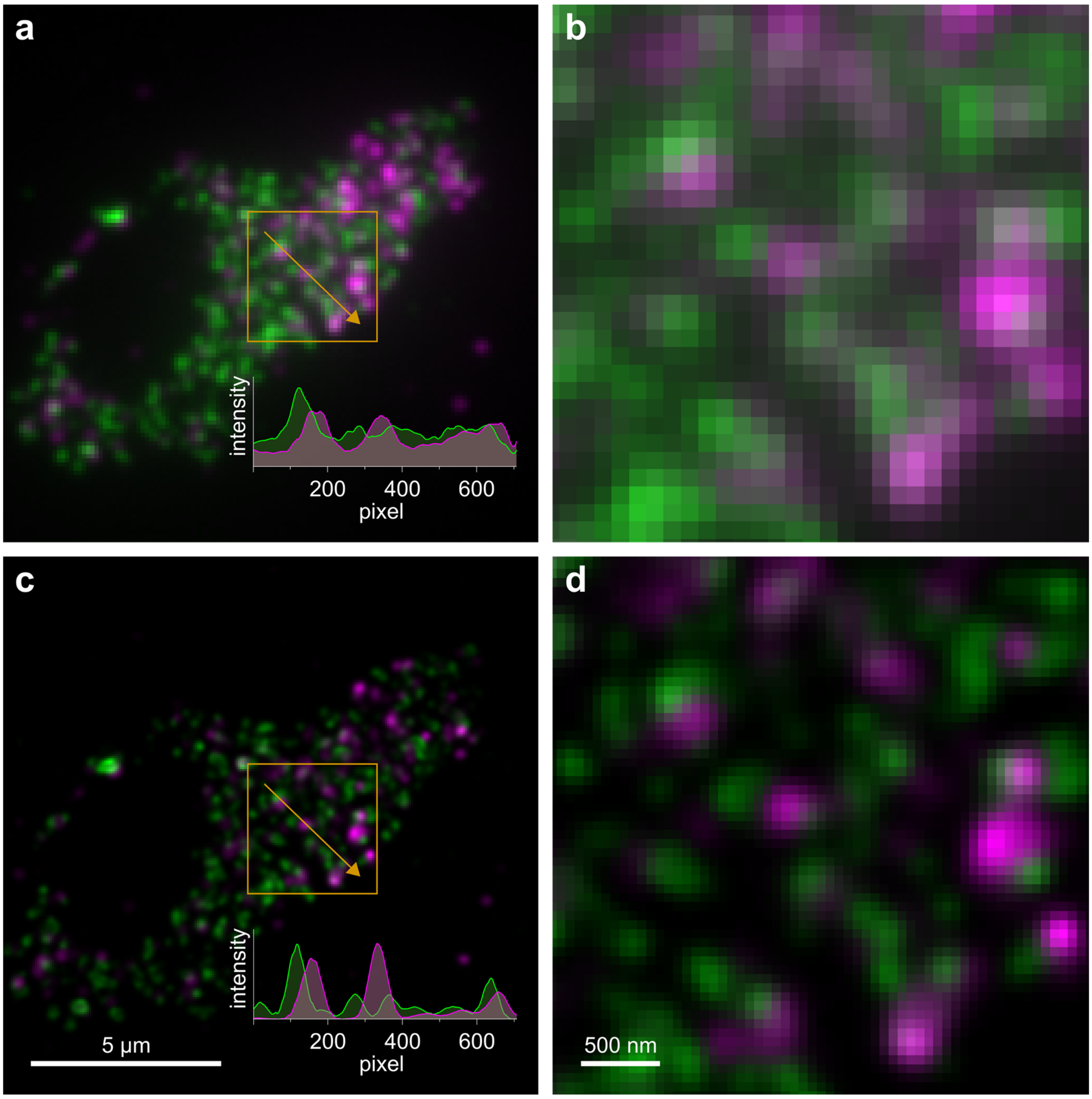

Figure 3.12 | Application of SOFI to protein clusters in cell nuclei of *A. thaliana*. (a) Merged images of pol II tagged with Alexa Fluor 488 (green) and SE tagged with Cy3 (magenta) in thin sections of *A. thaliana* nuclei, acquired with conventional TIRF microscopy. **(c)** Corresponding SOFI image. (**b**,**d**) Expanded views of the yellow-boxed regions in **a** and **c**, respectively. Insets: line profiles along the pixels indicated by the yellow arrow.

In addition to SOFI, the samples were also imaged with a commercial setup featuring another superresolution method (ZEISS LSM 880 with Airyscan). This technique records the information of out-of-focus light which is usually rejected at a pinhole. For each image pixel, the airy disk is recorded by an array of 32 circularly arranged GaAsP detectors. This results in 32, slightly shifted images which are then deconvolved to produce a higher-resolved image (ZEISS specifies an improvement factor of 1.7) with improved signal-to-noise ratio. This allowed for a direct comparison of this commercial technique with SOFI on the custom-built setup. As demonstrated in Figure 3.13, the SOFI images were very similar to those obtained with the Airyscan mode, and also colocalization analyses using line scans revealed comparable results. Both SOFI and Airyscan rely on mathematical algorithms to generate the final images, it is therefore generally advisable to exert caution when interpreting such inherently artificial visual representations. However, as both methods are based on very different acquisition modes and image reconstruction techniques, their matching results mutually support the abovementioned conclusions for cell biology. Furthermore, the similar contrast enhancement shows that SOFI on the custom-built microscope platform compares well to commercial standards. It should be pointed out that, in this case, Airyscan benefits from the ultrathin section preparation which removes the influence of out-of-focus light in *z*. SOFI inherently achieves this sharp contrast in *z* by TIRFM illumination and, therefore, suffers no quality losses when samples cannot be sectioned as thinly. Moreover, SOFI was applied quite cautiously to exclude possible artifacts, using only second-order correlation functions. The possibility to compare SOFI images with results from dSTORM and Airyscan microscopy allows for a better understanding of potential sources of error, also owing to the experience gained with this technique in the course of this project. Therefore, other SOFI varieties will be validated that use higher-order cross-cumulants (as mentioned in chapter 2.4.3) to enhance the contrast even further for future experiments.

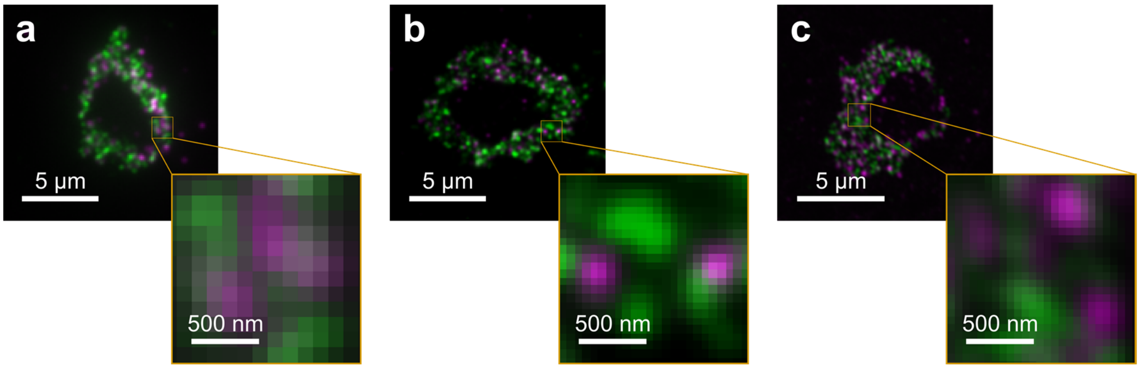

Figure 3.13 | SOFI in comparison with ZEISS Airyscan. (a) TIRF microscopy image. **(b)** SOFI image. **(c)** ZEISS Airyscan image. All images show pol II tagged with Alexa Fluor 488 (green) and SE tagged with Cy3 (magenta) in thin sections of *A. thaliana* nuclei.

In principle, SOFI, dSTORM or PALM can be combined with interaction experiments like FLIM-FRET. Confocal imaging can be performed with low laser intensities to preserve fluorophore intensities for subsequent superresolution techniques. However, in standard immunolabeling procedures, the fluorophores are often bound to a secondary antibody. This can introduce distances of up to 20 nm to the labeled structure, which is too far for efficient energy transfer. If this labeling problem can be overcome, for example, with the aforementioned SNAP-tag, CLIP-tag or anti-GFP nanobodies, then interaction maps with confocal resolution could be overlaid with superresolved structural information, allowing deeper insights into the distribution of the involved target molecules. Of course, this requires that both techniques can be performed on the same microscope platform without moving the sample.

In conclusion, this chapter presented the successful application of the superresolution method SOFI in the context of a current research project in cell biology. When initial problems with dSTORM led to unsatisfactory results, the variety of the microscope platform (concerning instrumentation and analysis methods) proved helpful to establish SOFI as a viable alternative. Nevertheless, supported by the continuous development of analysis algorithms and the employ of better suited immunolabels, it should be possible to study even such demanding samples with dual-color dSTORM in the near future.

Not only the structural arrangement of protein clusters, but many important biological processes happen in spatial dimensions that were previously unreachable in live cell imaging. With the emergence of superresolution imaging techniques over the last decades, the direct observation an organism's molecular machinery finally comes within reach. Therefore, their benefit for a modern research microscope is very high. Although SMLM methods are generally more suited to acquire structural information in fixed samples due to their comparably long acquisition times, researchers managed to collect 32 superresolved images per second in living cells [59]. However, the next chapter will present a superresolution technique that can be applied more generally and is well suited to analyze in vivo dynamics and kinetics.

3.5.3 Validation of sptPALM by a comparative study

Cells, the smallest biological units of an organism, heavily rely on the interaction with each other and their surroundings. Physically separating the cytoplasm and interior components from the extracellular environment, the plasma membrane plays an integral role in countless processes, for example, ion homeostasis, transportation of nutrients, and signaling. As the plasma membrane is a thin, but densely packed cell organelle in which proteins and other molecules are highly mobile, high-quality analytical procedures are required to decipher the functions of their components. Live cell imaging microscopy can provide an important tool to observe such processes at work: single particle tracking in cell membranes. Many signaling pathways are mediated by interacting membrane proteins. Tagged with fluorescent markers, they can be visualized to analyze essential parameters such as their distribution and dynamics.

Among the requirements for single-particle tracking are: a) single-molecule sensitivity; b) the capacity to image live cell membranes with high signal-to-noise ratio; and c) a high-resolution camera with high frame rates to gain access to fast dynamics. These capabilities were already demonstrated in the previous chapters; in particular the ability to use TIRFM or VAEM is highly beneficial to image plant membranes that are additionally surrounded by a cell wall. Therefore, it stands to reason that single particle tracking is a feasible and important biological technique worth adding to the microscope platform. This chapter serves to validate the capacity for this important biological analysis tool by comparison with published data.

Since membrane proteins typically occur in large numbers, they often cannot be reliably tracked over longer times, in particular when their fluorescence signals spatially overlap or they cross paths with each other. In many cases, membranes are packed so densely that single fluorophores markers cannot be localized at all. However, this can be alleviated by the use of photo-switchable fluorescence proteins as tags. By controlling the number of visible emitters per image frame, the requirement for their spatial isolation can be met. Therefore, this combination of single particle tracking with fluorescent tags used in PALM (thus designated sptPALM) allows access to analyze even ubiquitous membrane proteins and also benefits from the localization algorithms used in single-molecule based superresolution techniques.

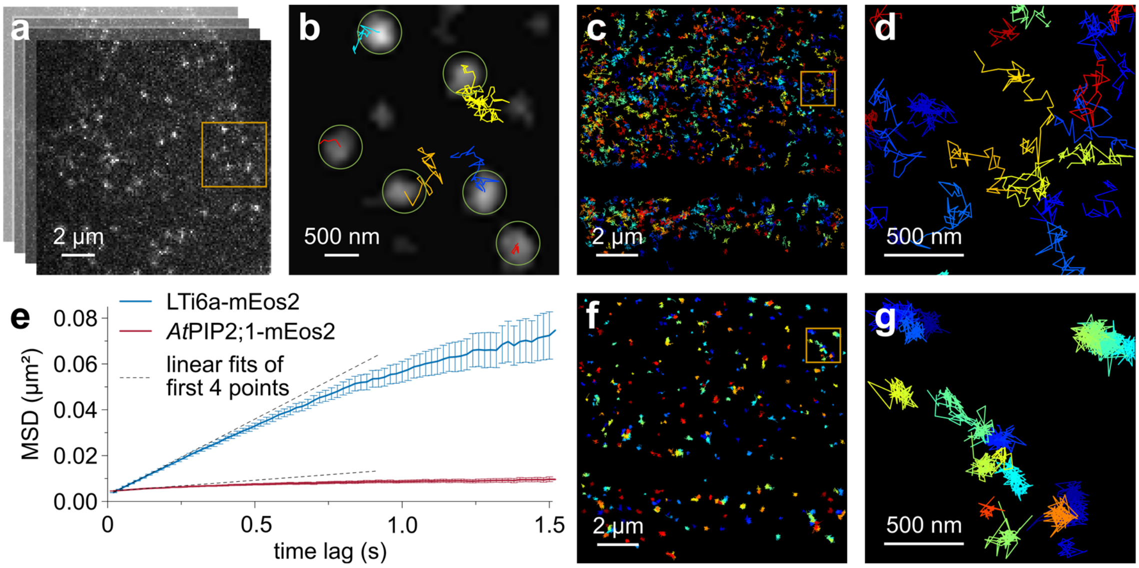

Figure 3.14 | Single particle tracking with PALM (sptPALM), applied to membrane proteins. (a) One frame of a longer movie acquired with VAEM (10000 frames, 50 frames/s), showing single fluorescence spots (LTi6a-mEos2 fusion proteins) in the plasma membrane of *A. thaliana* root cells. **(b)** Expanded view of the yellow-boxed region in a. For better visibility, the image was brightened and smoothed with a 2-D Gaussian filter. Green circles indicate single proteins found by the localization algorithm. The colored tracks show their respective paths up to this movie frame. **(c)** Tracking image of the movie a with arbitrary coloring for each protein. **(d)** Expanded view of the region in **c** enclosed by the yellow box. **(e)** MSD analysis of two different membrane protein fusions LTi6a-mEos2 (red curve) and *At*PIP2;1-mEos2 (blue curve). The dashed lines indicate linear fits for the first four data points to calculate the respective diffusion coefficients. (**f**,**g**) As in **c**,**d**, but with *At*PIP2;1-mEos2.

A recent study employed the photo-convertible fluorescent protein mEos2 as a marker in an experiment designed to show the applicability of sptPALM in plant systems [111]. Among other results, the researchers demonstrated the markedly different diffusion constants of membrane proteins LTi6a (low temperature inducible protein) and *At*PIP2;1 (plasma membrane intrinsic protein). After acquisition of the plant material (seedlings of stable transformed lines of *A. thaliana*), all experimental parameters in the original publication were followed closely. The root cells of seven-day-old seedlings were analyzed with sptPALM, using a 405 nm laser to convert small subsets of mEos2 to their red form and a 561 nm laser for imaging. The illumination intensities were tuned to ensure well separated fluorescence spots that were visible over multiple frames (Figure 3.14a). Superresolved particle tracks (Figure 3.14b) were obtained with the open-source software Localizer that was also used for dSTORM and SOFI in the previous chapters. This information was then exported to the MATLAB routine msdanalyzer [112] to draw particle tracks (see Figure 3.14c,d for LTi6a-mEos2 and Figure 3.14d,g for *At*PIP2;1-

mEos2) and calculate MSD plots (Figure 3.14e). Data analysis first involved the calculation of MSD plots for each individual trajectory lasting longer than 160 ms. Diffusion coefficients (D) were obtained by fitting the first four data points by a linear regression, the distribution of the log(D) values was then plotted as histograms (Figure 3.15a). The Gaussian fit functions in this representation indicate that the diffusion coefficients follow a lognormal distribution and that LTi6a is significantly more mobile than *At*PIP2;1. To determine the biological variability, the tracks were grouped by cells and each group subjected to an analysis as in Figure 3.15a. The log(D) values at their respective distribution maximum were plotted per cell and per membrane protein fusion in Figure 3.15b. To roughly determine the diffusive behavior, the mean MSD was calculated for all trajectories lasting longer than 400 ms and observed in a timescale of 0.5 s (Figure 3.15c).

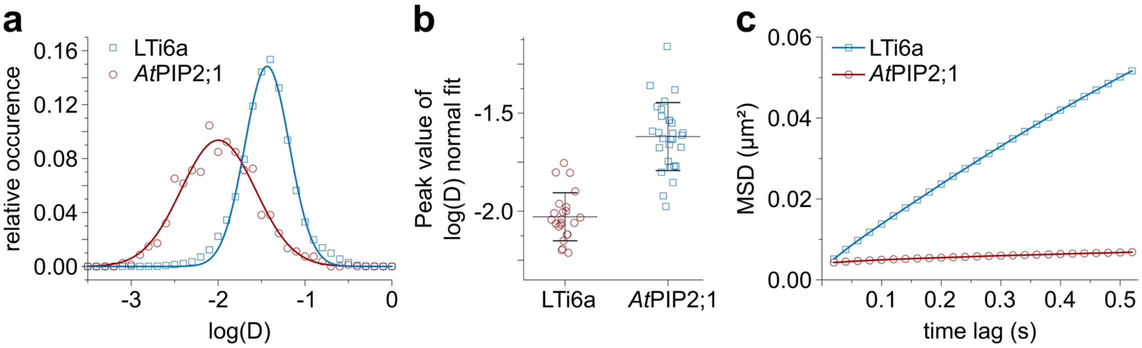

Figure 3.15 | Analysis of sptPALM data. (a) Histograms of individual log(D) values for LTi6a-mEos2 (blue squares) and *At*PIP2;1-mEos2 (red circles) fusion proteins follow lognormal distributions (blue and red curves). **(b)** Peak values of log(D) distributions, grouped by individual cells. **(c)** Mean MSD plots for all trajectories per protein fusion over 0.5 s.

The comparison of the experimental data with the respective data of the original publication were in good agreement. The results proved to be very similar, showing high motility of LTi6a and clearly stationary behavior of *At*PIP2;1. Consequently, the successful completion of this experiment adds sptPALM to the available techniques of the microscope platform.

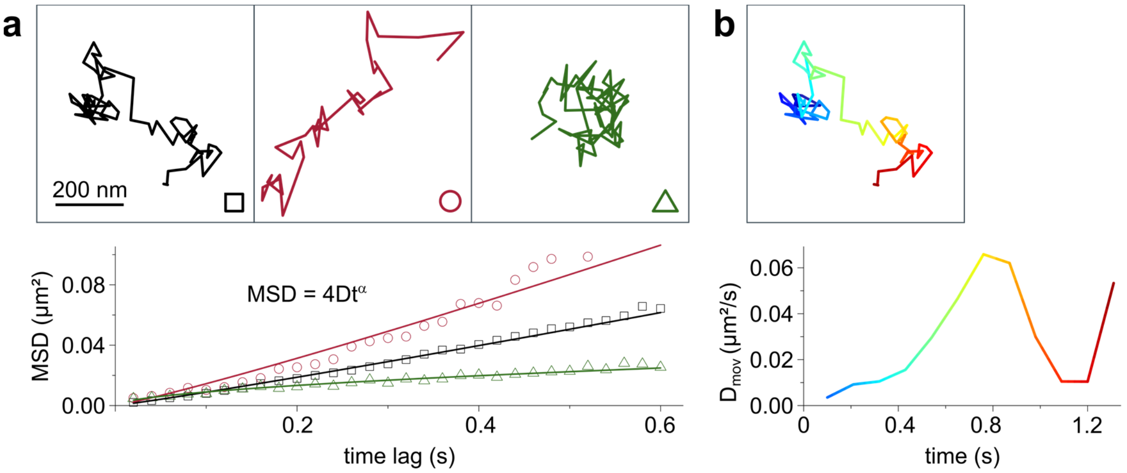

Figure 3.16 | Experimental data showing anomalous diffusion. (a) Top: three LTi6a-mEos2 protein fusions, showing free diffusion (black square), superdiffusive behavior (red circle) and subdiffusive behavior (green triangle). Bottom: corresponding MSD curves with that were fit with a linear regression in their respective log-log plots to determine the anomalous exponent α. **(b)** Using a moving time frame of 0.4 s, D values can be calculated for the corresponding track fragments. The colors also reflect the time progression of the particle track.

The collection of single-molecule data in sptPALM is ideal for statistical analyses, for example, to identify subpopulations of one molecule type with different diffusion patterns (three cases are shown in Figure 3.16a, top). According to equation (2.33), the diffusive behavior can be inferred from the anomalous exponent α. However, the common method of fitting MSD data in log-log plots with a linear regression to obtain the anomalous exponent α (Figure 3.16a, bottom) mostly fails in biological applications. The short track lengths in these types of experiments cannot provide enough data points to span several orders of magnitude to robustly fit such a power law. To date, no comprehensive method exists to reliably determine α, especially in live cell imaging that additionally introduces biological variance. Relative comparisons between samples might still be possible, but conclusions based on α values must be considered carefully. Even though the single particle tracks are difficult to analyze, they can provide deep insights into the molecular processes of living systems. According to the MSD plot in Figure 3.16a, one of the membrane proteins (black squares) shows Brownian motion. However, if its MSD is calculated within moving time frames along the particle track, the derived D values show a much more dynamic behavior (Figure 3.16b). This might, for instance, offer information on interaction events that take place during the observation of single molecules. In an sptPALM experiment, not only a molecule's spatial information, but also its intensity time trace is acquired. This points to a possible combination with FRET. When a molecule tagged with the FRET donor interacts with another molecule carrying the FRET acceptor, this would not only be visible in the drop of donor intensity, but also in its simultaneous diffusion pattern change. In the acceptor channel, a fluorescence spot should appear, copying the donor track during the time of interaction. Using automated analyses programs for a large number of particle tracks, it should be possible to find such interacting pairs, thus providing independent physical parameters for dynamic interactions in real time. This also demonstrates the potential benefits of such statistical evaluations for single particle tracing data, pointing to synergies with information sciences and mathematics. Performing most of the data evaluation on a customizable and widely used programming platform like MATLAB thus offers great potential for the development or implementation of new analysis techniques.

This chapter showed that, in addition to structural information obtained with dSTORM or SOFI, the broad spectroscopic capabilities of the microscope platform also allow for sptPALM experiments, as demonstrated by successfully reproducing data from a current research project. Furthermore, it validates sptPALM as a promising technique to address in vivo parameters of membrane molecules, which only recently proved to be applicable for complex analyses in plant systems [111]. Due to its synergy with other spectroscopic techniques like FRET, the addition of sptPALM holds great potential for a microscope platform targeting interdisciplinary research and method development.

3.6 Measurement of Nanoscopic Flow with A FRET-based Sensor

Can molecular mechanics be used to translate a macroscopic effect to the molecular level? The obvious advantage of such a successful translation would be the gain in resolution, as changes in molecular properties can be monitored or modeled on much smaller length scales than macroscopic parameters. Moreover, it is also very intriguing from a theoretical point of view: if the observed objects become sufficiently small, Newtonian mechanics are no longer applicable and must yield to a quantum mechanical approach. At which length scale are the effects predicted by each theory no longer negligible? Are there areas in which a mixed approach to a mechanical problem might be viable?

To come closer to answering these questions, first, a suitable model system must be found. The research project presented here deals with the sensing of dynamic pressures and currents at surfaces. An overview of the general concept and a feasibility study has already been published [113], therefore, only a brief summary of the original idea (compare Figure 3.17) will be given.

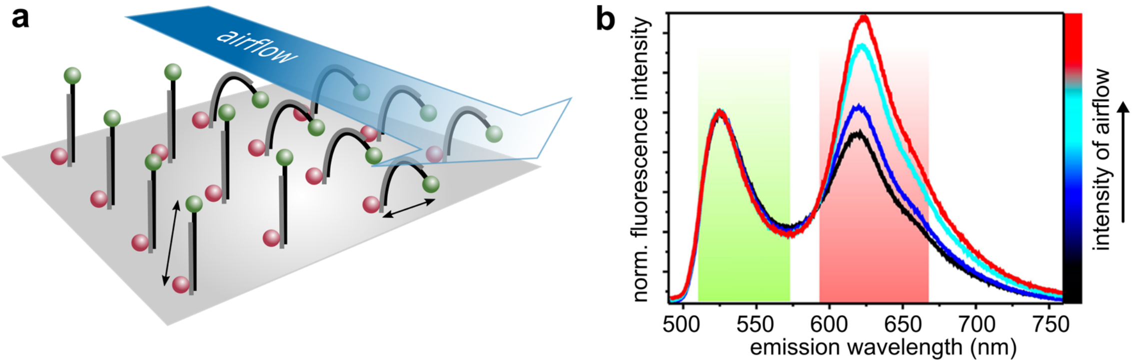

Figure 3.17 Functional principle of the molecular-mechanical pressure sensor. (a) Schematic representation of the sensor units. A suitable dye pair (green: donor, red: acceptor) is attached at a fixed distance to surface-anchored, double-stranded DNA. Airflow bends the DNA and thus changes the dye distance so that FRET is measurably increased (see length of double arrows). **(b)** The sensor response is read out via the relative intensity ratio of donor (green) and acceptor band (red). The larger the airflow, the higher the relative spectral content of the acceptor band (adapted from [113]).

3.6.1 Original Design

The original concept of the sensor can be illustrated by a wheat field on a stormy day. Wind or air pressure will bend the individual plant stems. By measuring the flexure of each stem as a function of impinging airflow, in theory, the force of the flow could be measured at each of these individual “sensors”. For a translation into the nanoscopic domain, an equivalent to these plant stems must be found, preferably linear molecular structures with suitable flexibility that can be covalently attached to a surface, standing up perpendicularly. Their curvature could be read out by measuring the distance between two points, for example between the top and bottom of the structure. A tool often used for the optical determination of nanoscopic distances is FRET. As this fluorescence-based method is highly sensitive, attaching a donor and acceptor dye to each molecular structure allows for monitoring interchromophoric distance changes down to subnanometer precision. These can then be back-translated to the curvature of the structure and the flow strength necessary to have caused the degree of bending. Since this technique is based on an optical readout, the spatial resolution to distinguish different areas of pressure is only limited by diffraction.

Before going into further details of the sensor, it is already evident that highly developed analytical methods are essential for its realization. The monitoring of the complete sensors main function under different environmental conditions, but also quality control of synthesis steps and the investigation of the precise sensor response mechanism place high demands on the spectroscopic equipment. Since the sensor is based on surface-bound fluorescent molecular structures, a fluorescence microscope with a wide range of spectroscopic techniques is the ideal choice. The microscope platform presented in this work provides both high-resolution imaging methods as well as techniques for the spectral and temporal analysis of FRET. Therefore, the project in this chapter also serves to underline that the development of novel measurement devices can greatly benefit from such expanded functionalities.

The sensor concept has obvious industrial applications, such as high-resolution measurements of aerodynamics in automotive and aviation engineering. Its utilization in biological research is also conceivable, for example to analyze water transport in the xylem tissue of plants.

A suitable molecular support structure that satisfies the abovementioned requirements is double-stranded DNA (dsDNA). It’s flexibility (Young’s modulus) is well researched, its surface chemistry established, and also modifiable with fluorescence dyes at almost every position with high accuracy. The original sensor design used partly hybridized dsDNA, placing donor (ATTO 488) and acceptor (ATTO 647) dyes at an initial distance of 8.8 nm. Figure 3.18 displays a short summary of the involved surface chemistry.

A custom-built air pressure nozzle with variable impinging angles was installed on top of the microscope's sample holder which firmly locked a sensor covered glass slide in place. The transparency of the substrate allowed for the assessment of the sensor response by the inverted objective from below. FRET efficiencies were calculated via the emission intensities of donor and acceptor in recorded fluorescence spectra. This enabled not only the basic characterization of surface coverage and average dye distance, but also the monitoring of dynamic FRET efficiency changes under airflow.

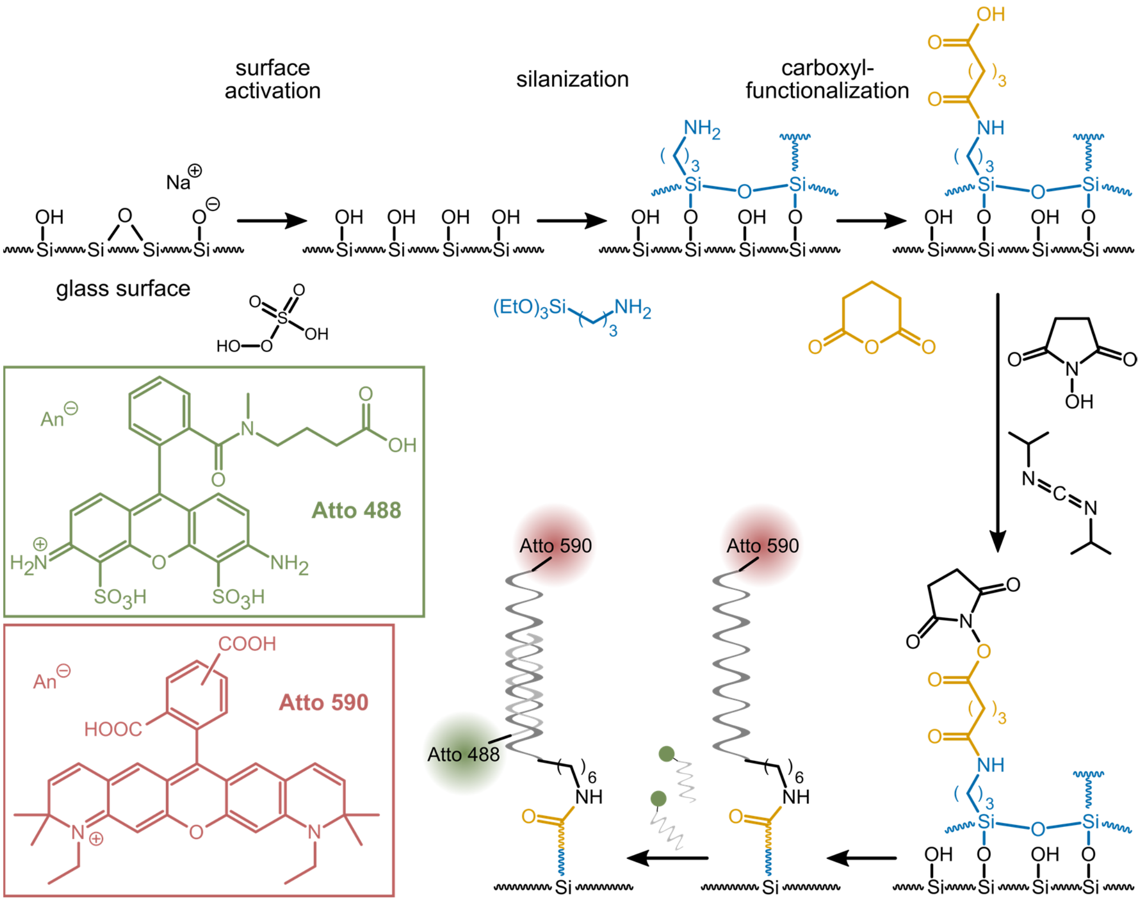

Figure 3.18 | Overview of the main synthesis steps of the original sensor design. After activation of the glass surface, silanization and carboxyl-functionalization, esterification with *N*-hydroxysuccinimide and *N,N'*-diisopropylcarbodiimide serves as a cross-linker to bind the acceptor-functionalized (ATTO 590) oligonucleotide to the surface. In a second step, the donor-functionalized (ATTO 488) oligonucleotide is added and hybridizes to its complementary DNA strand. Adapted from [113].

The proof-of-principle study showed very promising results. The FRET signal was shown to be dependent on both air pressure and the angle of incidence of the airflow. Molecular modifications to the sensor design apparently influenced its flexibility and therefore allowed to tune its functional range. Nevertheless, many properties of this novel sensor system and its precise mechanism were still unknown. Thus, it offered many interesting starting points for refinements, further development and the broadening of its application potential.

3.6.2 Additional Substrates

With regard to industrial applications, glass as a carrier material for the sensor is impractical. Polymer films, however, can be regarded as an ideal material. They are flexible and could therefore be applied to any shape or geometry, and they are readily modifiable by chemical means. Initial tests on poly(4-aminostyrene) with a spacer layer of polyethylene glycol served as proof-of-principle [114] for the attachment of the sensor on a plastic film (Figure 3.19).

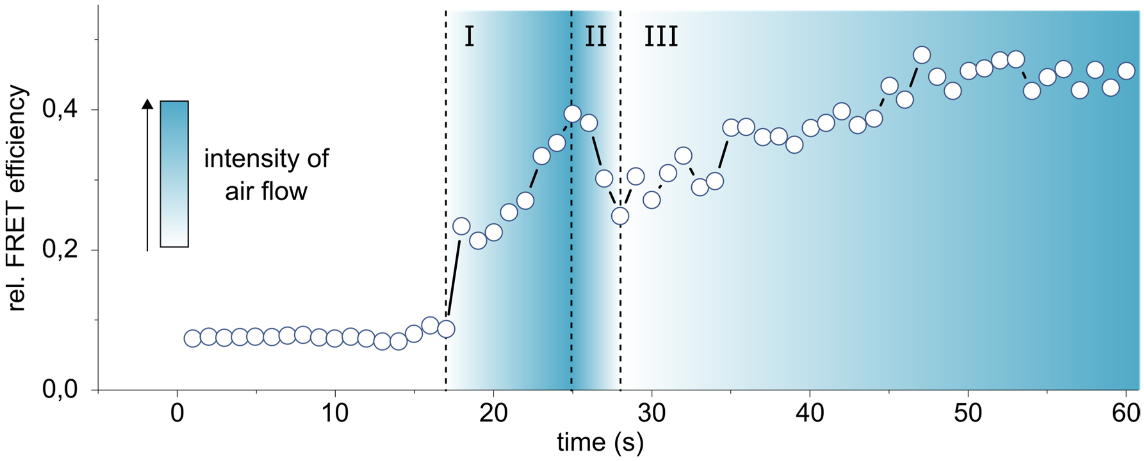

Figure 3.19 | Response of the sensor immobilized on poly(4-aminostyrene) as a function of the airflow intensity. Phase I shows a significant increase in FRET efficiency, which is only partially reversible with decreasing flow in phase II. Increasing the flow intensity in phase III again shows an increase in FRET efficiency. Adapted from [114]

Subsequent studies [115] looked into the choice of polymer with more detail. Polymers with free carboxyl or amine groups were preferred as they enable straightforward immobilization of terminally modified DNA. Key properties for the functional side are good plasticity, smoothness and low autofluorescence. During the synthesis process, low polymer swelling and high thermal stability are most important. Regarding upscaled applications, toxicity and price also have to be considered. After extensive research and tests [115], treatment of polyvinyl chloride with ammonia plasma resulted in a polymer fulfilling all of the above requirements. The dense surface functionalization could be demonstrated by successfully immobilizing organic dyes (Figure 3.20).

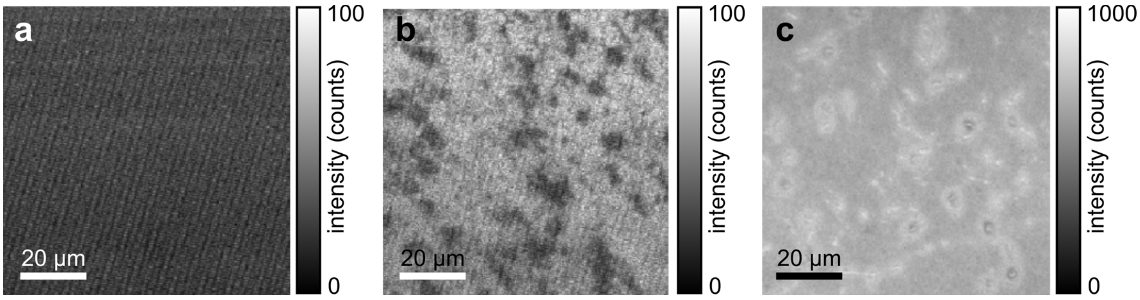

Figure 3.20 | Binding test of ATTO 488 dye on functionalized polyvinyl chloride (PVC). **(a)** Confocal fluorescence image of untreated PVC without addition of the dye (negative control). **(b)** Untreated PVC after the addition of carboxy-functionalized ATTO 488 in a coupling reaction. **(c)** As in **b**, but the PVC surface first underwent ammonia plasma treatment. Note the different intensity scale bar in comparison with **b**. All images were acquired with the same parameters. Adapted from [115].

Other carrier materials of interest are special stainless steels used for air plane models in wind tunnel tests. To achieve comparable results, downscaled models are furthermore often tested in pressurized, cryogenic wind tunnels, thereby readjusting the Reynolds number (ratio of inertial to viscous forces of the working fluid). While the temperature stability and thiol-coupling of the sensor to silver metal films could be shown [114], corresponding options for stainless steel substrates are still pending. An interesting electrochemical approach involves the passivation of steel surfaces to introduce modifiable hydroxyl groups. Using cyclic voltammetry as a monitoring tool to control this process showed promising results in initial experiments.

3.6.3 Additional Working Fluids

In addition to air currents, denser media were also explored as working fluids for the flow sensor. This would not only widen the scope of possible applications, but also provide a much more controlled environment. In comparison with gases, the higher density of liquids enables them to exert similar forces with lower velocities. This makes it much easier to ensure stable laminar flows and suppress chaotic turbulences.

The analysis of sensor dynamics in a buffered solution also provides a much more natural environment for DNA. Moreover, the intended mathematical modeling of the sensor response relies on property constants to simulate the system. Considering that most published physical properties for DNA were measured in its natural environment, buffered solutions allow for more congruency between model and experiment.

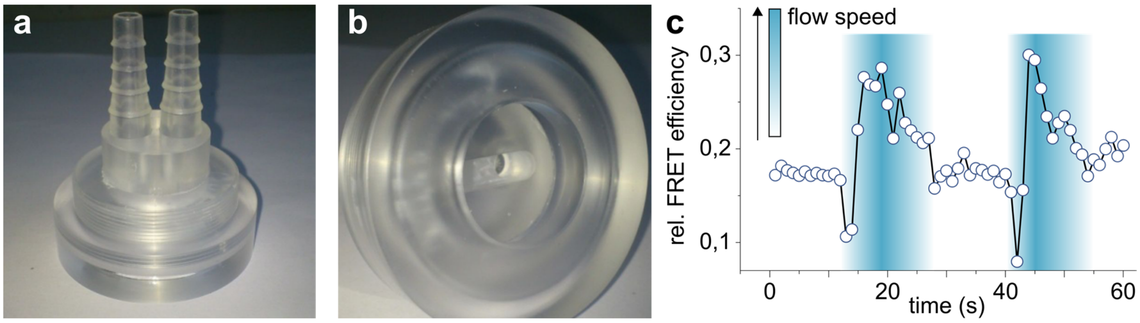

Figure 3.21 | Sensor dynamics in fluids. (a) Flow cell (diameter approx. 25 mm) with inlet and outlet connectors, designed as an attachment for an inverted fluorescence microscope. **(b)** Bottom view; a round coverslip can be locked and sealed here so that attached sensor units are exposed to a 5 mm wide flow channel. **(c)** Sensor response in the flow channel with water as a fluid medium. The FRET efficiency correlates significantly with the applied flow rate. Adapted from [114].

To this end, a basic flow cell was designed to fit on the microscope sample stage [114]. Several measurement series demonstrated the effectiveness of the sensor in liquid media (Figure 3.21), offering possible applications in microfluidic devices.

Further measurements [116] showed that, depending on the working fluid, the static interchromophoric distances differed significantly. As dehydration of dsDNA drives it from the B- to the A-conformation, the helix geometry and base pair distances are changed. This has to be considered when the sensor response is analyzed in different media.

For subsequent experiments [115], an advanced version of the flow cell was acquired that also enabled different flow geometries (Figure 3.22). This was achieved by using a polydimethylsiloxane stamp on which the flow channel was printed as an elevated structure. By pressing down the stamp onto the glass substrate, the flow channel seals itself and allows a constant fluid current via embedded in- and outlet ports. The exchangeable stamp affords maximal flexibility, for example by shaping the width and height of the flow channel, different current speeds can by realized. Moreover, curved paths or obstacles could be introduced to observe their influence on local flow patterns.

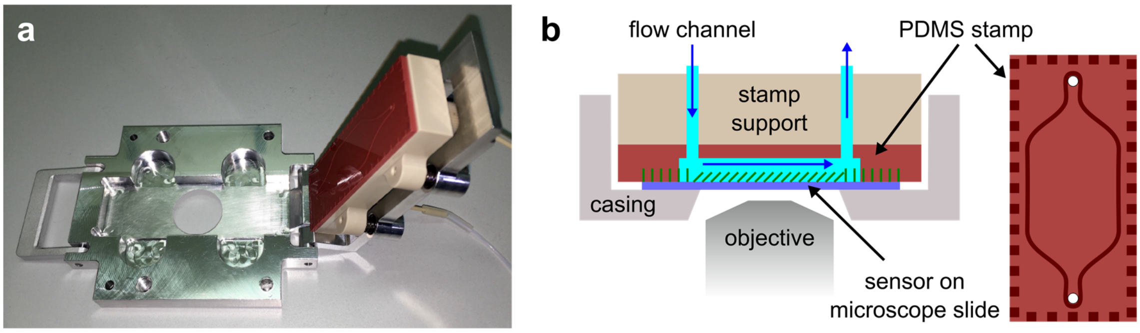

Figure 3.22 | Further development of the flow cell. (a) Top view of the housing (that can be screwed to the microscope sample table) and the flipped-up stamp (on the right) showing the inlet and outlet hoses. **(b)** Schematic structure of the flow cell (not to scale). The polydimethylsiloxane (PDMS) stamp (red) can be imprinted with any structure (right, dark red). In this case, the large width of the flow channel favors a laminar flow profile. The bordering squares provide a stress-free base for the sensor support (microscope slides). Adapted from [115].

3.6.4 Chemical Synthesis and Design Overhauls

The original publication focused on demonstrating the general functionality of the sensor. The scope must now be extended to analyze if the initial theoretical model truly reflects the sensor response in practice. In other words: does the resulting signal represent an average value of different processes or does each sensor unit contribute to the overall signal in the same, defined way? Only the latter case allows for an evaluation of the mechanical properties according to the model, therefore the structure of the sensor units must be exactly known and controlled. To this end, the surface chemistry was first reexamined to improve reproducibility (Figure 3.23). Surface synthesis steps were reduced to minimize experimental variabilities (compare with bottom row of Figure 3.18).

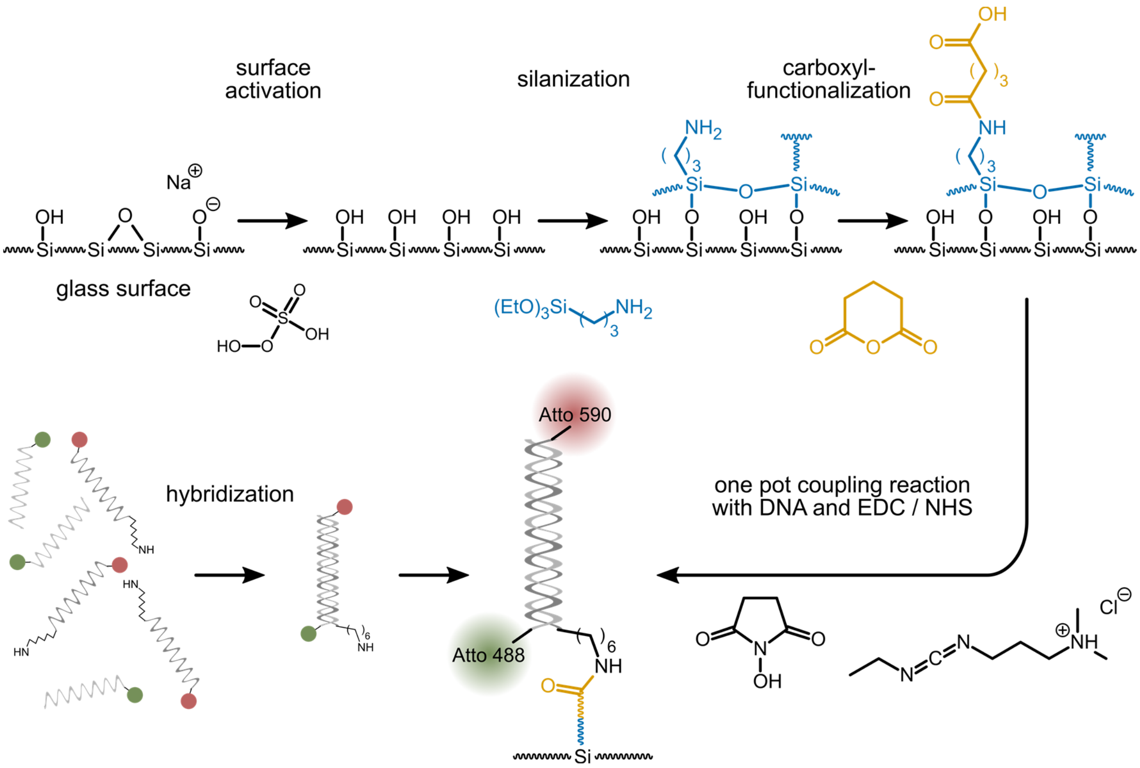

Figure 3.23 | Further development of the sensor surface chemistry. Using water-soluble coupling reagents, amine-modified double-stranded DNA can react directly with the in situ generated active esters on the surface. The preceding DNA hybridization step ensures that only complete sensor units are attached.

The greatest difference concerns the immobilization of DNA on the surface. As the original synthesis scheme derives from ligand binding assays, it involves an immobilized capture probe (single-stranded DNA [ssDNA]) that hybridizes with a ligand (the complementary DNA strand) in the analyte solution. This introduces incomplete hybridizations, thus leaving behind single-stranded DNA which only carries the acceptor dye. Furthermore, surface chemistry tends to be rather complex due to adsorption effects and reduced degrees of freedom. An excess of donor labeled DNA might therefore only lead to more unspecific binding instead of higher hybridization. This problem can be solved if the DNA hybridization is performed prior to immobilization. Temperature controlled DNA annealing in special buffer solutions is extensively used in molecular biology, often yielding virtually 100% hybridization, in particular for relative short DNA fragments as used in this project. This ensures that only complete sensor units are bound to the surface. As the immobilization is performed at room temperature with stable dsDNA, this further suppresses possible undesired side reactions with surface molecules.

In a further project step, the sensor design was reconsidered. In the original concept (Figure 3.24a-c), the donor is situated directly at the surface. It cannot be ruled out that this might have adverse effects on the fluorophore, for example, by collisional quenching and electrostatic interactions. Furthermore, the no-slip condition for viscous fluids predicts that the flow velocity at the surface will be zero. It should be pointed out, however, that it is unclear if classical fluid mechanics can be applied to the molecular level. In any case, a greater distance of the FRET dyes from the surface would be advantageous, removing these uncertainties. These considerations resulted in a new sensor design, featuring a hybridized dsDNA stem protruding from the surface, while two flexible ssDNA arms (their base pairs chosen to prevent hybridization) carry the FRET dyes (Figure 3.24d).

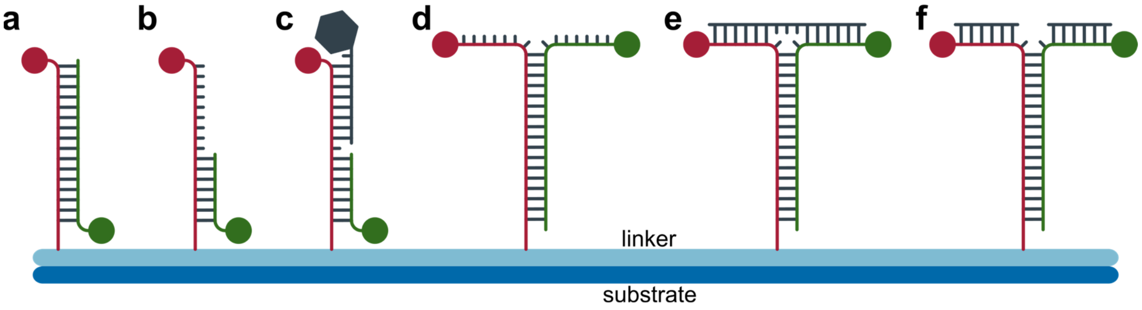

Figure 3.24 | Alternative sensor geometries. The acceptor (red) DNA strand is attached to the substrate (blue) via a chemical linker (light blue) and hybridizes to the donor (green) DNA strand, respectively. **(a)** Original design. **(b)** Incomplete hybridization to increase flexibility / sensitivity. **(c)** Hybridization of a third DNA strand to structure **b** allows the use of molecular structures (gray) to increase the available contact surface of the sensor. **(d)** Novel T-structured design to elevate the chromophores from the surface. **(e)** A third DNA strand (gray) is used as a bridge to fix the initial configuration. **(f)** Disruption of the bridge, introducing a molecular hinge.

In case of an impinging force, the initially randomly oriented arms would align in the same direction, bringing the FRET pair much closer together. However, in contrast to the defined tertiary structure of dsDNA, the random configuration of ssDNA is unsuitable for a predictable model. In consequence, a sensor design with full hybridization was devised by introducing a third strand to form a T-shaped structure. To influence flexibility, the removal of single base pairs can introduce a hinge of adjustable rigidity (Figure 3.24e,f).

3.6.5 Structural optimization

Another source of uncertainty was the attachment linker to the surface. At molecular length scales, Coulomb forces should provide enough repulsion so that the negatively charged dsDNA points perpendicularly away from the negative surface charges. It is however hard to estimate if this also holds true for strong surface flows. Instead of, or in addition to bending, the entire structure might just tip over to one side. A macroscopic approach for this problem would be a tripod linker at the base, but this would require multiple attachment points and therefore technically demanding modifications for the dsDNA. Here, the solution was found by applying DNA origami [117]. This technique utilizes the high interaction specificity of deliberately assembled base pair sequences to create two- and three-dimensional, self-assembling nanoscale shapes. These structures can be built with high stability. In one study [118], DNA origami was used to construct a tower-like support structure to control the spacing between two nanoparticles while elevating them high above the surface. This inspired a novel, very stable design for the sensor, featuring four chemical anchor points to fix the structure base to the surface (Figure 3.25a,b).

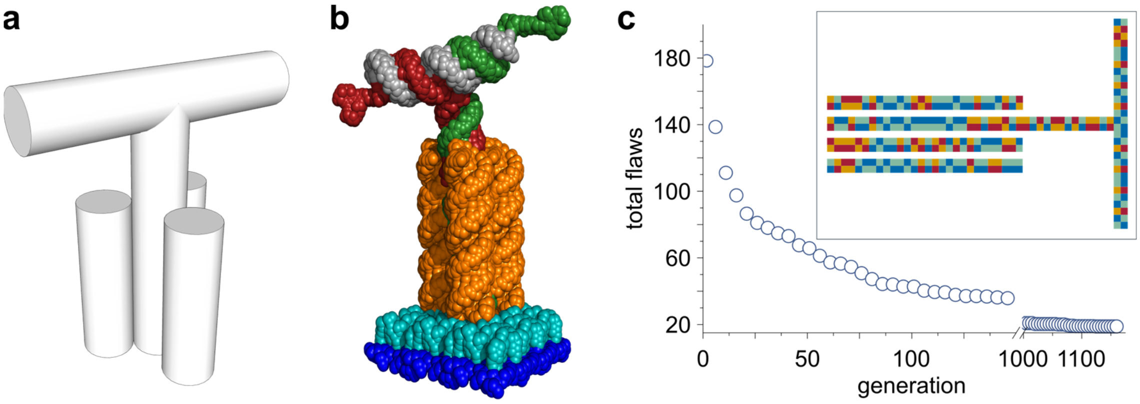

Figure 3.25 | Design and calculation of optimized DNA origami structures. (a) 3D concept drawing, each column represents a folded dsDNA sequence. The columns are cross-linked to each other and all vertical columns can be anchored to the surface. **(b)** Modeled molecular structure of a DNA origami sensor unit with substrate (blue), chemical linker layer (light blue), support structures (orange), donor (green) DNA strand, acceptor (red) DNA strand, and horizontal bridging DNA (gray). **(c)** Sequence optimization of the single strands for maximum hybridization efficiency. The folding flaws initially decrease rapidly for each calculated generation and approach a low error plateau. The inset shows the color-coded distribution of the four nucleobases in the optimized structure.

Usually, DNA origami uses one long (typically bacterial) DNA strand, and then small synthesized staple strands fold the longer strand into the desired shape. Depending on the size of the structure, the annealing procedure can take up to days and might also show varying degrees of mismatches. As the sensor is a comparatively small structure with nine DNA strands of small lengths ranging from 14 to 42 base pairs, this offered the possibility to deliberately design every DNA strand to maximize the hybridization efficiency of the final structure with a computational approach.

To ensure the highest yield of correctly folded sensors, the strands must have following properties: a) the base pairing must always be correct; and b) no hairpin structures of single strands, c) no self-hybridization of single strands and d) no false hybridizations between strands must take place. While not necessarily leading to misfolded structures, the more possibilities for alternative structures exist, the longer the annealing procedure will take. The probability of such mismatches was assessed by calculating their hybridization enthalpies in comparison to the desired structure. This was possible because the hybridization enthalpy of two DNA sequences can be estimated by adding the fractional enthalpies for each base pairing, slightly modified by their neighboring base pairs and their position in the sequence [119]. Consequently, all possible self-hybridizations (including hairpin structures) for each of the nine single strands and also all possible 36 combinations of different strands had to be calculated. The ratio of added mismatch enthalpies to the desired structure enthalpy had then to be minimized by the exchange of base pairs. As every change in one strand is interconnected to other strands, it was quickly evident that this optimization problem could not be solved by a simple least squares regression.

Therefore, an evolutionary algorithm was programmed in MATLAB. As a starting point, all strands had random base pair sequences that were adjusted to ensure correct base pairings (AT, TA, CG or GC) in the target structure. This strand package was copied 20 times (constituting a population of 20). Nucleotides in all strands were mutated with a specified probability, always making sure that the corresponding bases were changed accordingly. This represented a population of 20 mutants (the first generation). All strands for one mutant were analyzed and significantly undesired hybridizations were added up to a total flaw count for each mutant. Some of the random mutations would lead to higher, some to lower flaw counts. In natural selection, those individuals in a population which are best adapted to their environment will gain a reproductive advantage. In the program, this environmental pressure was exerted by only allowing the mutant with the least flaws to “procreate”. This package of DNA strands was then copied and mutated again, constituting the second generation. It then went through the above process again to generate the third generation, and so on. This method proved to be highly effective in quickly optimizing the origami sequences to reduce undesired hybridizations, allowing fast and correct folding of the structure (Figure 3.25c). The bigger the structure, the longer the calculation time, and some base level of flaws may still remain. However, at that point, thermodynamics will strongly favor folding into the correct structure. This optimization should lead to more clearly defined structural features such as the geometry of the sensor and its orientation to the surface.

3.6.6 Mathematical Modeling

An important step for the complete description of the sensor is the comparison of the sensor response with a theoretical, simulated model. As mentioned above, the sensor was designed on the basis of classical mechanics, translated to a molecular system. Therefore, it made sense to first build a mathematical model based on Newtonian mechanics. Such a model would also have the advantage that modifications in sensor geometry, environmental conditions or substrates could be simulated. On one hand, this could reveal which design aspects are critical for specified conditions or allow for a preselection of promising new molecular geometries. On the other hand, the experimentally determined sensor response could also serve to refine the mathematical model.

The following approach was developed by Alexander Stuhl, who utilized continuum mechanics and the representation of the sensor as a geometric body with a continuously distributed mass, while obeying the conservation laws of mass, linear momentum, angular momentum and energy. These quantities were expressed with regard to the mass continuum in the form of integrals, from which differential equations could be derived. Together with equations describing the material behavior (including material constants like dsDNA flexibility, given by its Young's modulus), equations for linear elasticity or fluid mechanics were obtained. The introduction of boundary conditions of the physical process (in this case a directed surface pressure on the sensor caused by a flow) then completed the mathematical description of the model sensor. The partial differential equations used here are usually solved and visualized with approximative numerical methods. In this project the finite element method was used, which was realized by the software SfePy (Simple Finite Elements in Python). In future project stages, the simulated model will enable quantitative evaluations of the molecular-mechanical sensor.

The present system can also be used to explore a much more fundamental question. While quantum mechanics and classical mechanics are usually described with fundamentally different formalisms, the sensor is a mechanical system that, due to its molecular size, works in a not yet adequately defined area between these worlds. By adapting the mathematical model and comparing it with experimental data, it may be possible to determine at which point quantum mechanical effects become dominant or whether entirely new formalisms have to be developed.

3.6.7 Further development and other interdisciplinary approaches

This project served as an example of how the knowledge and methods of various research disciplines can be combined: the physical process of fluid dynamics on a surface was sensed with the help of chemically modified biological molecules, their structure optimized with a computational approach and simulated with a mathematical model. It also showed the synergy of such a project with interdisciplinary spectromicroscopy techniques for visualizing the sensor response, quality control of synthesis steps and the analysis of molecular mechanics. The large variety of supporting spectroscopic methods greatly benefitted the demonstrated advancements in the design and characterization of the flow sensor.

In continuation of the ongoing work presented here, better control of structure and function of the sensor could provide a basis for the conception of comparable in vivo sensors that could measure fluid flows in living organisms. Further work has to be done to enable comparisons and bidirectional improvements of the experimental side and discrete mathematical modeling. This will not only be a major step toward the realization of wider sensor applications, but could also grant deeper insights into the links between classical and quantum mechanics.

In contrast to the other studies presented in this work, this project in particular extended well beyond life sciences, for example, by imaging chemically altered surfaces with confocal fluorescence microscopy or by monitoring the hybridization of labeled DNA with FLIM-FRET in solution. These useful techniques to analyze (surface) chemistry were readily available due to the selection and flexibility of the spectroscopic equipment.

This advantage also enabled collaborations with research groups from other disciplines. In the field of chemistry and basic research, one study investigated the photophysics of hemiporphycenes [120]. Another study from physics and materials science addressed changes in the optical properties of quantum dots near plasmonic structures [121]. In both cases, the researchers' access to time resolved fluorescence spectroscopy with single-molecule sensitivity resulted in important contributions to their respective projects.

Conversely, valuable experience is gained from sample analysis and the general approach of other scientific disciplines. This is important for the development of new analytical methods. As this chapter demonstrated, a broad range of spectroscopic capabilities as well as experience and skill in different research areas are key for interdisciplinary projects.

4 Design and Construction of an Interdisciplinary Microscope Platform

The aforementioned publications were used as validation for the selected spectromicroscopy techniques and underline their relevance in current scientific questions. Due to the diversity of the experiments, reaching into different research fields, this also allowed an overview of general requirements for the design of a suitable microscope. Conceptual considerations for the design are therefore presented in the following and were incorporated into the custom-built microscope, which is described in-depth in chapter 4.2, including hardware and software control.

4.1 General Considerations

Stability and modifiability: The optical setup should be generally constructed with careful attention to stability and robustness to ensure measurements that are isolated from vibrations originating from the laboratory building or other external influences. Moreover, all installed parts, especially support structures and optical path assemblies should use common and widely available components and materials to allow for the easy replacement or modification of existing setup design elements.

Sample holder: The hemisphere above the sample table should be designed accessible so that not only different sample formats (cover glasses, microscope slides, microwell plates, etc.) can be measured, but also, for example, opaque or inorganic samples. Experiment-specific attachments such as a gas supply, temperature control or illuminators for sample pretreatment with light should be easily implemented without being restricted by the lack of space.

Excitation modes: The broad spectrum of fluorescence labels in biological research requires a correspondingly large selection of available laser wavelengths. For many techniques, such as FLIM and FIDSAM, pulsed lasers are also a prerequisite. Moreover, some methods also require fast switching between several laser lines. Different excitation modes (wide field, TIRF, confocal, polarized, etc.) must also be supported and be easily interchanged.

Scanning and focusing: In most commercial raster imaging applications, the excitation laser beam is steered over the stationary sample by a system of electrically actuated mirrors (for example in confocal laser scanning microscopy [CLSM]). Here, however, a 3-axis piezo sample scanner will be used, whose comparatively slow scan speed is outweighed by several significant advantages. As the laser beam position is fixed, this allows for more precision in applications with high demands on stable focus geometries. Moreover, piezo sample stages provide very high and uniform positioning accuracy that might not be achievable by beam scanning. The utilization of the piezo table's *z*-axis also allows for precise optical sectioning without moving other focusing optics, thus further improving the stability and robustness of this system. For wide-range *z*-scanning and focusing, a separate piezo motor controls the position of the microscope objective, also providing the basis for other technical supplements like focus stabilization.

Multichannel detection and parallelization: Using a common excitation beam path and suitable filters and beam splitters, distinguishable fluorophores in the sample should be excited and detected separately in accordance with their spectral properties. Parallel or sequential sample measurements enable the representation of data as multimodal images. As living biological samples are prone to movement and jittering, a parallel acquisition is preferable for a spatially consistent overlay of different spectroscopic data.

Diverse readout methods: The analysis of different research questions requires a versatile and comprehensive detection module. This includes efficient detectors for confocal measurements, as well as electronics and detectors for time-correlated single photon counting, high-resolution imaging spectrographs and fast, low-noise EMCCD or CMOS cameras.

Flexible design: If possible, the analysis method should always be adapted to the scientific question and the available sample material. This is only possible if the excitation and detection modules are accessible, exchangeable or switchable. In this way, new developments in spectroscopic techniques can be quickly implemented.

4.2 Assembly of the Spectromicroscopy Platform

4.2.1 Design Fundamentals

To protect the optical setup from vibrations that are most prominent in buildings and especially research laboratories, the base plate of the setup consists of a heavy optical table with high thermal stability, which is supported by four isolation legs. To provide an air cushion that uncouples floor vibrations from the table, the legs are either passively pumped up or constantly adjusted with a connected pressured air source. In particular for live cell imaging techniques, small vibrations are widely exceeded by innate sample movements. For the studies presented here, a passively pumped system thus proved entirely sufficient. Casings and diverse structural elements were produced in the Central Chemical Institute's metal workshop, while most optical and optomechanical components were purchased from the companies Thorlabs (Newton, USA) and Qioptiq (Excelitas Technologies Corp., Waltham, USA), offering widely available products that are furthermore often interchangeable. Their 30 mm cage systems were used throughout for their easy implementation and compatibility. In principle, they allow a beam path height of 40 mm above the table, which is ideal considering stability and robustness. However, at this height, the adjustment screws of some optomechanical elements are difficult to access. Therefore, small aluminum blocks were produced to raise the overall beam path to a more practical height of 50 mm. All components on the optical table are grouped into several modules and encased in custom-made black plastic boxes with removable tops (Figure 4.1), while laser and emission light can pass through small holes between the modules.

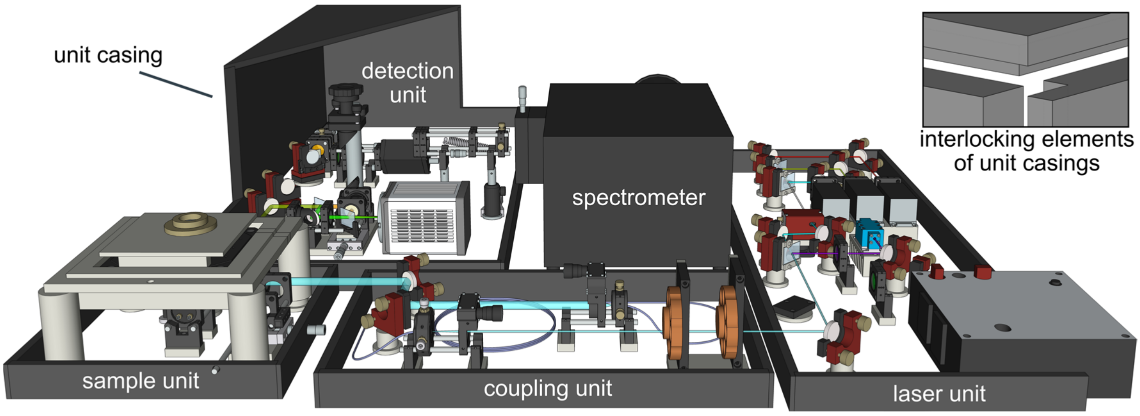

Figure 4.1 | Assembly overview of the custom-built microscope. Each unit is enclosed by a casing with a removable top panel, here partly shown for the detection unit, otherwise indicated by black boundaries. Clearance holes allow the excitation or emission light to traverse the different units. All casings are designed with interlocking elements (top right inset), thus light-proofing their junctions.

On one hand, this is a measure of laser safety, on the other hand this prevents laboratory or laser excitation stray light from reaching the detectors. For further reference in the following text and figures, a schematic overview of the research microscope is given in Figure 4.2. Details of all described components can be found in Table 4 in the appendix.

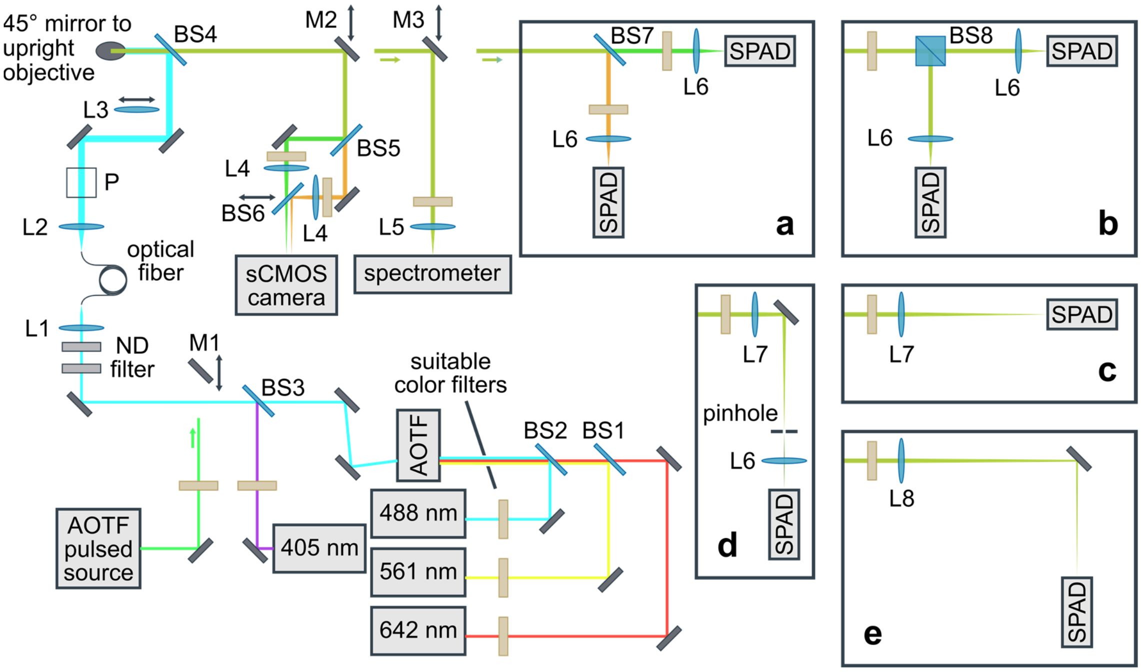

Figure 4.2 | Compact schematic overview of the research microscope. For a detailed description and references to numbered items like lenses (L), beam splitters (BS) and mirrors (M) see text in the following chapters, also for the different confocal configurations depicted in insets (a-e). Abbreviations: Acousto-optical tunable filter (AOTF), neutral density filter (ND filter), sCMOS (scientific complementary metal-oxide-semiconductor) camera, single-photon avalanche diode (SPAD). The box P in the beam path denotes the position for additional elements, such as polarization optics.

4.2.2 Laser Unit

Compare Figure 4.3 for an illustration of the laser beam path layout. To comply with the wide range of spectral requirements for fluorophore excitation, a supercontinuum pulsed laser source is implemented that can be used for all applications that need comparably low excitation intensities, for example FLIM or FCS measurements. The accompanying acousto-optical tunable filter (AOTF) allows for the free selection of up to eight laser lines from 400 to 675 nm, which can be used separately as well as in any combination with typically 1 mW output power each. The wide range of available repetition pulse rates between 2 and 78 MHz is ideal to capture fluorescence decay curves in time frames between 500 and 12.5 ns, respectively. Due to repetition rates in the MHz regime, the laser can practically be considered as a continuous wave (CW) laser and therefore used in many other applications. In the illustrated laser layout, this beam path can be accessed by placing mirror M1 on the magnetic platform (Figure 4.3). These removable magnetic holders are used throughout this optical setup as they offer excellent position stability and are also more suitable for long-term use than flip mounts.

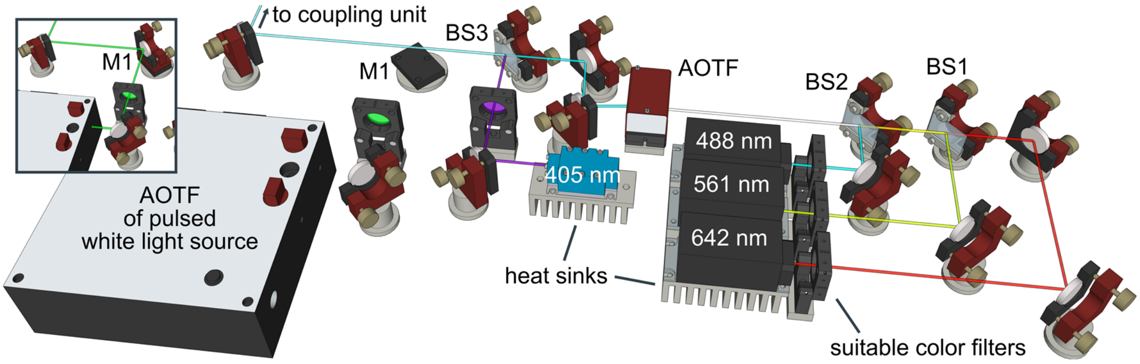

Figure 4.3 | Laser unit layout. Pulsed laser excitation is selected by placing mirror M1 on the magnetic base plate (see inset), using the AOTF of the pulsed white light source to choose up to eight wavelength outputs. For CW excitation, four laser heads are available (405 nm, 488 nm, 561 nm, 642 nm), equipped with heat sinks for thermal management and height adjustment. After passing suitable clean-up color filters, the three lasers on the right are steered to a common beam path with mirrors and dichroic beam splitters BS1 and BS2. The following AOTF is fixed on a rotational stage (not visible here) for fine adjustment.

A second output of the AOTF supplies an alternative excitation spectral range from 670 to 1100 nm, therefore also allowing access to spectromicroscopy in the near infrared. Experience has shown that the AOTF often produces additional broad spectral sidebands in addition to the selected laser line, so laser clean-up filters are advisable after the AOTF output. The AOTF can also be quickly removed in favor of installing other laser modules. Two mirrors compensate for the angular displacement of the selected laser beams. They are then joined with the 405 nm laser by beam splitter BS3 and finally directed to the coupling unit.

TIRFM applications, especially for single-molecule localization superresolution microscopy requires a set of different laser lines with output intensities of typically higher than 50 mW. To this end, four different CW lasers are implemented in the main excitation path: 488 nm, 561 nm and 642 nm imaging laser modules cover the most common range of available and utilized fluorophores. Aluminum cooling fins serve both as height adjustment and heat sinks, providing thermal management for all installed laser modules with a maximum power of 120 mW.

Each laser beam passes a suitable clean-up color filter and can be adjusted with two mirrors or dichroic beam splitters (BS1, BS2). All optic mounts feature two adjustable axes to precisely align all lasers to one common beam path that enters a computer-controlled AOTF that is fixed on a rotation state for further adjustment. The AOTF provides convenient control over laser intensities, combinations of the aforementioned laser lines and rapid switching between them in the millisecond regime. Beams of selected laser wavelengths exit under the Bragg diffraction angle and are straightened by two additional steering mirrors. Subsequently, beam splitter BS3 joins the imaging laser path with the 405 nm laser module that did not enter the AOTF for a practical reason: due to the large difference between the shortwave 405 nm laser and the longwave imaging lasers, even achromatic optics cannot always compensate for dispersion effects introduced by the focusing elements. As the 405 nm laser is used only as a low intensity activation laser, it is appropriate to primarily adjust the setup for the imaging lasers. The separately adjustable activation laser therefore reduces the alignment complexity, while still delivering enough laser power. In the end, all four CW lasers can be controlled by the same software control interface. While the fast switching of laser lines is in principle also possible by programmatically addressing each laser module, frequent changes between the ‘on’ and ‘off’ status or different power settings can introduce inconsistent laser profiles. For better stability, it is therefore advisable to operate the imaging laser modules at a set intensity and leave the switching and intensity adjustment to the AOTF.

4.2.3 Coupling Unit

Two intensity attenuation filter wheels provide additional intensity control of the lasers before they are coupled into a single mode fiber with achromatic lens L1 (Figure 4.4) as a convenient method to produce uniform, spatially cleaned-up Gaussian laser profiles. As the fiber output is fixed, this approach also simplifies the introduction of other laser modules without affecting the downstream beam path, for example by replacing the supercontinuum AOTF. By using patch cables, the optical fiber can also be quickly exchanged with polarization maintaining or multimode fibers.

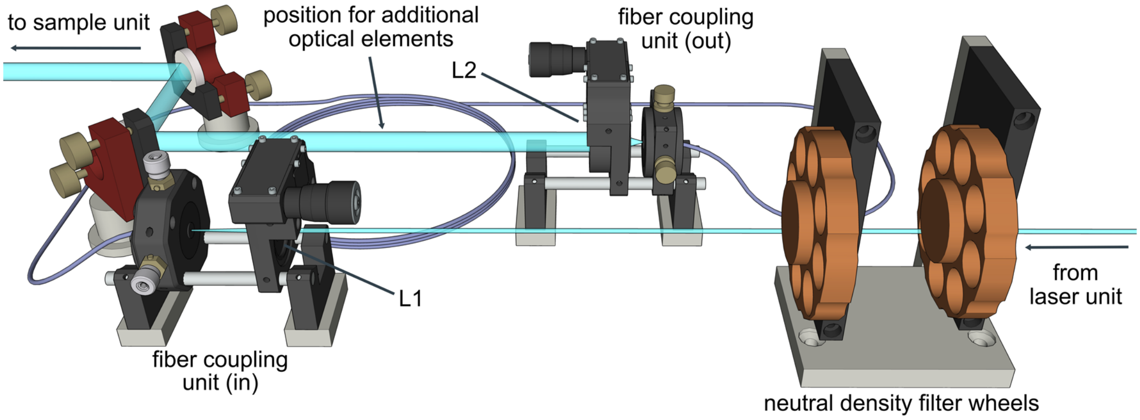

Figure 4.4 | Coupling unit layout. The beam from the laser unit (right) first passes two neutral density filter wheels for additional intensity adjustment. Achromatic lenses L1 and L2 are part of a single mode fiber coupling system and can be fine adjusted along z, while the fiber connectors can be adjustment in *x* and *y*. Afterward, all lasers show clean Gaussian profiles and are perfectly aligned with respect to each other. The focal length of L2 is chosen to result in a beam diameter of 10 mm. Additional optical elements can be introduced in the following free space, before two steering mirrors direct the beam to the sample unit (left).

Fiber de-coupling is achieved with achromatic lens L2 that collimates the excitation beam to a diameter of 10 mm. Subsequently, additional optical elements like linear polarizers and/or retardation plates can be introduced (also compare Figure 4.2, box P), before the beam is steered to the excitation/emission beam splitter via two adjustment mirrors.

It is important that the laser intensity can be attenuated prior to the fiber coupling, as this ensures that the neutral density filters have no influence on the final beam profile. As an alternative to discrete damping steps, the filter wheels can be replaced by a continuously displaceable laser blocker. Pushed into the beam path, for example, by means of a micrometer screw, the laser intensity coupled into the fiber can then be controlled gradually, also without changing the beam profile at the fiber output.

4.2.4 Sample Unit

The main component is shown in Figure 4.5a and hold the microscope objective, the piezo table and the sample stage and was manufactured in the metal work shop. The comparably heavy frame for the piezo table, sturdy aluminum legs and its compact design are chosen to provide additional vibrational stability. The sample stage is an aluminum plate mounted onto the piezo table with a round recess for the objective (see Figure 4.5b). In its simplest form, a biological sample is sandwiched between two round coverslips placed on a flat brass ring and lightly weighed down by a smaller brass ring for stability. By manually moving the lower ring, the user can coarsely navigate to a region of interest in the sample while fine tuning the position via the piezo table. This simplistic design allows for a wide range of sample formats (cover glasses, microscope slides, microwell plates, etc.) but also, for example, opaque or inorganic samples. By focusing into a small fluid droplet on a glass slide, many spectrally or time-resolved methods can also be performed in solution using very small sample volumes.

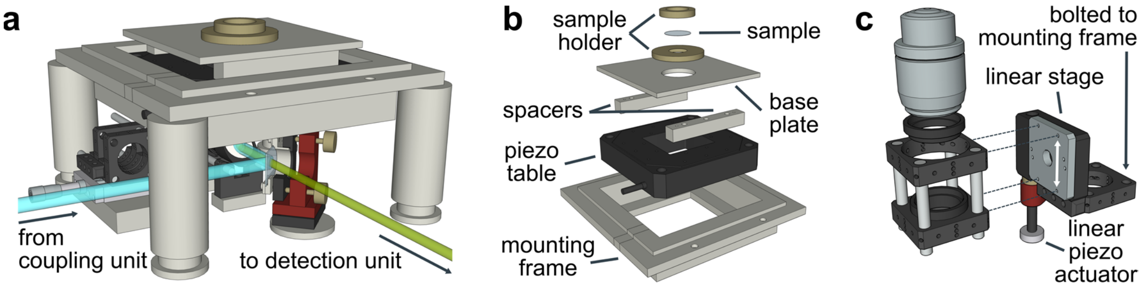

Figure 4.5 | Sample unit layout. (a) Assembled sample stage, for a better view of the beam path see Figure 4.6. **(b)** Exploded view of the sample stage components. **(c)** Design of the microscope objective focusing mechanics, using a linear piezo actuator to move the objective up and down.

Experiment-specific attachments such as a gas supply or other accessories can be easily implemented as well as motorized solutions for coarse sample movement. The comparably small lateral movement range of the piezo table (limited to 160 µm in the utilized software) might appear cumbersome when searching for interesting structures in a sample, but from experimental experience, this positioning method is sufficient for most samples. Moreover, the here presented microscope is not primarily designed for high-throughput, routine measurements but for specialized techniques with high precision, at the same time providing high versatility in the experimental setup.

The attached objective mount (see Figure 4.5c) can be moved up and down by a computer-controlled linear actuator. Its large movement range of 2.5 cm is beneficial for focusing with differently dimensioned microscope objectives while its small increment steps of 30 nm allow for fine tuning and, for example, its implementation in focus stabilization feedback loops.

When the excitation beam enters the sample stage from the coupling unit, an *xyz*-adjustable lens L3 can be pushed into the beam path, which focuses on the back focal plane of the microscope objective, thus allowing switching between either confocal (see

Figure 4.6a) or epi-fluorescence, TIRFM and VAEM illumination (see Figure 4.6b). As the second set of options is featured in superresolution experiments with comparably high laser powers, it is important to note that lens L3 should be manufactured from fused silica, as other lens materials can show significant auto-fluorescence under these conditions.

The here most frequently used beam splitter BS4 is a quad line beam splitter, reflecting 405 nm, 488 nm, 561 nm and 642 nm, covering the most common excitation wavelengths. It is installed on a magnetic platform to facilitate its replacement for experiments requiring other laser lines. The laser beam is then redirected by a 45-degree mirror to the upright microscope objective.

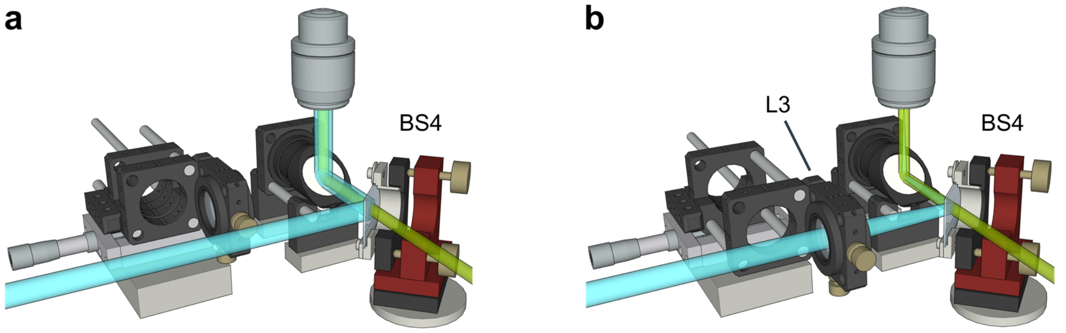

Figure 4.6 | Beam path of the sample unit. (a) In confocal illumination mode, the collimated beam (blue) is directed by the beam splitter BS4 and the 45° mirror to the upright microscope objective that focuses the beam on the sample. The emission signal (green) is collected by the same objective and passes though the beam splitter to the detector unit. **(b)** In wide-field illumination mode, lens L3 is pushed into the beam path to focus on the microscope objective's back focal plane, using the linear table as fine adjustment. Lateral beam displacement for total internal reflection illumination and variable angle epi-fluorescence illumination can be controlled with the adjustment screws of the lens holder.

When the excitation beam enters the objective, its large diameter of 10 mm is designed to overfill the back aperture to take full advantage of the numerical aperture, thus optimizing the achievable resolution in confocal measurements. This is also beneficial in wide-field experiments, as only using the center part of the Gaussian beam provides a more uniform illumination. However, the loss of intensity must always be considered, as this can be a limiting factor in single-molecule localization techniques. In these cases, a different fiber de-coupling lens L2 can be used to adjust the laser diameter.

4.2.5 Detection Unit

Sample fluorescence is collected by the microscope objective and passes the beam splitter to enter the detection module (see Fig. 49). Here, light from the main emission beam path can be redirected via removable mirrors M2 and M3 to the individual detectors.

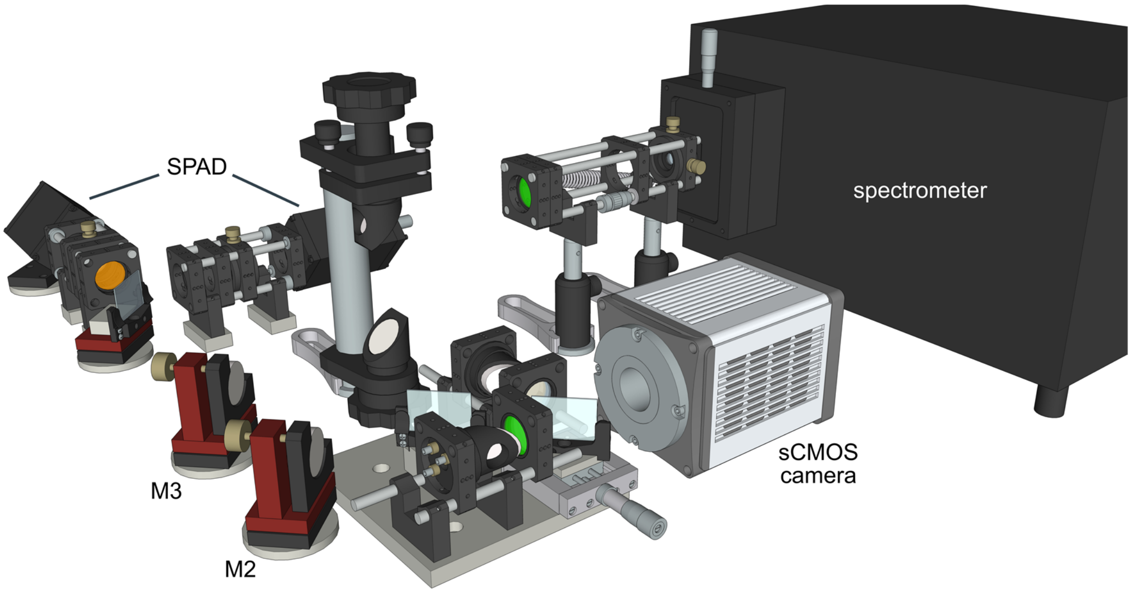

Figure 4.7 | Detection unit layout. Magnetic mirror holders M2 and M3 are used to direct the sample signal either to an sCMOS camera via an image splitter (see Figure 4.8) or a spectrometer (see Figure 4.9). Otherwise, the signal can be detected with different SPAD configurations (see Figure 4.11 and Figure 4.12).

The first detector is an sCMOS camera with 2048 x 2048 pixels on a 13.3 x 13.3 mm sized sensor, here mainly used for SMLM in combination with epi-fluorescence, TIRFM or VAEM illumination. For optimal results in SMLM, the focal length of the achromatic imaging lenses in front of the camera (also called tube lenses in this context) were chosen to be 100 mm to achieve Nyquist sampling:

According to equation (2.7), with the microscope objective's NA of 1.49, a fluorescence spot of the dye Cy3 (λ_{em} = 570 nm) will have an FWHM of roughly 230 nm. The objective's magnification is specified as 100x (based on a ZEISS tube lens with a focal length of 165 mm), therefore the effective magnification using a 100 mm lens is 60x. The camera pixel size is 6.5 µm, resulting in an effective pixel size of 108 nm. Thus, a fluorescence spot on the camera will extend 2-3 pixel in x- and y-direction, which is well within the commonly accepted boundaries to satisfy Nyquist sampling. This also holds true for other dyes from the blue to red spectral range.

Due to the large physical dimensions of the sCMOS camera chip, it is possible to use an image splitter to separate different colors in the sample and project them onto two different areas of the chip, therefore allowing parallel multicolor imaging (Figure 4.8). The image splitter is a custom-built modular component that was based on a design [122] by the Schäffer group (ZMBP, University of Tübingen). For this microscope, the image splitter was conceptualized and constructed in a student internship by Antonia Grauel.

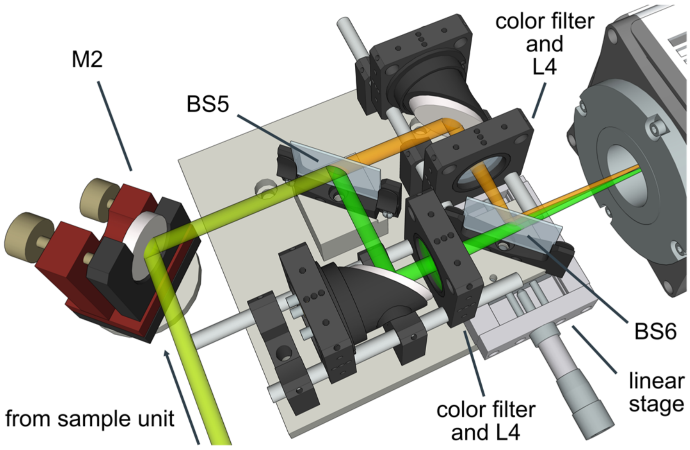

Figure 4.8 | Fluorescence emission image splitter. Emission light from the sample (yellow, from the lower left) is reflected by mirror M2 onto the first dichroic long pass beam splitter BS5 that separates the color channels (orange, green). Each channel is reflected by a mirror, then passes suitable band pass color filters and imaging lenses L4. The combining short pass beam splitter BS6 is mounted on a linear stage to control the lateral separation of the channels on the camera chip.

Here, the sample emission is separated by a dichroic long pass beam splitter BS5 into two separate arms (green and orange). Color filters further narrow the spectral region for each signal. Each arm is focused by a separate lens L4 and again combined by a short pass beam splitter BS6 mounted on a linear translation table to achieve a lateral color channel separation on the camera chip. The main advantages of this design are: a) separate focusing lenses to minimize chromatic aberration for both color channels; b) the emission light can pass through the center of each lens to minimize astigmatism; c) each emission arm experiences the same number of reflections and transmissions; and d) compact construction with exchangeable filters for other fluorophore pairs. Furthermore, the image splitter is bolted to a plate that can be easily removed or reattached according to the experimental requirements.

Using confocal illumination, the next detector is a spectrograph consisting of a 30 cm focal length imaging monochromator and a thermoelectrical cooled CCD camera with 1340 x 100 pixels and high (> 80%) quantum efficiency in the visible range. As the entrance slit is located 12.4 cm above the optical table, the emission beam is first elevated by a periscope assembly before it is focused onto the entrance slit by an *xyz*-adjustable achromatic lens L5 with a focal length of 20 mm to satisfy the f/4 specification of the monochromator considering an approximate beam diameter of 5 mm (see Figure 4.9).

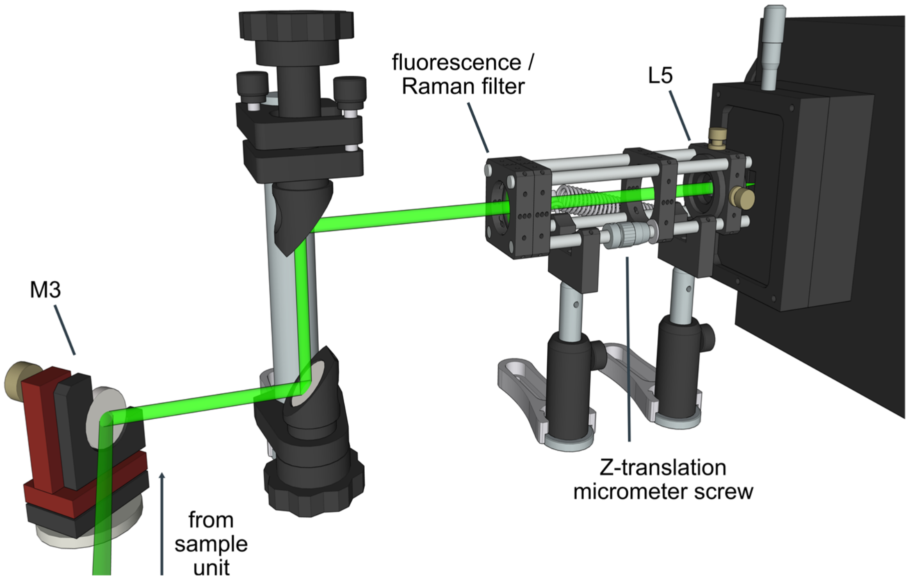

Figure 4.9 | Spectroscopy beam path. Mirror M3 directs the sample signal (green, from the lower left) to a periscope assembly that elevates the adjusts the beam height to the spectrometer's optical path height. A fluorescence or Raman long pass filter first rejects reflected laser light, then achromatic lens L5 focuses on the spectrometer's entrance slit. The lateral focus position can be aligned with the lens holder screws, while the axial position is set by moving the whole upper optical scaffold along the optical axis. The combination of a micrometer screw with a tension spring allows for very smooth adjustments.

Typically, a long pass filter is inserted in front of the lens to block reflected laser light. Both fluorescence (single-molecule) spectroscopy and Raman spectroscopy (see examples in Figure 4.10) have a wide variety of applications in many fields of science.

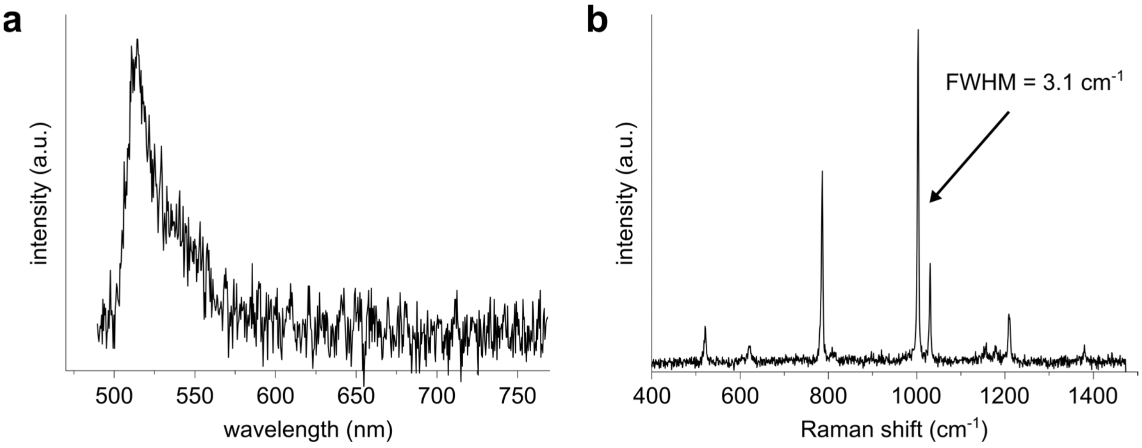

Figure 4.10 | Exemplary spectroscopy data. (a) Fluorescence emission spectrum of a single fluorescent protein, acquired using 488 nm excitation and a grating with 300 grooves / mm. **(b)** Raman spectrum of organic standard substance toluene in solution, acquired using 632.8 nm excitation and a grating with 1200 grooves / mm. The indicated peak at 1003 cm^{-1} was fitted with a Lorentzian function to calculate the full width at half maximum (FWHM).

The present spectrometer supports both methods with high spectral resolution using two different blazed diffraction gratings (300 and 1200 grooves / mm). The theoretical spectroscopic parameters listed in Table 2 are manufacturer specifications based on the instrument design and ignore the signal line width, optical aberrations and other factors that can negatively affect the spectral resolution. Nevertheless, the measured resolution (FWHM of the 1003 cm^{-1} peak of the Raman standard substance toluene in Figure 4.10b) of 3.1 cm^{-1} is very close to the theoretical resolution of 3.0 cm^{-1}, showing that the spectroscopy module is operated at top efficiency.

Table 2 | Performance parameters for typical spectroscopy experiments. The values are calculated for the given excitation wavelength, 300 µm focal length, 25 µm slit width, 1340 horizontal pixels on the camera with 20 µm pixel size. The resolution (linewidth) is calculated for a signal covering 3 pixels, for Raman spectroscopy at the middle of the covered range.

	Fluorescence spectroscopy (λ_{exc} = 488 nm)		**Raman spectroscopy (λ_{exc} = 632.8 nm)**	
grating (grooves / mm)	600	1200	600	1200
covered range	278 nm	57 nm	4797 cm^{-1}	1314 cm^{-1}
resolution	0.62 nm	0.13 nm	10.4 cm^{-1}	3.0 cm^{-1}

These spectroscopic capabilities not only extend the microscope's usability for a very diverse set of experiments but they also offer interesting method combinations with biological relevance, as will be demonstrated in the following example: in a study [123] examining DsRed_N42H fluorescent proteins, individual species were first immobilized on a cover slip, detected with confocal fluorescence imaging and analyzed with single-molecule fluorescence spectroscopy (using analogous steps as presented in chapter 3.4). After depositing a thin silver island film onto the sample, previously bleached and non-bleached proteins were then addressed with surface-enhanced Raman spectroscopy using the same microscope. The correlation of distinct spectral forms of individual molecules (fluorescence spectroscopy) with the structural fingerprint of the native species and their photoproducts (Raman spectroscopy) provided a comprehensive method to analyze the underlying photo-degeneration processes and illustrated the benefit of different spectroscopic techniques combined on one microscope platform.

By synchronizing the camera acquisition with the movement of the piezo sample table, this also offers the possibility of spectral mapping by raster scanning the sample and collecting spectral information for each point.

The following detector block features single-photon avalanche diodes (SPADs) for their use in confocal techniques like FLIM, FLIM-FRET, FIDSAM, FLCS, antibunching or other experiments with single-molecule detection. Both SPAD and pulsed laser synchronization signals are fed into a TCSPC unit to measure the time delay between sample excitation and the arrival of an emitted photon at the detector. All abovementioned techniques can be performed and analyzed by the proprietary software SymPhoTime that accompanies the TCSPC instrumentation.

While most commercial microscopes feature adjustable pinholes for confocal measurements, here, different detection paths can be chosen depending on the requirements of the experiment. In some single-molecule experiments, the emitter separation is already sufficient and the biggest concern is signal intensity. In these cases, a pinhole is unnecessary and a lens L7 with f = 200 nm directly focuses the emission beam on the SPAD detector, resulting in an Airy disk size of 54 µm (550 nm emission wavelength, 5 mm beam diameter) that is much smaller than the 100 µm diameter of the SPAD's active area (Figure 4.11a, Figure 4.2c).

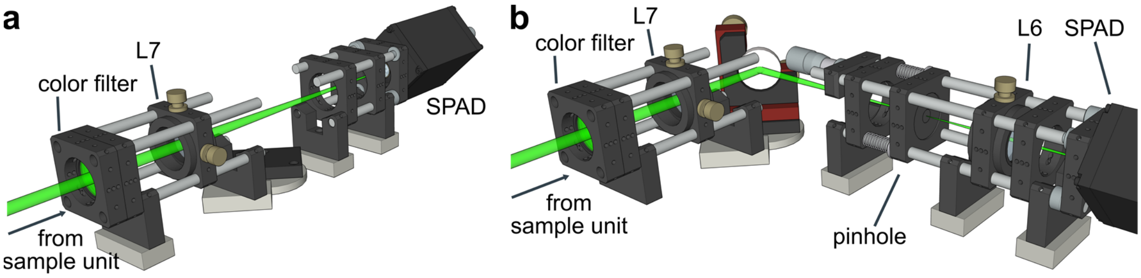

Figure 4.11 | Detector configurations with one detector. (a) For experiments with low signal intensity, lens L7 focuses directly on the SPAD. The resulting Airy disk is much smaller than the detector's active area, thus enhancing the photon collection efficiency. **(b)** When optical sectioning is necessary, a mirror (for lateral adjustment) guides the focused beam through a suitable pinhole (adjustable in z), then lens L6 focuses on the SPAD.

Moreover, this detection pathway was specially designed for the smallest number of optical elements between microscope objective and detector to maximize the photon collection efficiency.

When optical sectioning is necessary, particularly in biological samples with high levels of autofluorescence, an *xy*-adjustable mirror can be inserted to steer the focused beam through a *z*-adjustable pinhole (50 µm ≙ 1 Airy Unit), before focusing on a SPAD with another lens L6 to allow confocal measurements (Figure 4.11b, Figure 4.2d). A third option uses a different focusing lens L8 with f = 400 nm (Figure 4.2e), resulting in an Airy disk size of 107 µm (with above parameters). Therefore, the available SPAD detector area serves as a pinhole, providing some out-of-focus light rejection while reducing the number of optical elements for better signal intensity.

To validate these different options, their resolution and achievable signal intensities must be quantified. As already discussed in chapter 2.1.4, the theoretical lateral confocal resolution according to Cole et al.[18] is given by

$$r_{0,\mathrm{FWHM}} = \frac{0.51 \cdot \lambda_{exc}}{\mathrm{NA}} \tag{4.1}$$

and can be compared with the FWHM of experimentally acquired PSFs from point emitters that are fitted with a Gaussian function. From their experience, a well-adjusted confocal microscope should show PSF sizes within 10-40% of this theoretical resolution, while the PSF shape is also a measure for the overall imaging system quality. Instead of their suggested fluorescent microspheres, here, 40 nm diameter gold nanospheres are used to acquire scattering images with the 488 nm laser line. Being exceptionally bright and stable, the same nanosphere can be imaged multiple times to estimate the resolution and additionally determine the relative intensity for all three aforementioned beam path options (see Table 3) by fitting each PSF intensity profiles in all directions with a Gaussian function, then calculating the FWHM and amplitude.

Table 3 | Comparison of confocal resolution and signal intensity. The FWHM for each direction was calculated from a Gaussian fit function of the corresponding PSF intensity profile. The results represent the average of five separate gold nanospheres. All intensities were derived from the Gaussian fit function's amplitude in *z* direction, relative to the case without pinhole for each gold nanosphere before averaging.

	$\mathrm{FWHM}_{\mathrm{PSF}}$ (nm)			**Relative intensity**
	x	*y*	*z*	
Without pinhole	204	215	617	1
Detector as pinhole	182	182	507	0.85
With pinhole	155	143	479	0.59
Theory	167	167	347	

The experimental resolution for the confocal case (with pinhole) shows that the lateral values are smaller and the axial values higher than the theoretical values, but both are well within the aforementioned margins. Discrepancies between *x*- and *y*-values could however point to deposited dirt particles in the pinhole or its slightly imperfect adjustment, especially when seen in contrast to the more homogeneous lateral resolution estimation for the other two cases. The difference in axial resolution also follows the expected trend and underscores the necessity of pinholes for optional sectioning. Concerning the relative signal intensity, the gain in resolution using a pinhole is accompanied with an intensity loss up to 40%. These measurements show that the microscope setup is well equipped to acquire diffraction-limited confocal images, and they also help to decide which emission pathway should be chosen for a selected experiment. Moreover, using the detector area as a pinhole proved to strike a favorable balance between resolution and signal intensity.

As the available TCSPC unit can process the signals of two SPADs via a router, a dichroic beam splitter BS7 can be inserted into the existing beam path as shown in Figure 4.12a (also refer to Figure 4.2a) to allow for dual-color experiments that are easily implemented due to the available multiple laser lines and the multiband excitation/emission beam splitter.

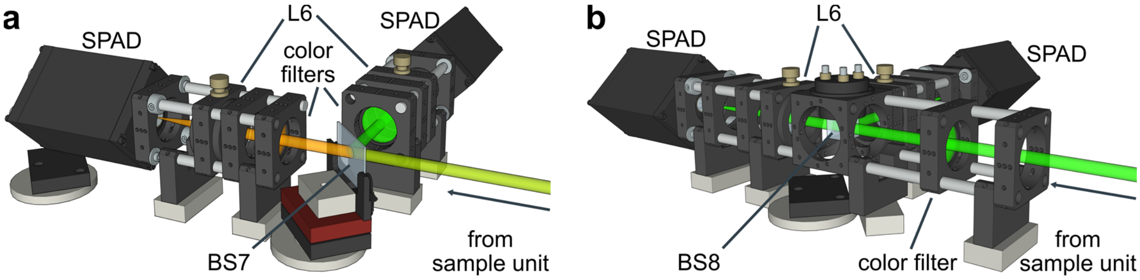

Figure 4.12 | Detector configurations with two detectors. (a) For dual-color experiments, the dichroic beam splitter BS7 separated the sample signal (yellow, from the right) into two arms (green, orange). Both are equipped with band pass color filters and independently adjustable lenses L6 to focus the signal on the respective SPAD. **(b)** In a similar arrangement, a suitable beam splitter cube BS8 can also separate the signal 50:50 for antibunching experiments or by its polarization for anisotropy experiments.

Using the existing cage system, the dichroic beam splitter can be replaced with beam splitter cube BS8 (Figure 4.12b, Figure 4.2b) to enable further experimental options, for example, 50:50 signal splitting for antibunching experiments. Provided that linear polarization optics are inserted in the excitation path (see Figure 4.2, box P), a polarizing beam splitter cube also enables fluorescence anisotropy measurements in solution or even anisotropy imaging. As a side note, some plate beam splitters and especially beam splitter cubes can introduce aberrations when placed in a divergent beam. Therefore, each SPAD uses a separate focusing lens L6 placed after the beam splitter.

4.2.6 Hardware and Software Control

Every technique and method that was implemented in the custom-built microscope makes use of a certain set of components that were mostly acquired from different vendors. This not only made it possible to select optimal parameters for each device, but also proved to be more cost-effective than all-in-one solutions from one company. This design approach was adopted early on to ensure flexibility and adaptability, for example to explore new techniques or to integrate equipment from cooperation partners.

However, this also raises the problem that each device uses its own control software and GUI, which is detrimental to user-friendliness and also complicates the combination of different spectroscopic methods. Therefore, a comprehensive software platform is required that not only offers central instrument control, but can also forward measurement data to analysis modules. Several options were tested for their practicality, including the open-source software µManager (Open Imaging, Burlingame, USA) and the commercially available software packages Simulink (MathWorks, Natick, USA) and LabVIEW (National Instruments, Austin, USA). An important selection factor was the adaptability and intuitiveness of the software structure. Especially with regard to sustainability, future users should only need a short period of time to familiarize themselves with the software for maintenance or to implement changes and additions. For these reasons, µManager proved to be unsuitable for the existing microscope setup, as both customization and writing of new modules was cumbersome. Both LabVIEW and Simulink are specialized programming tools, widely used in industrial applications for system control, simulation and engineering design. They are intended for dataflow modeling, using graphical wrappers such as icons for modules and wires for connections to represent built-in code building blocks. Decision trees, for instance, to control and synchronize external devices, can be realized quickly and intuitively. Moreover, companies that produce scientific instruments often provide compatible drivers or software libraries that allow an easy implementation.

Simulink and MATLAB, the main analysis programming language throughout this work, are from the same company, which would suggest better compatibility. However, Simulink leans more toward running dynamic simulations, while LabVIEW focuses more on measurement systems and hardware control. Due to the requirements of the custom-built microscope, LabVIEW was therefore preferred. Moreover, its hardware driver database is more extensive and it also features several options to interface with MATLAB, allowing data transfer between the two programming environments.

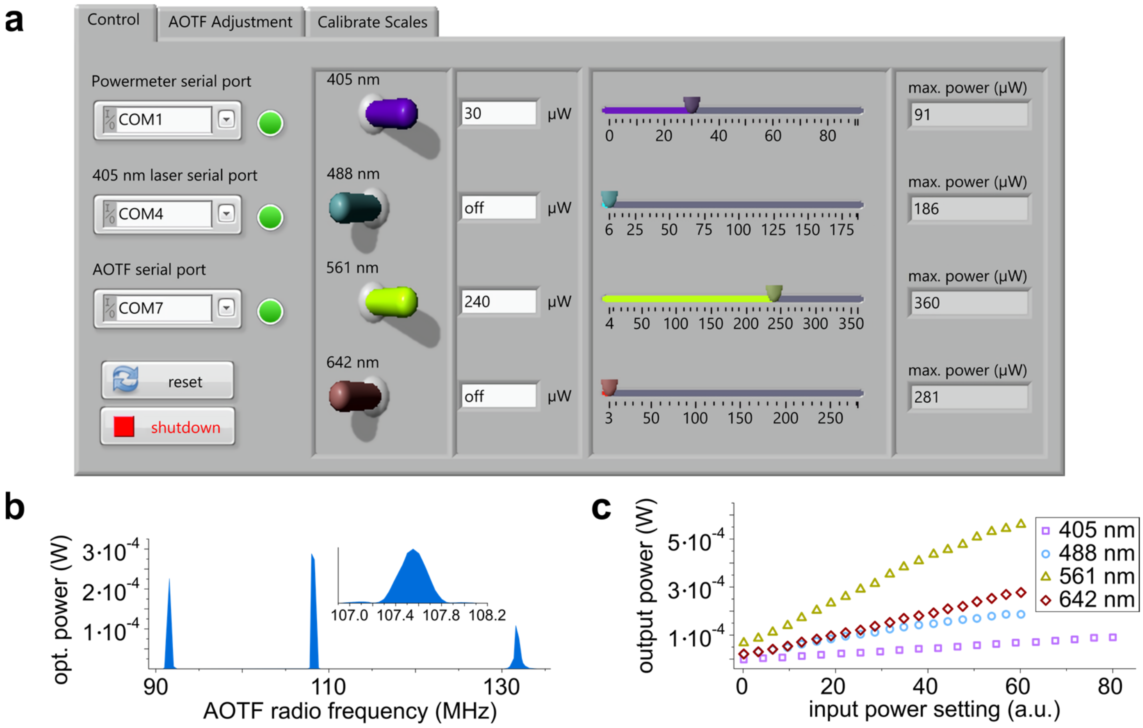

Powermeter serial port: COM1

405 nm laser serial port: COM4

AOTF serial port: COM7

405 nm: 30 µW, max. power (µW): 91

488 nm: off µW, max. power (µW): 186

561 nm: 240 µW, max. power (µW): 360

642 nm: off µW, max. power (µW): 281

Figure 4.13 | Laser control GUI and calibration graphs. (a) Custom-built user interface to control active laser lines and their optical power, additional tabs “AOTF Adjustment” (see b) and “Calibrate Scales” (see c) enable calibration procedures. **(b)** Frequency sweeps (inset with higher resolution) can automatically adjust the AOTF settings to maximize transmittance for the respective laser lines. **(c)** Optical power output at the sample plane for corresponding power settings of the 405 nm laser (violet squares) or the AOTF that controls the 488 nm (blue circles), 561 nm (yellow triangles) and 642 nm (red diamonds) laser lines. This calibration updates the scales in the “Control” tab **a**, allowing to set the power at the sample plane in absolute values.

To demonstrate the applicability, Figure 4.13a shows the GUI for a program module that controls the CW lasers presented in chapter 4.2.2. Here, the 405 nm laser is controlled directly, while the other laser lines are controlled via the AOTF. Part of the program uses an external power meter to optimize the AOTF frequencies (see Figure 4.13b). When the power sensor is placed in the sample plane, power calibration curves are also recorded for each laser line (see Figure 4.13c). Deviations from the ideal linear behavior (as evident for the 561 nm laser line) can then be taken into account by fitting the data with polynomial functions to acquire correct calibration coefficients. This initialization routine ensures that the target power value in the GUI always corresponds to the actual irradiance in the sample plane. This generally important parameter in spectromicroscopy is key for many live cell imaging experiments. Plant cells are naturally sensitive to changes in light intensity, but animal cells can also show stress responses due to microscopy illumination, which of course cannot be completely avoided in optical imaging. To reduce the experimental variance, sample irradiance should therefore at least be kept constant, especially for long test series with biological replicates. Commercial microscope users are often instructed to adjust the laser power (given in percent) until the image quality is acceptable. However, due to laser intensity degradation in heavy-duty systems, gradual misalignment or manual readjustment of the fiber couplers, this relative power setting is non-repeatable. Lower image quality at the relative power setting may then be misinterpreted as a hardware issue by the user, who compensates with higher laser intensity. However, if the reason was a lower fluorophore expression level in the sample, then this introduces more photobleaching and phototoxicity and may therefore skew experimental results. As demonstrated, the custom-built user interface can easily address such concerns by adding appropriate program blocks, setting it apart from the proprietary software of commercial microscopes.

A comprehensive user interface offers further advantages in scientific data management. While commercial software stores many parameters in the metadata of recorded images, the degree of documentation can vary for each system. This is a problem for central data storage facilities where standardized database formats are essential for efficient archiving and fast retrieval.

The self-written software therefore offers the possibility to collect all desired parameters automatically (date, irradiance, filter settings, image resolution, etc.) or to retrieve them via user input (project number, tissue type, sample preparation, etc.) and to compile this information for storage in the desired format. In addition, the parameters of connected analysis modules, such as 2D Gauss fitting parameters for SMLM, can also be saved. This allows the raw data, hardware settings, data analysis and parameters to be clearly assigned to each other to ensure transparency and reusability.

5 Conclusion

Where do we come from? What are we? Where are we going?

The title of one of Paul Gaugin's most famous works (*D'où venons-nous? Que sommes-nous? Où allons-nous?*) exemplifies the fundamental questions that we can ask about our own existence. For the exploration of life itself, no other research discipline is more suited to ask and possibly answer such vital questions than the life sciences. In addition, they contribute many practical applications to our everyday lives, for example in medicine, pharmacy, agriculture, the environment and the food industry. Accordingly, it becomes clear to what extent our lives can benefit from a deeper understanding of these matters. Research on living organisms has shown that life is not only structured at the cellular level, but also controlled by an extremely complex network of molecular interactions. This makes it all the more important to develop techniques that can visualize these biological functions in living cells. Microscopy and spectroscopy methods are ideal complements, as their combination provides a wealth of information beyond pure imaging. This work demonstrates that the theoretical and practical expertise has been achieved for different spectromicroscopy techniques, which allowed them to be successfully applied in several scientific projects. These contributions to current research have also been used to evaluate which advanced microscopy techniques are particularly valuable to gain scientific knowledge in the life sciences.

Two projects focused on protein-protein interaction experiments that are one of the most important tools for revealing the complex molecular mechanisms of living systems. As demonstrated, spectromicroscopy has the decisive advantage of carrying out these measurements in the natural physiological environment. The FLIM-FRET technique offered robust and reliable analyses for this type of experiment. In contrast to many in vitro interaction assays, it is viable for almost every cell compartment and additionally provides spatial information about the interaction sites.

Microscope images rely heavily on good contrast, which causes problems especially in highly autofluorescent tissues. The FIDSAM method for contrast enhancement, originally developed for plant cells, emerged from the FLIM technique and showed that such advanced methods have great potential for further development in live cell imaging. In this work, FIDSAM was further refined and is now suitable for all current microscope systems with FLIM capability. Its applicability was demonstrated in histopathology, which additionally underlines the interdisciplinary benefit of this technique.

As mentioned above, spectroscopy is an indispensable companion of modern microscopy. This was underlined with the example of another protein-protein interaction method: multicolor BiFC. Supported by various spectroscopic methods, photophysical parameters of artificial fluorescence probes were determined and then confirmed by in vivo experiments with three concurrent interaction partners. This provided selection criteria for suitable probe combinations as well as a basis for quantifying the interactions. As many parameters are usually hidden in ensemble experiments, single-molecule spectroscopy was employed to pinpoint the origin of certain photophysical effects down to the amino acid level. This data could also serve as a starting point for the improvement of multicolor BiFC probes.

The capability for single-molecule detection was a crucial factor to establish superresolution. This rapidly growing research area is becoming more and more important in the life sciences, as it enables the visualization of previously hidden structural features beyond the classical resolution limit. The successful implementation of SMLM techniques was first demonstrated on biological test samples and then applied in a research project. In addition to structural information, the investigation of dynamic processes with high spatial and temporal resolution are of great interest for current research. The sptPALM technique proved to be an ideal complement to the implemented superresolution methods, which was shown by the analysis of protein dynamics in plant cell membranes.

Finally, the nanoscopic flow sensor project realized an interdisciplinary research endeavor. Conception, synthesis and functional testing involved different scientific disciplines and benefited from the range of available spectromicroscopy techniques. Thus, the application of methodologies and theoretical concepts from different scientific fields shows great creative potential. The ability to work on projects beyond the life sciences also extends future scientific collaborations.

With the experience gained from the abovementioned projects, a microscope platform was designed and built that offers a unique combination of advanced light microscopy techniques. In the context of interdepartmental imaging core facilities, such a custom-built system has invaluable advantages. Due to its modularity, new techniques can be evaluated and implemented quickly, offering a time advantage for research projects in a competitive field. Owed to the diversity of biological samples, commercial devices are often unable to meet all experimental requirements. The adaptability of the custom microscope platform to a specific experiment can therefore be decisive for a project. In addition, different spectroscopic techniques can be operated in parallel, enabling multiparameter analyses that strengthen the robustness of experimental findings. As scientific research is commonly highly specialized, it benefits strongly from additional or alternative techniques that can contribute new analysis parameters to existing methods in the respective fields. The microscope therefore also serves as an interface between different scientific disciplines, as it provides users with a more complete picture of spectroscopic methods that are applied across the natural sciences thus stimulating scientific knowledge transfer between participating departments. As shown in this work, the possibility to analyze complex scientific phenomena with different approaches has led to many interdisciplinary, fruitful collaborations. Considering the high acquisition costs of commercial microscopes, the custom-built platform is very cost-effective, especially regarding the large array of different spectroscopic techniques. Specialized commercial research microscopes with additional spectroscopy modules can quickly cost up to one million euros, which is a major hurdle for most research departments. The microscope presented here can be built for less than a quarter of this amount and combines techniques that would not be available on any single commercial instrument in this form. For imaging departments, it can also be used to evaluate new techniques to strategize spending plans for commercial instrument extensions.

This multitude of application possibilities and advantages makes the presented microscopy platform an indispensable instrument of our research. We explicitly aim to make such an instrument accessible to other researchers, who can use the detailed description of the assembly as a blueprint.

It must be pointed out that mastering the necessary expertise for this multitude of methods can be very time-consuming. In addition to theoretical and practical skills of the spectromicroscopy techniques themselves, both technical planning and precise implementation are a prerequisite to engineer such a high-end optical setup. Moreover, basic knowledge of electronics and good programming skills are useful for efficient device control. Self-written software is often necessary for comprehensive data evaluation, especially when results of different techniques are to be correlated or standardized. For the strategy adopted here, methods were successively evaluated and added on the basis of scientific projects, utilizing the existing infrastructure of extensive spectroscopic equipment and expert knowledge. Without such support structures, the necessary know-how may be laborious to acquire and therefore represents a limitation for the construction of this system.

Of course, the implemented techniques are not exhaustive. They were chosen for typical applications in life science research and their flexible combination range. There are many other microscopy techniques that are more suitable for certain scientific questions, but difficult to integrate into the existing platform. Therefore, if highly specialized instruments are readily available, then they should be used in the spirit of scientific collaboration. On the other hand, the implementation into the custom-built microscope may be justified if the combined application of different techniques provides a significant advantage.

With regard to future technical developments, the complete automation of the setup will further enhance its user-friendliness. For coarse mechanical adjustments (filter wheels, shutters, beam path redirections, etc.), servo or stepper motors can be controlled by LabVIEW via an open source single-board microcontroller, which is straightforward and cost-effective. Furthermore, a focus stabilization system should be installed to counteract thermal focus drift, in particular for long superresolution measurements or time-lapse experiments. A common method uses a near infrared laser that is reflected at the sample coverslip under TIRF conditions and then directed to a position sensor. Any change in the objective-coverslip-distance is registered as a lateral shift on the sensor and can be countered by a corresponding motion of the objective in a feedback loop.

On the side of further research, there are several promising combinations of techniques that were not yet validated in this work. As already described in chapter 3.2, the combination of FLIM-FRET and anisotropy can provide more information about size of membrane complexes. This could be a powerful tool, in particular when compared with results from superresolution microscopy. The SMLM techniques are in principle already quantitative methods, since they can count the fluorescence events of individual emitters. Accordingly, it should be possible to correlate the determined localizations at one point with the actual number of labelled target proteins, for example, in a larger complex. Currently, this approach still shows many problems due to unpredictable blinking events and incomplete labeling. A multimodal approach with fundamentally different techniques would therefore help to put these results on a stronger footing.

Another example is the determination of diffusion coefficients that can be measured with two independent methods (sptPALM and FCS), enabling the mutual confirmation of experimental results. It has already been mentioned in chapter 3.5.3 that sptPALM could also be combined with FRET. Since sptPALM not only records the single emitters' position but also their intensity, dual-color experiments (using intensity-based FRET) could be used to map single interaction events.

Chapter 3.6.5 described an optimization technique for the structure of surface sensors. This could also be quite interesting for other research fields. In ligand binding assays, ssDNA is bound directly to the surface, awaiting hybridization with a suitable counterpart in the solution. Surface absorption and misfolding therefore can be problematic. Small DNA origami anchors, extending farther into the solution, with computationally optimized target structures thus might have better sensitivity.

Computer algorithms will undoubtedly become very important in all microscopy techniques involving large amounts of data. In particular, superresolution technologies are expected to develop even further in the coming years, not least through the increased use of artificial intelligence to improve image quality. Such interdisciplinary approaches are therefore of great importance for the continuation of cutting-edge research.

6 References

[1] A. Jabłoński, "Über den Mechanismus der Photolumineszenz von Farbstoffphosphoren," *Zeitschrift für Physik,* vol. 94, no. 1, pp. 38-46, 1935.

[2] M. Kasha, "Characterization of electronic transitions in complex molecules," *Discussions of the Faraday Society,* vol. 9, pp. 14-19, 1950.

[3] G. G. Stokes, "Über die Veränderung der Brechbarkeit des Lichts," *Annalen der Physik,* vol. 163, no. 11, pp. 480-490, 1852.

[4] E. U. Condon, "Coupling of Electronic and Nuclear Motions in Diatomic Molecules," *Proceedings of the National Academy of Sciences of the United States of America,* vol. 13, no. 6, pp. 462-466, 1927.

[5] J. Franck and E. G. Dymond, "Elementary processes of photochemical reactions," *Transactions of the Faraday Society,* vol. 21, pp. 536-542, 1926.

[6] E. U. Condon, "A Theory of Intensity Distribution in Band Systems," *Physical Review,* vol. 28, no. 6, pp. 1182-1201, 1926.

[7] W. Heisenberg, "Über den anschaulichen Inhalt der quantentheoretischen Kinematik und Mechanik," *Zeitschrift für Physik,* journal article vol. 43, no. 3, pp. 172-198, 1927.

[8] C. V. Raman and K. S. Krishnan, "A New Type of Secondary Radiation," *Nature,* vol. 121, pp. 501-502, 1928.

[9] A. Smekal, "Zur Quantentheorie der Dispersion," *Naturwissenschaften,* vol. 11, no. 43, pp. 873-875, 1923.

[10] H. J. Butler *et al.*, "Using Raman spectroscopy to characterize biological materials," *Nature Protocols,* vol. 11, no. 4, pp. 664-687, 2016.

[11] E. Abbe, "Beiträge zur Theorie des Mikroskops und der mikroskopischen Wahrnehmung," *Archiv für mikroskopische Anatomie,* vol. 9, no. 1, pp. 413-468, 1873.

[12] C. Huygens, *Traité de la Lumière*. Leiden, The Netherlands: Pierre Van der Aa, 1690.

[13] A. Fresnel, "Mèmoire sur la diffraction de la lumière," *Mémoires de l'Académie des sciences de l'Institut de France,* vol. 5, pp. 339-475, 1826.

[14] M. Müller, *Introduction to Confocal Fluorescence Microscopy*, 2 ed. Bellingham, WA, USA: SPIE Press, 2005, p. 138.

[15] W. H. Richardson, "Bayesian-Based Iterative Method of Image Restoration," *Journal of the Optical Society of America,* vol. 62, no. 1, pp. 55-59, 1972.

[16] L. B. Lucy, "An iterative technique for the rectification of observed distributions," *The Astronomical Journal,* vol. 79, no. 6, pp. 745-754, 1974.

[17] M. Minsky, "Microscopy apparatus," Patent US3013467, 1961.

[18] R. W. Cole, T. Jinadasa, and C. M. Brown, "Measuring and interpreting point spread functions to determine confocal microscope resolution and ensure quality control," *Nature Protocols,* vol. 6, no. 12, pp. 1929-1941, 2011.

[19] E. J. Ambrose, "A surface contact microscope for the study of cell movements," *Nature,* vol. 178, no. 4543, p. 1194, 1956.

[20] C. A. Konopka and S. Y. Bednarek, "Variable-angle epifluorescence microscopy: a new way to look at protein dynamics in the plant cell cortex," *The Plant Journal,* vol. 53, no. 1, pp. 186-196, 2008.

[21] J. R. Lakowicz, *Principles of Fluorescence Spectroscopy*, 3 ed. New York, NY, USA: Springer US, 2006.

[22] B. Valeur and M. N. Berberan-Santos, *Molecular Fluorescence: Principles and Applications*, 2 ed. Weinheim, Germany: Wiley-WCH, 2012.

[23] M. Y. Berezin and S. Achilefu, "Fluorescence lifetime measurements and biological imaging," *Chemical Reviews,* vol. 110, no. 5, pp. 2641-2684, 2010.

[24] M. Maus *et al.*, "An experimental comparison of the maximum likelihood estimation and nonlinear least-squares fluorescence lifetime analysis of single molecules," *Analytical Chemistry,* vol. 73, no. 9, pp. 2078-2086, 2001.

[25] F. Schleifenbaum *et al.*, "Fluorescence intensity decay shape analysis microscopy (FIDSAM) for quantitative and sensitive live-cell imaging: a novel technique for fluorescence microscopy of endogenously expressed fusion-proteins," *Molecular Plant,* vol. 3, no. 3, pp. 555-562, 2010.

[26] T. Förster, "Zwischenmolekulare Energiewanderung und Fluoreszenz," *Annalen der Physik,* vol. 437, no. 1-2, pp. 55-75, 1948.

[27] E. Fišerová and M. Kubala, "Mean fluorescence lifetime and its error," *Journal of Luminescence,* vol. 132, no. 8, pp. 2059-2064, 2012.

[28] K. Elgass, K. Caesar, D. Wanke, K. Harter, A. J. Meixner, and F. Schleifenbaum, "Application of FLIM-FIDSAM for the in vivo analysis of hormone competence of different cell types," *Analytical and Bioanalytical Chemistry,* vol. 398, no. 5, pp. 1919-1925, 2010.

[29] K. Elgass, K. Caesar, K. Harter, A. J. Meixner, and F. Schleifenbaum, "Combining ocFLIM and FIDSAM reveals fast and dynamic physiological responses at subcellular resolution in living plant cells," *Journal of Microscopy,* vol. 242, no. 2, pp. 124-131, 2011.

[30] W. E. Moerner and L. Kador, "Optical detection and spectroscopy of single molecules in a solid," *Physical Review Letters,* vol. 62, no. 21, pp. 2535-2538, 1989.

[31] M. Orrit and J. Bernard, "Single pentacene molecules detected by fluorescence excitation in a p-terphenyl crystal," *Physical Review Letters,* vol. 65, no. 21, pp. 2716-2719, 1990.

[32] J. K. Trautman, J. J. Macklin, L. E. Brus, and E. Betzig, "Near-field spectroscopy of single molecules at room temperature," *Nature,* vol. 369, no. 6475, pp. 40-42, 1994.

[33] F. Pennacchietti, T. J. Gould, and S. T. Hess, "The Role of Probe Photophysics in Localization-Based Superresolution Microscopy," *Biophysical Journal,* vol. 113, no. 9, pp. 2037-2054, 2017.

[34] D. Magde, E. Elson, and W. W. Webb, "Thermodynamic Fluctuations in a Reacting System - Measurement by Fluorescence Correlation Spectroscopy," *Physical Review Letters,* vol. 29, no. 11, pp. 705-708, 1972.

[35] C. Blum, A. J. Meixner, and V. Subramaniam, "Room temperature spectrally resolved single-molecule spectroscopy reveals new spectral

forms and photophysical versatility of aequorea green fluorescent protein variants," *Biophysical Journal,* vol. 87, no. 6, pp. 4172-4179, 2004.

[36] F. Stracke, C. Blum, S. Becker, K. Müllen, and A. J. Meixner, "Correlation of Emission Intensity and Spectral Diffusion in Room Temperature Single-Molecule Spectroscopy," *ChemPhysChem,* vol. 6, no. 7, pp. 1242-1246, 2005.

[37] C. Blum, A. J. Meixner, and V. Subramaniam, "Single oligomer spectra probe chromophore nanoenvironments of tetrameric fluorescent proteins," *Journal of the American Chemical Society,* vol. 128, no. 26, pp. 8664-8670, 2006.

[38] T. Ha, T. Enderle, D. F. Ogletree, D. S. Chemla, P. R. Selvin, and S. Weiss, "Probing the interaction between two single molecules: fluorescence resonance energy transfer between a single donor and a single acceptor," *Proceedings of the National Academy of Sciences of the United States of America,* vol. 93, no. 13, pp. 6264-6268, 1996.

[39] A. F. Raigoza, J. W. Dugger, and L. J. Webb, "Review: Recent Advances and Current Challenges in Scanning Probe Microscopy of Biomolecular Surfaces and Interfaces," *ACS Applied Materials & Interfaces,* vol. 5, no. 19, pp. 9249-9261, 2013.

[40] M. Sackrow, C. Stanciu, M. A. Lieb, and A. J. Meixner, "Imaging Nanometre-Sized Hot Spots on Smooth Au Films with High-Resolution Tip-Enhanced Luminescence and Raman Near-Field Optical Microscopy," *ChemPhysChem,* vol. 9, no. 2, pp. 316-320, 2008.

[41] B. Huang, M. Bates, and X. Zhuang, "Super-resolution fluorescence microscopy," *Annual Review of Biochemistry,* vol. 78, pp. 993-1016, 2009.

[42] L. Schermelleh, R. Heintzmann, and H. Leonhardt, "A guide to super-resolution fluorescence microscopy," *Journal of Cell Biology,* vol. 190, no. 2, pp. 165-175, 2010.

[43] S. J. Sahl, S. W. Hell, and S. Jakobs, "Fluorescence nanoscopy in cell biology," *Nature Reviews Molecular Cell Biology,* vol. 18, no. 11, pp. 685-701, 2017.

[44] S. W. Hell and J. Wichmann, "Breaking the diffraction resolution limit by stimulated emission: stimulated-emission-depletion fluorescence microscopy," *Optics Letters,* vol. 19, no. 11, pp. 780-782, 1994.

[45] M. Hofmann, C. Eggeling, S. Jakobs, and S. W. Hell, "Breaking the diffraction barrier in fluorescence microscopy at low light intensities by using reversibly photoswitchable proteins," *Proceedings of the National Academy of Sciences of the United States of America,* vol. 102, no. 49, pp. 17565-17569, 2005.

[46] G. Vicidomini *et al.*, "Sharper low-power STED nanoscopy by time gating," *Nature Methods,* vol. 8, no. 7, pp. 571-573, 2011.

[47] S. Bretschneider, C. Eggeling, and S. W. Hell, "Breaking the Diffraction Barrier in Fluorescence Microscopy by Optical Shelving," *Physical Review Letters,* vol. 98, no. 21, p. 218103, 2007.

[48] S. W. Hell and M. Kroug, "Ground-state-depletion fluorescence microscopy: A concept for breaking the diffraction resolution limit," *Applied Physics B,* journal article vol. 60, no. 5, pp. 495-497, 1995.

[49] F. Balzarotti *et al.*, "Nanometer resolution imaging and tracking of fluorescent molecules with minimal photon fluxes," *Science,* vol. 355, no. 3625, pp. 606-612, 2017.

[50] E. Betzig *et al.*, "Imaging intracellular fluorescent proteins at nanometer resolution," *Science,* vol. 313, no. 5793, pp. 1642-1645, 2006.

[51] S. T. Hess, T. P. Girirajan, and M. D. Mason, "Ultra-high resolution imaging by fluorescence photoactivation localization microscopy," *Biophysical Journal,* vol. 91, no. 11, pp. 4258-4272, 2006.

[52] M. J. Rust, M. Bates, and X. Zhuang, "Sub-diffraction-limit imaging by stochastic optical reconstruction microscopy (STORM)," *Nature Methods,* vol. 3, no. 10, pp. 793-795, 2006.

[53] M. Heilemann, S. van de Linde, A. Mukherjee, and M. Sauer, "Super-resolution imaging with small organic fluorophores," *Angewandte Chemie International Edition in English,* vol. 48, no. 37, pp. 6903-6908, 2009.

[54] M. Heilemann *et al.*, "Subdiffraction-resolution fluorescence imaging with conventional fluorescent probes," *Angewandte Chemie International Edition in English,* vol. 47, no. 33, pp. 6172-6176, 2008.

[55] P. Lemmer *et al.*, "SPDM: light microscopy with single-molecule resolution at the nanoscale," *Applied Physics B,* vol. 93, no. 1, pp. 1-12, 2008.

[56] J. Fölling *et al.*, "Fluorescence nanoscopy by ground-state depletion and single-molecule return," *Nature Methods,* vol. 5, no. 11, pp. 943-945, 2008.

[57] E. Jensen and D. J. Crossman, "Technical Review: Types of Imaging—Direct STORM," *The Anatomical Record,* vol. 297, no. 12, pp. 2227-2231, 2014.

[58] C. E. Shannon, "Communication in the Presence of Noise," *Proceedings of the IRE,* vol. 37, no. 1, pp. 10-21, 1949.

[59] F. Huang *et al.*, "Video-rate nanoscopy using sCMOS camera-specific single-molecule localization algorithms," *Nature Methods,* vol. 10, no. 7, pp. 653-658, 2013.

[60] G. T. Dempsey, J. C. Vaughan, K. H. Chen, M. Bates, and X. Zhuang, "Evaluation of fluorophores for optimal performance in localization-based super-resolution imaging," *Nature Methods,* vol. 8, no. 12, pp. 1027-1036, 2011.

[61] D. M. Shcherbakova, P. Sengupta, J. Lippincott-Schwartz, and V. V. Verkhusha, "Photocontrollable fluorescent proteins for superresolution imaging," *Annual Review of Biophysics,* vol. 43, pp. 303-329, 2014.

[62] A. G. Godin, B. Lounis, and L. Cognet, "Super-resolution Microscopy Approaches for Live Cell Imaging," *Biophysical Journal,* vol. 107, no. 8, pp. 1777-1784, 2014.

[63] B. Huang, S. A. Jones, B. Brandenburg, and X. Zhuang, "Whole-cell 3D STORM reveals interactions between cellular structures with nanometer-scale resolution," *Nature Methods,* vol. 5, no. 12, pp. 1047-1052, 2008.

[64] T. Dertinger, R. Colyer, G. Iyer, S. Weiss, and J. Enderlein, "Fast, background-free, 3D super-resolution optical fluctuation imaging (SOFI)," *Proceedings of the National Academy of Sciences,* vol. 106, no. 52, pp. 22287-22292, 2009.

[65] T. Dertinger, R. Colyer, R. Vogel, J. Enderlein, and S. Weiss, "Achieving increased resolution and more pixels with Superresolution Optical

Fluctuation Imaging (SOFI)," *Optics Express,* vol. 18, no. 18, pp. 18875-18885, 2010.

[66] S. Geissbuehler, N. L. Bocchio, C. Dellagiacoma, C. Berclaz, M. Leutenegger, and T. Lasser, "Mapping molecular statistics with balanced super-resolution optical fluctuation imaging (bSOFI)," *Optical Nanoscopy,* journal article vol. 1, no. 1, pp. 4-10, 2012.

[67] S. Geissbuehler, C. Dellagiacoma, and T. Lasser, "Comparison between SOFI and STORM," *Biomedical Optics Express,* vol. 2, no. 3, pp. 408-420, 2011.

[68] L. S. Barak and W. W. Webb, "Diffusion of low density lipoprotein-receptor complex on human fibroblasts," *Journal of Cell Biology,* vol. 95, no. 3, pp. 846-852, 1982.

[69] M. J. Saxton and K. Jacobson, "Single-particle tracking: applications to membrane dynamics," *Annual Review of Biophysics and Biomolecular Structure,* vol. 26, pp. 373-399, 1997.

[70] C. Manzo and M. F. Garcia-Parajo, "A review of progress in single particle tracking: from methods to biophysical insights," *Reports on Progress in Physics,* vol. 78, no. 12, pp. 124601-124629, 2015.

[71] A. Keppler, S. Gendreizig, T. Gronemeyer, H. Pick, H. Vogel, and K. Johnsson, "A general method for the covalent labeling of fusion proteins with small molecules in vivo," *Nature Biotechnology,* vol. 21, no. 1, pp. 86-89, 2003.

[72] A. Keppler, H. Pick, C. Arrivoli, H. Vogel, and K. Johnsson, "Labeling of fusion proteins with synthetic fluorophores in live cells," *Proceedings of the National Academy of Sciences of the United States of America,* vol. 101, no. 27, pp. 9955-9959, 2004.

[73] A. Gautier *et al.*, "An engineered protein tag for multiprotein labeling in living cells," *Chemistry & Biology,* vol. 15, no. 2, pp. 128-136, 2008.

[74] S. Manley *et al.*, "High-density mapping of single-molecule trajectories with photoactivated localization microscopy," *Nature Methods,* vol. 5, no. 2, pp. 155-157, 2008.

[75] N. Chenouard *et al.*, "Objective comparison of particle tracking methods," *Nature Methods,* vol. 11, no. 3, pp. 281-289, 2014.

[76] A. Einstein, "Über die von der molekularkinetischen Theorie der Wärme geforderte Bewegung von in ruhenden Flüssigkeiten suspendierten Teilchen," *Annalen der Physik,* vol. 322, no. 8, pp. 549-560, 1905.

[77] M. J. Saxton, "Modeling 2D and 3D Diffusion," in *Methods in Membrane Lipids*, A. M. Dopico, Ed. Totowa, NJ, USA: Humana Press, 2007, pp. 295-321.

[78] N. Destainville and L. Salomé, "Quantification and Correction of Systematic Errors Due to Detector Time-Averaging in Single-Molecule Tracking Experiments," *Biophysical Journal,* vol. 90, no. 2, pp. L17-L19, 2006.

[79] M. A. Bopp, A. J. Meixner, G. Tarrach, I. Zschokke-Gränacher, and L. Novotny, "Direct imaging single molecule diffusion in a solid polymer host," *Chemical Physics Letters,* vol. 263, no. 6, pp. 721-726, 1996.

[80] O. Shimomura, F. H. Johnson, and Y. Saiga, "Extraction, Purification and Properties of Aequorin, a Bioluminescent Protein from the Luminous

Hydromedusan, Aequorea," *Journal of Cellular and Comparative Physiology,* vol. 59, no. 3, pp. 223-239, 1962.

[81] D. C. Prasher, V. K. Eckenrode, W. W. Ward, F. G. Prendergast, and M. J. Cormier, "Primary structure of the Aequorea victoria green-fluorescent protein," *Gene,* vol. 111, no. 2, pp. 229-233, 1992.

[82] M. Chalfie, Y. Tu, G. Euskirchen, W. W. Ward, and D. C. Prasher, "Green fluorescent protein as a marker for gene expression," *Science,* vol. 263, no. 5148, pp. 802-805, 1994.

[83] F. Yang, L. G. Moss, and G. N. Phillips, "The molecular structure of green fluorescent protein," *Nature Methods,* vol. 14, no. 10, pp. 1246-1251, 1996.

[84] A. B. Cubitt, R. Heim, S. R. Adams, A. E. Boyd, L. A. Gross, and R. Y. Tsien, "Understanding, improving and using green fluorescent proteins," *Trends in Biochemical Sciences,* vol. 20, no. 11, pp. 448-455, 1995.

[85] R. Heim and R. Y. Tsien, "Engineering green fluorescent protein for improved brightness, longer wavelengths and fluorescence resonance energy transfer," *Current Biology,* vol. 6, no. 2, pp. 178-182, 1996.

[86] M. V. Matz *et al.*, "Fluorescent proteins from nonbioluminescent Anthozoa species," *Nature Biotechnology,* vol. 17, no. 10, pp. 969-973, 1999.

[87] N. C. Shaner, R. E. Campbell, P. A. Steinbach, B. N. Giepmans, A. E. Palmer, and R. Y. Tsien, "Improved monomeric red, orange and yellow fluorescent proteins derived from Discosoma sp. red fluorescent protein," *Nature Biotechnology,* vol. 22, no. 12, pp. 1567-1572, 2004.

[88] E. A. Rodriguez *et al.*, "The Growing and Glowing Toolbox of Fluorescent and Photoactive Proteins," *Trends in Biochemical Sciences,* vol. 42, no. 2, pp. 111-129, 2017.

[89] E. Hebisch, J. Knebel, J. Landsberg, E. Frey, and M. Leisner, "High Variation of Fluorescence Protein Maturation Times in Closely Related Escherichia coli Strains," *PLOS ONE,* vol. 8, no. 10, pp. e75991-e75999, 2013.

[90] A. Hecker, N. Wallmeroth, S. Peter, M. R. Blatt, K. Harter, and C. Grefen, "Binary 2in1 vectors improve in planta (co-) localisation and dynamic protein interaction studies," *Plant Physiology,* vol. 168, no. 3, pp. 776-787, 2015.

[91] I. Ghosh, A. D. Hamilton, and L. Regan, "Antiparallel Leucine Zipper-Directed Protein Reassembly: Application to the Green Fluorescent Protein," *Journal of the American Chemical Society,* vol. 122, no. 23, pp. 5658-5659, 2000.

[92] C. D. Hu, Y. Chinenov, and T. K. Kerppola, "Visualization of Interactions among bZIP and Rel Family Proteins in Living Cells Using Bimolecular Fluorescence Complementation," *Molecular Cell,* vol. 9, no. 4, pp. 789-798, 2002.

[93] C. D. Hu and T. K. Kerppola, "Simultaneous visualization of multiple protein interactions in living cells using multicolor fluorescence complementation analysis," *Nature Biotechnology,* vol. 21, no. 5, pp. 539-545, 2003.

[94] Y. J. Shyu and C. D. Hu, "Fluorescence complementation: an emerging tool for biological research," *Trends in Biotechnology,* vol. 26, no. 11, pp. 622-630, 2008.

[95] Y. J. Shyu, C. D. Suarez, and C. D. Hu, "Visualization of AP-1–NF-κB ternary complexes in living cells by using a BiFC-based FRET," *Proceedings of the National Academy of Sciences,* vol. 105, no. 1, pp. 151-156, 2008.

[96] R. B. Horsch, "A Simple and General Method for Transferring Genes into Plants," *Science,* vol. 227, no. 4691, pp. 1229-1231, 1985.

[97] S. J. Clough and A. F. Bent, "Floral dip: a simplified method for Agrobacterium-mediated transformation of Arabidopsis thaliana," *The Plant Journal,* vol. 16, no. 6, pp. 735-743, 1998.

[98] A. Bent, "Arabidopsis thaliana Floral Dip Transformation Method," in *Agrobacterium Protocols*, K. Wang, Ed. Totowa, NJ, USA: Humana Press, 2006, pp. 87-104.

[99] S. Fields and O. Song, "A novel genetic system to detect protein-protein interactions," *Nature,* vol. 340, no. 6230, pp. 245-246, 1989.

[100] E. J. Licitra and J. O. Liu, "A three-hybrid system for detecting small ligand-protein receptor interactions," *Proceedings of the National Academy of Sciences of the United States of America,* vol. 93, no. 23, pp. 12817-12821, 1996.

[101] D. J. Sheerin *et al.*, "Light-Activated Phytochrome A and B Interact with Members of the SPA Family to Promote Photomorphogenesis in Arabidopsis by Reorganizing the COP1/SPA Complex," *The Plant Cell,* vol. 27, no. 1, pp. 189-201, 2015.

[102] G. Weidler *et al.*, "Degradation of Arabidopsis CRY2 is regulated by SPA proteins and phytochrome A," *Plant Cell,* vol. 24, no. 6, pp. 2610-2623, 2012.

[103] J. A. Levitt, D. R. Matthews, S. M. Ameer-Beg, and K. Suhling, "Fluorescence lifetime and polarization-resolved imaging in cell biology," *Current Opinion in Biotechnology,* vol. 20, no. 1, pp. 28-36, 2009.

[104] A. N. Bader, E. G. Hofman, P. M. P. v. B. e. Henegouwen, and H. C. Gerritsen, "Imaging of protein cluster sizes by means of confocal time-gated fluorescence anisotropy microscopy," *Optics Express,* vol. 15, no. 11, pp. 6934-6945, 2007.

[105] A. Nolte *et al.*, "Stented Vessels: A Challenge for Histological Preparation and Microscopy," *Journal of Interdisciplinary Histopathology,* vol. 1, pp. 104-112, 2013.

[106] S. Peter *et al.*, "Chimeric Autofluorescent Proteins as Photophysical Model System for Multicolor Bimolecular Fluorescence Complementation," *The Journal of Physical Chemistry B,* vol. 121, no. 11, pp. 2407-2419, 2017.

[107] C. Gadelha, B. Wickstead, P. G. McKean, and K. Gull, "Basal body and flagellum mutants reveal a rotational constraint of the central pair microtubules in the axonemes of trypanosomes," *Journal of Cell Science,* vol. 119, no. 12, p. 2405, 2006.

[108] P. Dedecker, S. Duwé, R. K. Neely, and J. Zhang, "Localizer: fast, accurate, open-source, and modular software package for superresolution

microscopy," *Journal of Biomedical Optics,* vol. 17, no. 12, p. 126008, 2012.

[109] J. Ries, C. Kaplan, E. Platonova, H. Eghlidi, and H. Ewers, "A simple, versatile method for GFP-based super-resolution microscopy via nanobodies," *Nature Methods,* vol. 9, no. 6, pp. 582-584, 2012.

[110] C. Speth *et al.*, "Arabidopsis RNA processing factor SERRATE regulates the transcription of intronless genes," *eLife,* vol. 7, p. e37078, 2018.

[111] E. Hosy, A. Martinière, D. Choquet, C. Maurel, and D. T. Luu, "Super-Resolved and Dynamic Imaging of Membrane Proteins in Plant Cells Reveal Contrasting Kinetic Profiles and Multiple Confinement Mechanisms," *Molecular Plant,* vol. 8, no. 2, pp. 339-342, 2015.

[112] N. Tarantino *et al.*, "TNF and IL-1 exhibit distinct ubiquitin requirements for inducing NEMO–IKK supramolecular structures," *The Journal of Cell Biology,* vol. 204, no. 2, pp. 231-245, 2014.

[113] D. Basler, W. Leis, B. Görlach, A. J. Meixner, and F. Schleifenbaum, "How Molecular Mechanics Can Measure Nanoscopic Flow," *The Journal of Physical Chemistry C,* vol. 116, no. 27, pp. 14694-14700, 2012.

[114] R. M. Kemmler, "Entwicklung eines optischen Sensors zur hochempfindlichen Messung fluider Systeme," Zulassungsarbeit, Mathematisch-Naturwissenschaftliche Fakultät, Eberhard Karls Universität Tübingen, 2012.

[115] T. D. Rammler, "Parametrisierung einer drucksensitiven Oberfläche mit FRET-Funktionalisierung," Abschlussbericht Modulpraktikum, Institut für Physikalische und Theoretische Chemie, Eberhard Karls Universität Tübingen, 2016.

[116] T. D. Rammler, "Charakterisierung einer drucksensitiven Oberfläche mit FRET-Funktionalisierung," Bachelorarbeit, Institut für Physikalische und Theoretische Chemie, Eberhard Karls Universität Tübingen, 2014.

[117] P. W. K. Rothemund, "Folding DNA to create nanoscale shapes and patterns," *Nature,* vol. 440, no. 7082, pp. 297-302, 2006.

[118] G. P. Acuna, F. M. Möller, P. Holzmeister, S. Beater, B. Lalkens, and P. Tinnefeld, "Fluorescence Enhancement at Docking Sites of DNA-Directed Self-Assembled Nanoantennas," *Science,* vol. 338, no. 6106, pp. 506-510, 2012.

[119] K. J. Breslauer, R. Frank, H. Blöcker, and L. A. Marky, "Predicting DNA duplex stability from the base sequence," *Proceedings of the National Academy of Sciences of the United States of America,* vol. 83, no. 11, pp. 3746-3750, 1986.

[120] V. Kim *et al.*, "Unusual effects in single molecule tautomerization: hemiporphycene," *Physical Chemistry Chemical Physics,* vol. 20, no. 41, pp. 26591-26596, 2018.

[121] A. J. Meixner *et al.*, "Coupling single quantum dots to plasmonic nanocones: optical properties," *Faraday Discussions,* vol. 184, pp. 321-337, 2015.

[122] S. Simmert, M. K. Abdosamadi, G. Hermsdorf, and E. Schäffer, "LED-based interference-reflection microscopy combined with optical tweezers for quantitative three-dimensional microtubule imaging," *Optics Express,* vol. 26, no. 11, pp. 14499-14513, 2018.

[123] F. Schleifenbaum, S. Peter, and A. J. Meixner, "Detecting the Same Individual Protein and Its Photoproducts via Fluorescence and Surface-Enhanced Raman Spectroscopic Imaging," *The Journal of Physical Chemistry A,* vol. 114, no. 1, pp. 143-150, 2010.

7 List of Abbreviations

AD	activating domain
AU	Airy unit
BiFC	bimolecular fluorescence complementation
bp	base pair
CFP	cyan fluorescent protein
CIB1	CRYPTOCHROME-INTERACTING BASIC-HELIXHOOP-HELIX PROTEIN1
CMOS	complementary metal-oxide-semiconductor
Co-IP	co-immunoprecipitation
COP1	CONSTITUTIVELY PHOTOMORPHOGENIC1
cry2	cryptochrome 2
DBD	DNA-binding domain
dsDNA	double stranded DNA
dSTORM	direct stochastic optical reconstruction microscopy
EGFP	enhanced green fluorescence protein
EMCCD	electron-multiplying charged-coupled device
FCS	fluorescence correlation spectroscopy
FD	frequency domain
FIDSAM	fluorescence intensity decay shape analysis microscopy
FLIM	fluorescence lifetime imaging microscopy
FLT	fluorescence lifetime
FP	fluorescent protein

(F)PALM	(fluorescence) photoactivated localization microscopy
FRET	Förster resonance energy transfer
FWHM	full width at half maximum
GFP	green fluorescent protein
GSD	ground-state depletion
GSDIM	ground-state depletion followed by individual molecule return
GSH	glutathione
GST	glutathione S-transferase
GUI	graphical user interface
IC	internal conversion
ILG	intron-less gene
IPG	intron-poor gene
IRF	instrument response function
ISC	intersystem crossing
MLE	maximum likelihood estimation
mRNA	messenger RNA
MSD	mean square displacement
NA	numerical aperture
NB	nuclear body
NLLS	nonlinear least squares
NLS	nuclear localization sequence
(F)PALM	(fluorescence) photoactivated localization microscopy
phyA	phytochrome A

phyB	phytochrome B
PMMA	polymethyl methacrylate
pol II	RNA Polymerase II
PSF	point spread function
PVA	polyvinyl alcohol
QD	quantum dot
RESOLFT	reversible saturable optically linear fluorescence transitions
RFP	red fluorescent protein
SE	SERRATE
siRNA	small interfering RNA
smFRET	single-molecule Förster resonance transfer
SMLM	single-molecule localization microscopy
SOFI	superresolution optical fluctuation imaging
SPA	SUPPRESSOR OF *phyA-105*
SPDIM	spectral position determination microscopy
sptPALM	single particle tracking with photoactivated localization microscopy
ssDNA	single-stranded DNA
STED	stimulated emission depletion
STORM	stochastic optical reconstruction microscopy
TCSPC	time correlated single photon counting
TD	time domain
TF	transcription factor
Ti	tumor inducing

TIRFM	total internal reflection microscopy
VAEM	variable-angle epifluorescence microscopy
VR	vibrational relaxation
YFP	yellow fluorescent protein

8 Appendix

Table 4 lists the most relevant components used to assemble the custom-built spectromicroscopy platform, providing necessary information to assemble such a system or parts of it. The item entries are ordered according to the different module sections in chapter 4.2. General components like computer equipment or miscellaneous optomechanical components are listed at the end and summarized where appropriate. In addition, approximate equipment costs (without warranty) are provided to assess individual components and also estimate the total cost of the platform presented in this work. General specifications of the instruments can be obtained from the corresponding vendors to search for alternatives or updated versions.

Table 4 | List of components used in the assembly of the spectromicroscopy platform in this work.

Identifier[a]	Item	Vendor	Part number	Price[b]
	Support			
	Nexus Optical Table, 1.2 m x 2.5 m x 310 mm, M6 x 1.0 Mounting Holes	Thorlabs	T1220C	3.6
	Active Legs, 700 mm (27.5") High, Set of Four	Thorlabs	PTS603	2.8
	Laser Unit			
	Oxxius Laserboxx Diode laser 642 nm, 130 mW (CW)	Laser 2000	OXX-642-130	2.5
	Vortran Stradus DPSS Laser 561 nm, 50 mW (CW)	Laser 2000	VOR-561-050	6.5
	Oxxius Laserboxx Diode laser 488 nm, 100 mW (CW)	Laser 2000	OXX-488-100	6.1
	Laser module NANO 250-405-80 405 nm, 80 mW (CW)	Qioptiq	G040-946-000	4.0
	Supercontinuum fiber laser	NKT Photonics	SuperK Extreme EXB-4	41.6
	Multi-line tunable filter	NKT Photonics	SuperK SELECT UV/VIS-nIR	8.8
	Polychromatic Modulator (AOTF) 450 - 700 nm	AA OPTO-ELECTRONIC	AOTFnC-VIS-TN	2.4
	4-channel RF driver	AA OPTO-ELECTRONIC	AA.MPDS4C	1.5
	Ø1" Manual Rotation Stage, Metric	Thorlabs	RP005/M	0.1
BS3	Laser Beamsplitter H 405 LPXR	AHF analysentechnik AG	F48-403	0.4
BS2	Laser Beamsplitter zt 488 RDC	AHF analysentechnik AG	F43-088	0.3
BS1	Beamsplitter HC BS 555	AHF analysentechnik AG	F38-555	0.3
	Laser Clean-Up Filter ZET 405/20	AHF analysentechnik AG	F49-405	0.4
	Laser Clean-up Filter ZET 488/10	AHF analysentechnik AG	F49-488	0.3
	560/14 BrightLine HC	AHF analysentechnik AG	F39-561	0.4
	Laser Clean-up Filter ZET 640/10	AHF analysentechnik AG	F49-643	0.3
	Coupling Unit			
	XY Translating Lens Mount for Ø1" Optics (x2)	Thorlabs	CXY1	0.3
	Z-Axis Translation Mount (x2)	Thorlabs	SM1Z	0.4
L1	350 - 700 nm, f = 11.0 mm, NA = 0.25 Aspheric Lens	Thorlabs	C220TMD-A	0.1
L2	Ø1" Achromatic Doublet, ARC: 400-700 nm, f=30 mm	Thorlabs	AC254-030-A-ML	0.1
	Polarization-Maintaining FC/PC Fiber Optic Patch Cable PM-S405-XP	Thorlabs	P1-405BPM-FC-2	0.2
	Mounted GT Polarizer, 10 mm x 10 mm, 350 - 700 nm AR Coating	Thorlabs	GTH10M-A	0.6
	Ø1/2" Mounted Achromatic Half-Wave Plate, Ø1" Mount, 400 - 800 nm	Thorlabs	AHWP05M-600	0.8

Identifier[a]	Item	Vendor	Part number	Price[b]
	Sample Stage			
	Objective alpha Plan-Fluar 100x/1,49 Oil M27	ZEISS	421190-9800-000	9.0
	Picomotor Controller/Driver Kit, Four-Axis	Newport	8742-4-KIT	1.0
	Picomotor Actuator, 1 in. Travel, 30 nm Resolution, 9.5 mm Shank	Newport	8302	0.5
	Linear stage TS10 M	Qioptiq	G080211000	0.6
	3-Axis Piezo Scanner with Direct Position Measuring	Physik Instrumente (PI)	P-527.3CD	10.0
	3-Axis Digital Piezo Nanopositioning Controller	Physik Instrumente (PI)	E-710.3CD	8.6
BS4	TIRF Quad zt405/488/561/640rpc	AHF analysentechnik AG	F73-410	0.6
L3	Ø1" UVFS Plano-Convex Lens, f = 150.0 mm, ARC: 350 - 700 nm	Thorlabs	LA4874-A-ML	0.1
	Linear stage TM 90-25	Qioptiq	G403372000	0.9
	Adjustable Mirror Insert 30	Qioptiq	G063730000	0.1
	Camera			
	Digital CMOS camera	Hamamatsu Photonics	ORCA-Flash4.0 V2	20.0
	525/50 BrightLine HC	AHF analysentechnik AG	F37-516	0.3
	600/52 BrightLine HC	AHF analysentechnik AG	F39-613	0.3
BS5	Laser Beamsplitter H 560 LPXR superflat	AHF analysentechnik AG	F48-559	0.3
BS6	Shortpass beamsplitter HC BS 556 SP	AHF analysentechnik AG	F38-556	0.3
	Adjustable Mirror Insert 30 (x2)	Qioptiq	G063730000	0.3
L4	Biconvex lens; N-BK 7; D=25.4; F=100; mounted	Qioptiq	G063854000	0.2
	Linear stage TM 90-25	Qioptiq	G403372000	0.5
	Spectrometer			
	Imaging Spectrograph	Princeton Instruments	Acton SP-2356	8.0
	Digital CCD Camera System	Princeton Instruments	PIXIS 100B	20.0
	Ruled Grating 1200 G/mm, 500 nm blaze wavelength	Princeton Instruments	ARC-1-120-500	2.0
	Ruled Grating 300 G/mm, 500 nm blaze wavelength	Princeton Instruments	ARC-1-090-500	2.0
	Complete Periscope Assembly, Metric	Thorlabs	RS99/M	0.3
	RazorEdge LP Edge Filter 488 RU	AHF analysentechnik AG	F76-488	0.7
L5	Achr. VIS ARB2; D=12.5; F=40; mounted	Qioptiq	G052010000	0.1
	Centering Mounting Plate 25	Qioptiq	G061025000	0.1
	Single Photon Detectors			
	Single Photon Avalanche Diodes (SPAD), < 100 cps dark counts (x2)	Micro Photon Devices	PDM	10.0
	TCSPC Module	Picoquant	PicoHarp 300	14.0
	SymPhoTime 64 software	Picoquant	SPT64-1+2	10.0

Identifier[a]	**Item**	**Vendor**	**Part number**	**Price**[b]
L6	Ø1" Achromatic Doublet, ARC: 400-700 nm, f=40.0 mm	Thorlabs	AC254-040-A	0.1
L7	Achr. VIS ARB2; D=25.4; F=200; mounted	Qioptiq	G063237000	0.1
L8	Achr. VIS ARB2; D=25.4; F=400	Qioptiq	G322340322	0.1
	Centering Mounting Plate 25 (x2)	Qioptiq	G061025000	0.1
	Micrometer G 10	Qioptiq	G061162000	0.1
	Ø1" Mounted Precision Pinhole, 50 ± 3 µm	Thorlabs	P50D	0.1
BS7	Laser Beamsplitter H 560 LPXR superflat	AHF analysentechnik AG	F48-559	0.3
	525/50 BrightLine HC	AHF analysentechnik AG	F37-516	0.3
	600/52 BrightLine HC	AHF analysentechnik AG	F39-613	0.3
BS8	20 mm Polarizing Beamsplitter Cube, 420 - 680 nm	Thorlabs	PBS201	0.2
	PC for hardware control, data acquisition and analysis 32 GB DDR3 RAM ZOTAC GeForce RTX 2070 graphic card SSD hard drive (RAID 0), 256 GB (x4) Monitor (x2)	misc. vendors	-	1.3
	Additional Software			
	LabVIEW	National Instruments	LabVIEW 2018	1.0
	MATLAB	MathWorks	R2018b	2.0
	Optics and Optomechanical Components			
	Protected Silver Mirror Ø1" (x20)	Thorlabs	PF10-03-P01	0.8
	Mirror Mounts (x20)	Radiant Dyes	MDI-HS-3030-M6	1.8
	Magnet Plates (x5)	Radiant Dyes	RD-MP	0.3
	Miscellaneous (Holder, Rods, Clamps, etc.)	Thorlabs, Qioptiq	-	2.0
			total	216.4

[a] As referenced in chapter 4.2. [b] All figures in thousands of euros (k€) before tax.